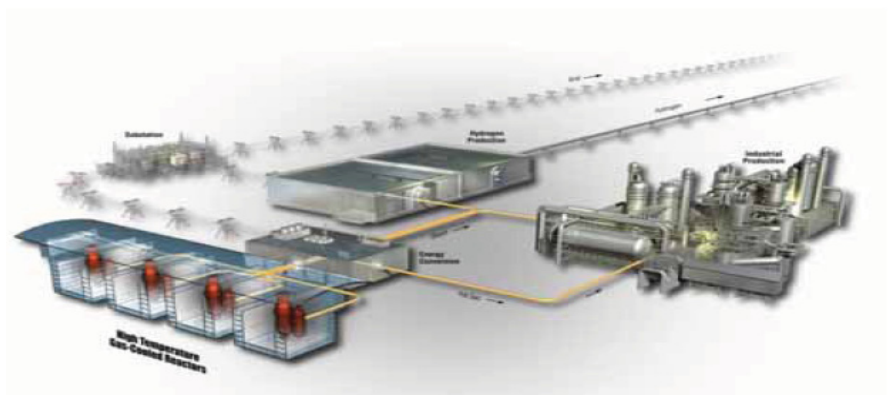


Scaling Studies for High Temperature Test Facility and Modular High Temperature Gas-Cooled Reactor

Richard R. Schultz
Paul D. Bayless
Brian D. Hawkes
Richard W. Johnson
James R. Wolf
Brian Woods

February 2012



The INL is a U.S. Department of Energy National Laboratory operated by Battelle Energy Alliance



DISCLAIMER

This information was prepared as an account of work sponsored by an agency of the U.S. Government. Neither the U.S. Government nor any agency thereof, nor any of their employees, makes any warranty, expressed or implied, or assumes any legal liability or responsibility for the accuracy, completeness, or usefulness, of any information, apparatus, product, or process disclosed, or represents that its use would not infringe privately owned rights. References herein to any specific commercial product, process, or service by trade name, trade mark, manufacturer, or otherwise, does not necessarily constitute or imply its endorsement, recommendation, or favoring by the U.S. Government or any agency thereof. The views and opinions of authors expressed herein do not necessarily state or reflect those of the U.S. Government or any agency thereof.

Scaling Studies for High Temperature Test Facility and Modular High Temperature Gas-cooled Reactor

**Richard R. Schultz, Paul D. Bayless, Brian D. Hawkes, Richard W. Johnson, and
James R. Wolf (INL); Brian Woods (Oregon State University)**

February 2012

**Idaho National Laboratory
Next Generation Nuclear Plant Project
Idaho Falls, Idaho 83415**

<http://www.inl.gov>

**Prepared for the
U.S. Department of Energy
Office of Nuclear Energy
Under DOE Idaho Operations Office
Contract DE-AC07-05ID14517**

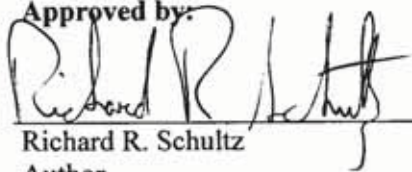
Next Generation Nuclear Plant Project

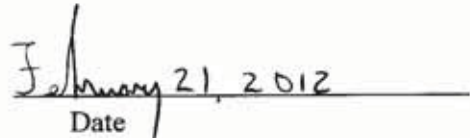
Scaling Studies for High Temperature Test Facility
and Modular High Temperature Gas-cooled Reactor

INL/EXT-12-24701

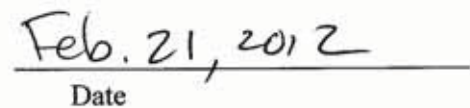
February 2012

Approved by:

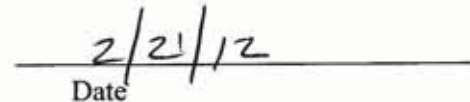

Richard R. Schultz
Author


Date


Hans D. Gougar
VHTR TDO Technical Deputy Director


Date


Diane V Croson
VHTD TDO Deputy Director


Date

EXECUTIVE SUMMARY

The Oregon State University (OSU) High Temperature Test Facility (HTTF) is an integral experimental facility that will be constructed on the OSU campus in Corvallis, Oregon. The HTTF project was initiated, by the U.S. Nuclear Regulatory Commission (NRC), on September 5, 2008 as Task 4 of the 5-year High Temperature Gas Reactor Cooperative Agreement via NRC Contract 04-08-138. Until August, 2010, when a DOE contract was initiated to fund additional capabilities for the HTTF project, all of the funding support for the HTTF was provided by the NRC via their cooperative agreement.

The U.S. Department of Energy (DOE) began their involvement with the HTTF project in late 2009 via the Next Generation Nuclear Plant (NGNP) project. Because the NRC's interests in HTTF experiments were only centered on the depressurized conduction cooldown (DCC) scenario, NGNP involvement focused on expanding the experimental envelope of the HTTF to include steady-state operations and also the pressurized conduction cooldown (PCC) scenario.

Since DOE has included the HTTF as an ingredient in the NGNP thermal-fluids validation program, several important outcomes should be noted: (a) The reference prismatic reactor design that serves as the basis for scaling the HTTF, became the modular high temperature gas-cooled reactor (MHTGR) (b) To enable the HTTF to operate at more representative steady-state conditions, i.e. with turbulent flow conditions in the core, DOE contributed the resources necessary to allow operation at a steady-state power of 2.2 MW. Consequently the HTTF may operate at steady-state conditions that are more representative of the MHTGR than it could with its initial design components.

As this report is being written, the design concept is being finalized but many of the details are still in various stages of review, revision, and approval. In an effort to gain a clear understanding of the correspondence between the projected thermal-fluid behavior of the HTTF in relation to the modular high temperature gas-cooled reactor (MHTGR), a number of analyses have been performed using both systems analysis software (RELAP5-3D) and computational fluid dynamics software. These calculations enable all of the various scaling relationships to be considered concurrently. At a later date, as the HTTF is built, shakedown tests performed, and adjustments to the hardware are completed, a more finalized set of comparisons between the HTTF and the MHTGR will be performed to: (a) examine the correspondence between the two and (b) identify and quantify the HTTF atypicalities.

Steady-state simulations of the MHTGR and the HTTF have been performed. The calculations addressed the thermal-hydraulic behavior of both, as well as the thermal stress response of the HTTF.

Reference calculations of the MHTGR were performed using the RELAP5-3D computer code. The input model represented the reactor vessel, reactor cavity, and reactor cavity cooling system (RCCS). The core and reflectors were modeled as a series of concentric rings with a coolant gap in between. The reflector rings containing control rod holes were further divided into two rings, one solid and one containing the holes. Unit cells based on a coolant channel were used to model the fuel blocks. Radiation and two-dimensional conduction were modeled to transfer heat from the core through the reflectors to the core barrel, reactor vessel, and RCCS. The RCCS was modeled as an air-cooled system with flow driven by natural convection.

The initial HTTF scoping calculations were performed with a scaled-down version of the MHTGR input model. These calculations identified a problem with the facility. With the facility at full power, with prototypical helium inlet and outlet temperatures, the flow through the core was laminar. This resulted in reduced heat transfer from the core to the coolant, which in turn caused the initial temperatures in the core and reflectors to be too high. The power was subsequently upgraded from 650 kW to 2.2 MW to induce turbulent flow and achieve cooling rates consistent with the (scaled down) MHTGR

Sensitivity calculations using both RELAP5-3D and STAR-CCM+ were performed to help investigate the next HTTF core design. The RELAP5-3D calculations looked at how different combinations of reflector coolant holes affected the core bypass. The STAR-CCM+ calculations estimated the local temperatures in the core for several of the reflector coolant hole geometry options. These simulations predicted significant local temperature peaking that would be inconsistent with that expected for the MHTGR, and that the proposed arrangements of cooling holes resulted in the reflectors being hotter than the core ceramic.

These results precipitated another core redesign, resulting in the current model. RELAP5-3D sensitivity calculations were again performed to address the bypass flow provided by different cooling hole sizes and locations. Results from the analysis of the redesigned model agreed with those from the MHTGR steady-state calculations with respect to overall conditions and with the helium temperatures at the entrance to the reactor vessel outlet plenum. Although the Reynolds numbers in the core are an order of magnitude lower than those in the reference plant, the Reynolds numbers are nevertheless representative of turbulent flow and the flow behavior anticipated in the HTTF can be linked to the behavior in the MHTGR using the scaling laws. The lower turbulent flow rates in the HTTF do result in reduced convective heat transfer; together with differences in thermal conductivity, this yields much higher structure temperatures in the core and reflectors than in the MHTGR. But again, the linkage between the HTTF and the MHTGR via the scaling laws enable defensible comparisons between the two to be performed. It is anticipated that data from the system characterization tests will be used to improve the RELAP5-3D input model, particularly the modeling of the conduction heat transfer in the reflectors. Following completion of this task, a more rigorous comparison based on real data will be performed.

Also at steady-state conditions, thermal stress analyses were performed to investigate the likelihood of catastrophic cracking in the ceramic core. These calculations indicate that some cracking will occur in the HTTF ceramic core. Although the calculational model is unable to predict the size or length of the cracks, visual observations based on heating ceramic samples in ovens at high temperatures have shown that the cracks will likely be surface cracks that do not penetrate the full thickness of the ceramic structures and furthermore will be narrow with rough walls and won't open free-flowing passages for the HTTF working fluid. The first plastic strain observed in the model occurred when the temperature was ramped up to about half of the final temperature, indicating that the temperatures would have to be reduced by about half to prevent the onset of any cracking. In anticipation that the cracking will materialize itself in the form of surface cracks, as noted above, it is unrealistic to try to operate the system to not have some cracks. Therefore, the test matrix will be tuned to chronologically perform the experiments in the order of lowest anticipated temperatures first followed by the higher anticipated temperatures as the experimental program continues. Further analysis is needed to apply these calculational results to both design HTTF experimental operating guidelines and to more rigorously order the experimental test matrix.

Scoping RELAP5-3D calculations of DCC and PCC transients in the HTTF and the MHTGR were performed. Heatup and cooldown operational evolutions in the HTTF were also simulated.

The response of the two facilities during a DCC transient was similar. The order in which peak temperatures were reached in the various structures in the reactor vessel was the same in the HTTF and the MHTGR. Peak core temperatures were about the same, although the increase from steady-state conditions was larger in the MHTGR. The radial temperature gradient across the side reflector was about 100°C higher in the HTTF than in the MHTGR. Considering the facility time scale factor of 2, the HTTF temperatures are peaking earlier than those of the reference plant.

Two sets of sensitivity calculations were performed. Increasing the decay power by 20% resulted in higher peak temperatures that occurred later in both facilities. Modeling the boundary volume connected to the reactor vessel outlet as pure air instead of pure helium changed the core flow behavior. With

helium, all of the core and reflector flow channels were flowing upward. With air, there was a mixture, with some channels flowing up and some down. However, there was an insignificant effect on the temperature response because the heat transfer is dominated by radiation and conduction, not by convection. Graphite oxidation was not considered in the MHTGR simulation.

There was little difference between the DCC and PCC transients in the HTTF, whereas noticeable differences occurred between these transients in the MHTGR. The principal reason for this is the power/flow mismatch at the onset of the transient. The flow in the MHTGR is reduced at a slower rate than the power, allowing some of the stored energy in the core and reflectors to be removed before the overall heatup begins. This results in lower temperatures in the PCC transient, with the peak fuel temperature dropping by 100-150°C. In the HTTF, little of the stored energy is removed because the flow transitions to laminar flow early in the coastdown, reducing the convective heat transfer coefficient. The peak temperatures in the HTTF PCC transient were less than 20°C lower than those in the DCC transient. There were some minor differences in the flow patterns in the core between the MHTGR and HTTF, concerning which channels were flowing up and which down, but these had little effect on the overall facility response given the relative unimportance of convective heat transfer compared to radiation and conduction.

Two HTTF heatup transients were simulated, one from ambient temperature and one following termination of a DCC transient. The heatup from ambient indicated that there may be a concern with increased radial temperature gradients across the core blocks during the heatup. The recovery following a DCC experiment suggested that a more rapid return to operating conditions may be achieved if the system is first cooled for a while before reestablishing power to the heater rods.

Two cooldown transients following completion of a DCC experiment were also simulated, using different flow rates with the heaters turned off. The permanent side reflector is the structure that takes the longest to cool down, because it has no direct convective cooling by the flowing helium; it must transfer heat by radiation or conduction to either the core barrel or the side reflector. After 24 hours, all of the structure average temperatures were within 15°C of ambient with ~50% of nominal cooling flow, and within 45°C of ambient with ~20% cooling flow.

The calculations performed to date indicate that the HTTF experiments will give a reasonable representation of the behavior of the MHTGR for the scenarios under consideration. Although sometimes the flow behavior in the cooling channels may differ by an order of magnitude, e.g., during steady-state conditions, from that of the MHTGR, because the cooling channel flow is either turbulent in both the HTTF and the MHTGR or laminar in both concurrently, enables the use of the scaling laws to obtain reasonable comparisons between the HTTF and MHTGR.

CONTENTS

EXECUTIVE SUMMARY	v
ACRONYMS	xv
1. INTRODUCTION	1
2. REFERENCE REACTOR DESIGN	3
3. HTTF EXPERIMENTAL MATRIX: DISCUSSION OF PLANNING ACTIVITIES	6
3.1 Background	6
3.2 Testing Overview	6
3.3 RELAP5-3D Scoping Calculations	7
3.4 Depressurized Conduction Cooldown Tests	7
3.4.1 HTTF EXPERIMENT-001: Double Ended Inlet-Outlet Crossover Duct Break	7
3.4.2 HTTF EXPERIMENT-002: Control Rod Drive Nozzle Break	7
3.4.3 HTTF EXPERIMENT-003: Instrumentation Port Break	7
3.4.4 HTTF EXPERIMENT-004: Inlet Crossover Duct Break	7
3.4.5 HTTF EXPERIMENT-005: Pressure Relief Valve Break	13
3.4.6 HTTF EXPERIMENT-006: Double Ended Inlet-Outlet Crossover Duct Break	13
3.4.7 HTTF EXPERIMENT-007: Pressure Relief Valve Break	13
3.4.8 HTTF EXPERIMENT-008: Double Ended Inlet-Outlet Crossover Duct Break, Gas Similarity	13
3.5 Depressurized Conduction Cooldown Tests with Degraded RCCS	13
3.5.1 HTTF EXPERIMENT-009: Double Ended Inlet-Outlet Crossover Duct Break with failure of single train of RCCS	13
3.5.2 HTTF EXPERIMENT-010: Double Ended Inlet-Outlet Crossover Duct Break with failure of two trains of RCCS	14
3.6 Pressurized Conduction Cooldown Tests	14
3.6.1 HTTF EXPERIMENT-011: Complete loss of flow	14
3.6.2 HTTF EXPERIMENT-012: Complete loss of flow with failure of single train of RCCS	14
3.6.3 HTTF EXPERIMENT-013: Outlet Duct Break	14
3.6.4 HTTF EXPERIMENT-014: Complete loss of flow, gas similarity	14
3.7 Inlet Plenum Mixing Tests	15
3.8 Normal Operations—Outlet Plenum Mixing Tests	15
4. HTTF TO MHTGR SCALING RATIOS	16
5. STUDIES OF STEADY-STATE BEHAVIOR IN MHTGR AND HTTF USING RELAP5-3D AND COMPUTATIONAL FLUID DYNAMICS	20
5.1 MHTGR Modeling and Analysis	20
5.1.1 RELAP5-3D Input Model Description	20
5.1.2 RELAP5-3D Calculations	23
5.2 HTTF Thermal-hydraulic Modeling and Analysis	24

5.2.1	Background	24
5.2.2	RELAP5-3D Input Model	27
5.2.3	Steady-State Calculations	29
5.2.4	Thermal Stress Analysis.....	31
5.2.5	Summary	42
6.	STUDIES OF TRANSIENT SCENARIOS IN MHTGR AND HTTF USING RELAP5-3D	44
6.1	Depressurized Conduction Cooldown.....	44
6.1.1	Base Case Calculations	44
6.1.2	Sensitivity Calculations.....	52
6.2	Pressurized Conduction Cooldown	59
6.2.1	Base Case Calculations	59
6.2.2	Sensitivity Calculations.....	67
6.3	HTTF Operational Transients	71
6.4	Summary	79
7.	SUMMARY OF DEVELOPMENTAL NEEDS FOR RELAP5-3D	81
7.1	Air Ingress.....	81
7.1.1	Split Pipe Model	81
7.1.2	Add a New Correlation to the RELAP5-3D Code.....	81
7.1.3	Link to a CFD Code.....	81
7.1.4	Summary of Developmental Needs to Model Density-Gradient-Driven Stratified Flow	82
7.2	Dust and Fission Product Tracking	82
7.3	Graphite Oxidation.....	82
8.	REFERENCES	83

FIGURES

Figure 2-1.	MHTGR module (DOE 1986).....	3
Figure 2-2.	Plan view of reactor vessel and internals in an elevation through the core region (DOE 1986).....	4
Figure 2-3.	Isometric view through MHTGR reactor building (DOE 1986).....	5
Figure 2-4.	RCCS cooling system and air cooling panels.	5
Figure 5-1.	RELAP5-3D nodalization of the MHTGR reactor vessel.....	21
Figure 5-2.	Cross section of the MHTGR reactor vessel in the core region.	21
Figure 5-3.	Cross-section of the RELAP5-3D model of the MHTGR reactor vessel.....	22
Figure 5-4.	RELAP5-3D modeling of the MHTGR control rod reflector rings.	22
Figure 5-5.	Unit cell for the core rings in the RELAP5-3D MHTGR model.	22
Figure 5-6.	Nodalization of the RCCS and reactor cavity in the RELAP5-3D MHTGR model.	23
Figure 5-7.	Calculated HTTF temperatures in the bottom portion of the core for the 2.2 MW base case.	26

Figure 5-8. Calculated HTTF temperatures in the bottom portion of the core for the 2.2 MW control rod hole sensitivity case.	26
Figure 5-9. RELAP5-3D nodalization of the HTTF reactor vessel.	27
Figure 5-10. Cross-section of the RELAP-3D model of the HTTF reactor vessel.	28
Figure 5-11. Unit cells used in the RELAP5-3D model of the HTTF reactor vessel.	29
Figure 5-12. Thermal conductivity (W/m K) of Greencast 94F as a function of temperature (K).	32
Figure 5-13. Illustration of the CFD model for the 1/12 sector.	33
Figure 5-14. Cross sectional view of the CFD model.	33
Figure 5-15. Temperature (K) distribution along the vertical edge of the permanent side reflector (m) (temperature increasing with core depth as measured from the top).	33
Figure 5-16. Temperature contours in the plane of the ninth lowest disk.	35
Figure 5-17. Close-up view of temperature contours in the ceramic core and the mesh for the CFD result.	35
Figure 5-18. Comparison of temperature computed using CFD code to that remapped onto the stress analysis mesh.	36
Figure 5-19. ABAQUS/Standard finite element mesh of a section of ninth disk.	36
Figure 5-20. STAR-CCM+ model temperatures (K) mapped onto the ABAQUS/Standard model.	37
Figure 5-21. Close-up view of the mapped temperatures (K) in the ABAQUS/Standard model.	38
Figure 5-22. Measured coefficient of thermal expansion for Greencast 94F.	39
Figure 5-23. Calculated von Mises stress (Pa) in the Greencast 94F ceramic.	40
Figure 5-24. Calculated plastic strain from thermal expansion.	40
Figure 5-25. Elements exhibiting some degree of plastic strain.	41
Figure 5-26. Calculated deformation (m) in the disk.	41
Figure 6-1. Calculated peak fuel temperatures for the MHTGR DCC transient.	45
Figure 6-2. Calculated peak heater rod temperatures for the HTTF DCC transient.	45
Figure 6-3. Calculated fuel axial average temperatures for the MHTGR DCC transient.	46
Figure 6-4. Calculated core region axial average temperatures for the HTTF DCC transient.	46
Figure 6-5. Calculated central reflector axial average temperatures for the MHTGR DCC transient.	47
Figure 6-6. Calculated central reflector axial average temperatures for the HTTF DCC transient.	47
Figure 6-7. Calculated side reflector axial average temperatures for the MHTGR DCC transient.	48
Figure 6-8. Calculated side reflector axial average temperatures for the HTTF DCC transient.	49
Figure 6-9. Calculated permanent side reflector, core barrel, and reactor vessel axial average temperatures for the MHTGR DCC transient.	49
Figure 6-10. Calculated permanent side reflector, core barrel, and reactor vessel axial average temperatures for the HTTF DCC transient.	50

Figure 6-11. Calculated reactor vessel heat removal and core power for the MHTGR DCC transient.	50
Figure 6-12. Calculated reactor vessel heat removal and core power for the HTTF DCC transient.	51
Figure 6-13. Calculated channel inlet coolant velocities for the MHTGR DCC transient.	51
Figure 6-14. Calculated channel inlet coolant velocities for the HTTF DCC transient.	52
Figure 6-15. Peak fuel temperatures for the MHTGR DCC base and 120% decay power cases.	53
Figure 6-16. Peak heater rod temperatures for the HTTF DCC base and 120% decay power cases.	53
Figure 6-17. Peak reactor vessel temperatures for the MHTGR DCC base and 120% decay power cases.	54
Figure 6-18. Peak reactor vessel temperatures for the HTTF DCC base and 120% decay power cases.	54
Figure 6-19. Calculated reactor vessel heat removal and core power for the MHTGR DCC 120% decay power case.	55
Figure 6-20. Calculated reactor vessel heat removal and core power for the HTTF DCC 120% decay power case.	55
Figure 6-21. Peak fuel temperatures for the MHTGR DCC base and reactor cavity air cases.	56
Figure 6-22. Peak heater rod temperatures for the HTTF DCC base and reactor cavity air cases.	57
Figure 6-23. Peak reactor vessel temperatures for the MHTGR DCC base and reactor cavity air cases.	57
Figure 6-24. Peak reactor vessel temperatures for the HTTF DCC base and reactor cavity air cases.	58
Figure 6-25. Coolant channel inlet velocities for the MHTGR DCC base and reactor cavity air cases.	58
Figure 6-26. Coolant channel inlet velocities for the HTTF DCC base and reactor cavity air cases.	59
Figure 6-27. Calculated peak fuel temperatures for the MHTGR PCC transient.	60
Figure 6-28. Calculated peak heater rod temperatures for the HTTF PCC transient.	60
Figure 6-29. Calculated fuel axial average temperatures for the MHTGR PCC transient.	61
Figure 6-30. Calculated core region axial average temperatures for the HTTF PCC transient.	61
Figure 6-31. Calculated central reflector axial average temperatures for the MHTGR PCC transient.	62
Figure 6-32. Calculated central reflector axial average temperatures for the HTTF PCC transient.	62
Figure 6-33. Calculated side reflector axial average temperatures for the MHTGR PCC transient.	63
Figure 6-34. Calculated side reflector axial average temperatures for the HTTF PCC transient.	63
Figure 6-35. Calculated permanent side reflector, core barrel, and reactor vessel axial average temperatures for the MHTGR PCC transient.	64
Figure 6-36. Calculated permanent side reflector, core barrel, and reactor vessel axial average temperatures for the HTTF PCC transient.	64

Figure 6-37. Calculated reactor vessel heat removal and core power for the MHTGR PCC transient.	65
Figure 6-38. Calculated reactor vessel heat removal and core power for the HTTF PCC transient.	65
Figure 6-39. Calculated channel inlet coolant velocities for the MHTGR PCC transient.	66
Figure 6-40. Calculated channel inlet coolant velocities for the HTTF PCC transient.	67
Figure 6-41. Peak fuel temperatures for the MHTGR PCC base and 120% decay power cases.	68
Figure 6-42. Peak heater rod temperatures for the HTTF PCC base and 120% decay power cases.	68
Figure 6-43. Peak reactor vessel temperatures for the MHTGR PCC base and 120% decay power cases.	69
Figure 6-44. Peak reactor vessel temperatures for the HTTF PCC base and 120% decay power cases.	69
Figure 6-45. Calculated reactor vessel heat removal and core power for the MHTGR PCC 120% decay power case.	70
Figure 6-46. Calculated reactor vessel heat removal and core power for the HTTF PCC 120% decay power case.	70
Figure 6-47. Calculated HTTF core structure average temperatures during an initial heatup transient.	71
Figure 6-48. Calculated HTTF reflector structure average temperatures during an initial heatup transient.	72
Figure 6-49. Calculated HTTF structure average temperatures during an initial heatup transient.	72
Figure 6-50. Calculated HTTF structure relative temperatures during an initial heatup transient.	73
Figure 6-51. Calculated HTTF structure relative temperatures during an initial heatup transient.	73
Figure 6-52. Calculated HTTF core average temperatures for the DCC reheat transient.	74
Figure 6-53. Calculated HTTF reflector average temperatures for the DCC reheat transient.	75
Figure 6-54. Calculated HTTF structure average temperatures for the DCC reheat transient.	75
Figure 6-55. Calculated HTTF core structure average temperatures for the DCC 50% flow cooldown transient.	76
Figure 6-56. Calculated HTTF reflector structure average temperatures for the DCC 50% flow cooldown transient.	76
Figure 6-57. Calculated HTTF structure average temperatures for the DCC 50% flow cooldown transient.	77
Figure 6-58. Calculated HTTF core average structure temperatures for the DCC 20% flow cooldown transient.	77
Figure 6-59. Calculated HTTF reflector structure average temperatures for the DCC 20% flow cooldown transient.	78
Figure 6-60. Calculated HTTF structure average temperatures for the DCC 20% flow cooldown transient.	78

TABLES

Table 1-1. Quality assurance information for the computer codes used for the computer simulations.....	2
Table 3-1. HTTF Test Matrix.	8
Table 4-1. Relationships between MHTGR and HTTF primary variables.	17
Table 4-2. Relationships between MHTGR and HTTF non-dimensional quantities.....	17
Table 4-3. Relationships between MHTGR and HTTF primary heat transfer variables.....	18
Table 4-4. Relationships between MHTGR and HTTF quantities specific to DCC and PCC scenarios.	19
Table 5-1. Desired and calculated MHTGR steady-state conditions.	24
Table 5-2. Calculated steady-state Reynolds numbers for the scaled MHTGR model.....	25
Table 5-3. Sample results from HTTF reflector hole size sensitivity calculations.	25
Table 5-4. Calculated steady-state conditions for the HTTF and MHTGR.	29
Table 5-5. Calculated HTTF and MHTGR steady-state Reynolds numbers.	30
Table 5-6. Calculated HTTF and MHTGR steady-state core channel outlet helium temperatures (°C).	30
Table 5-7. Calculated HTTF and MHTGR steady-state structure axial average temperatures (°C).....	31
Table 5-8. Mass flows and exit temperature: HTTF coolant channels for CFD and RELAP5 results.....	34
Table 5-9. Overall mass flows and temperatures for the CFD results compared to RELAP5 results.....	34
Table 5-10. Greencast 94F material properties.	38

ACRONYMS

CFD	computational fluid dynamics
DCC	depressurized conduction cooldown
D-LOFC	depressurized loss of forced convection
DOE	Department of Energy
HTTF	High Temperature Test Facility
INL	Idaho National Laboratory
MHTGR	Modular High Temperature Gas-Cooled Reactor
NGNP	Next Generation Nuclear Plant
NIST	National Institute of Standards and Technology
NRC	Nuclear Regulatory Commission
OSU	Oregon State University
PCC	pressurized conduction cooldown
PIRT	Phenomena Identification And Ranking Table
P-LOFC	pressurized loss of forced convection
RCCS	reactor cavity-cooling system
V&V	verification and validation
VHTR	very high temperature reactor

Scaling Studies for High Temperature Test Facility and Modular High Temperature Gas-cooled Reactor

1. INTRODUCTION

The High Temperature Test Facility (HTTF), to be located at Oregon State University in Corvallis, Oregon, has been undergoing design since 2008 when the project was initiated^a by the U.S. Nuclear Regulatory Commission (NRC). As this report is being written, that design concept is being finalized but many details are still in various stages of review, revision, and approval.

The HTTF will be 1/4-scale in both height and diametric dimensions to the Modular High Temperature Gas-cooled Reactor (MHTGR) described in the Preliminary Safety Information Document for the Standard MHTGR (DOE 1986). NRC's original intent for the HTTF was to study the depressurized conduction cooldown (DCC) scenario. The MHTGR is a prismatic block reactor design that uses graphite as a moderator in the form of prismatic graphite blocks in its core. It has an air-cooled reactor cavity-cooling system (RCCS) and its power conversion is provided by a Rankine cycle via a once-through steam generator.

The HTTF is one ingredient of a set of thermal-fluids experiments that will be used to generate validation data for the Next Generation Nuclear Plant (NGNP) experimental verification and validation (V&V) program (Schultz et al, 2008). As such, U.S. Department of Energy (DOE) funding has been used to define modifications that will expand the experimental envelope of the HTTF from the DCC scenario to include additional scenarios such as the pressurized conduction cooldown (PCC) scenario and also representative steady-state conditions.

The NGNP is presently scheduled to perform experiments within the scope formally defined by NRC Contract 04-08-138, with accommodations to perform experiments that are mutually beneficial to DOE. The experimental program will end in approximately March or April 2014, unless other provisions are made to expand the program scope.

The work described herein focuses on (a) the projected test matrix as defined in a preliminary fashion by the HTTF Program (Woods et al. unpublished), (b) the scaling parameters that relate the HTTF experiment design to the MHTGR, (c) calculations performed to project the behavior of the HTTF relative to the expected behavior of the MHTGR for selected scenarios representative of those listed in item a, and (d) a summary of conclusions derived from the calculations. Aside from the scaling relationships identified in item b, the most rigorous way to compare the scaled behavior of the HTTF relative to the MHTGR is via systems analysis code calculations summarized in item c, since systems analysis code calculations consider the global system behaviors.

Sections 2, 3, 4, and 5 summarize the work described in items a through d above.

The software used for the analyses summarized herein are listed in Table 1-1 together with the software's V&V status, operating system, version number, and the approach for ensuring their software algorithms are current.

a The HTTF design was initiated via the U.S. Nuclear Regulatory Commission (NRC) High Temperature Gas Reactor cooperative agreement that began on September 5, 2008 via NRC Contract 04-08-138. This NRC Contract is a 5-year agreement and the HTTF was originally designed to only address the depressurized conduction cooldown (DCC) scenario.

Table 1-1. Quality assurance information for the computer codes used for the computer simulations.

Computer Code	Version	Vendor	V&V Status	INL Computer	Computer Operating System
FlexPdE*	Student	PdE Solutions Inc., Spokane Valley, WA.	Unknown	Macintosh G5	OSX10.4.11
ABAQUS/ Standard	6.11-1	Dassault Systèmes Simulia Corp., Providence, RI, USA	Validated per ECAR-1698	Dell PowerEdge R410 cluster (Quark)	OpenSUSE 11.1
FLUENT	6.3.26	FLUENT Inc./Ansys Inc., 10 Cavendish Court, Centerra Resource Park, Lebanon, NH, 03766 USA	Vendor holds ISO 9001 certification	Dell PowerEdge 1950 distributed memory cluster (Helios)	OpenSUSE 11.1
GAMBIT	2.4.6	FLUENT Inc./Ansys Inc., 10 Cavendish Court, Centerra Resource Park, Lebanon, NH, 03766 USA	Vendor holds ISO 9001 certification	Dell PowerEdge 1950 distributed memory cluster (Helios)	OpenSUSE 11.1
MathCad	2001	Mathsoft, Inc, 101 Main St, Cambridge, MA 02142	Vendor holds ISO9001 certification	Macintosh G5	OSX10.4.11
RELAP5-3D	3.0.1is	Idaho National Laboratory	INL controlled	Macintosh MACPro	Ubuntu Linux 10.04 LTS
STARCCM+	6.02.007	CD-adapco, 60 Broadhollow Road, Melville, NY 11747	Vendor holds ISO 9001 certification	SGI Altix ICE 8200 distributed memory blade cluster (Ice Storm)	SUSE Linux Enterprise Server 10 Service Pack 2, with SGI Propack 6

* PdE Solutions, Inc., Spokane Valley, Wa, 2009.

2. REFERENCE REACTOR DESIGN

The HTTF design is based on the MHTGR prismatic reactor system as defined in the Preliminary Safety Identification Document (1986). The MHTGR is designed to use tristructural-isotropic fuel in a hexagonal prismatic cylindrical block, similar to the Fort St. Vrain design. The reactor is designed to deliver 350 MW(t) with a power density of 5.9 W/cc. The working fluid is helium on the primary side. The operating pressure is 6.4 MPa where the helium inlet temperature is 259°C and the helium exit temperature is 687°C for a total temperature rise of 428°C. Power conversion occurs via a secondary system that operates on the Rankine cycle using light water as the working fluid. The operating pressure is 17.3 MPa with an exit steam temperature of 541°C—over 180°C superheated.

The primary and secondary (steam generator) vessels, and their relationships to one another, are shown in Figure 2-1. The reactor vessel is designed such that helium, intended to enter the core, enters the reactor vessel via an annular passage in the cross duct. It then proceeds upward through annular-type passages, which are divided into distinct coolant inlet channels between the peripheral duct wall of the core region and the inner diameter of the reactor vessel wall. The helium then flows into the upper plenum where the control rod drives are housed. These flow passages can be seen in Figure 2-2 which presents a plan view of the reactor vessel taken in the core region at a plane that is perpendicular to both the axis of the reactor vessel and the direction of the flowing helium. As helium moves into the upper plenum it changes direction 180 degrees where it enters the annular core and inner and outer reflector regions. It then flows downward until it exits into the lower plenum where it gathers into a single stream that flows through the cross duct to the steam generator.

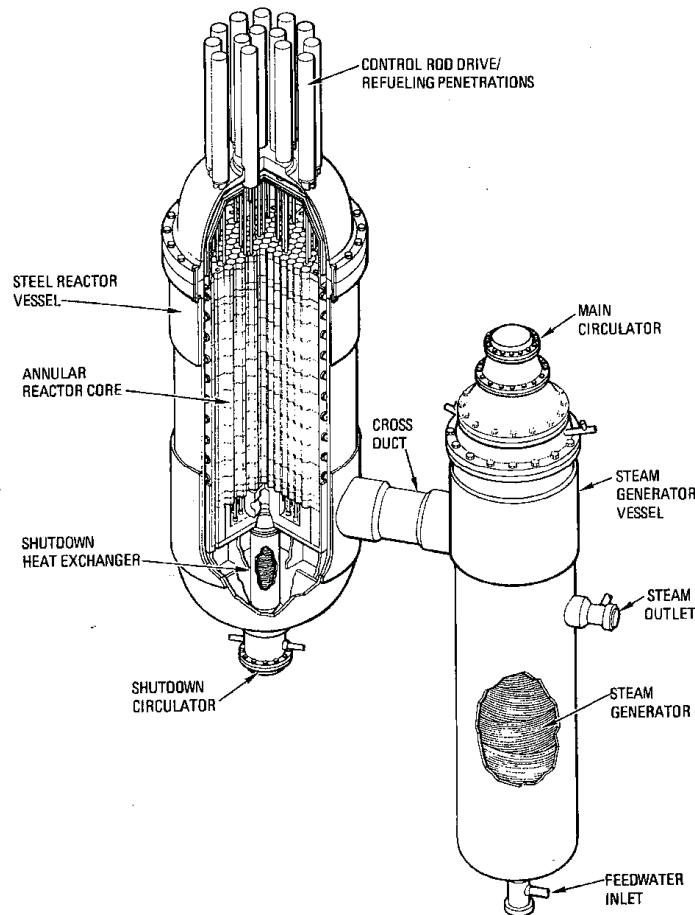


Figure 2-1. MHTGR module (DOE 1986).

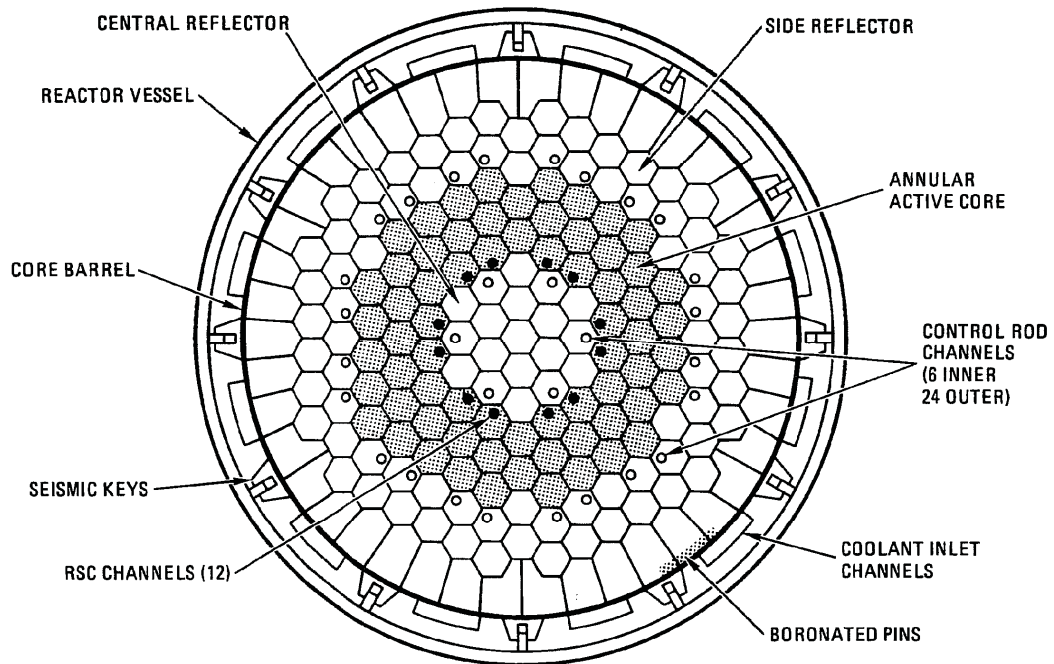


Figure 2-2. Plan view of reactor vessel and internals in an elevation through the core region (DOE 1986).

The steam generator consists of a large number of helical tubes containing water that is boiled and then superheated. The steam outlet nozzle is shown on the side of the steam generator vessel.

The reactor vessel and steam generator vessel are housed in a building as shown in Figure 2-3. The building is cooled by a continuous circulation of air inside the confinement and also by radiation heat transfer to the reactor cavity cooling heat exchanger—the air panels identified in Figure 2-4. Via the air panels, cooling is administered using environmental air that enters through passages shown in the RCCS inlet/exhaust structure shown in Figure 2-3.

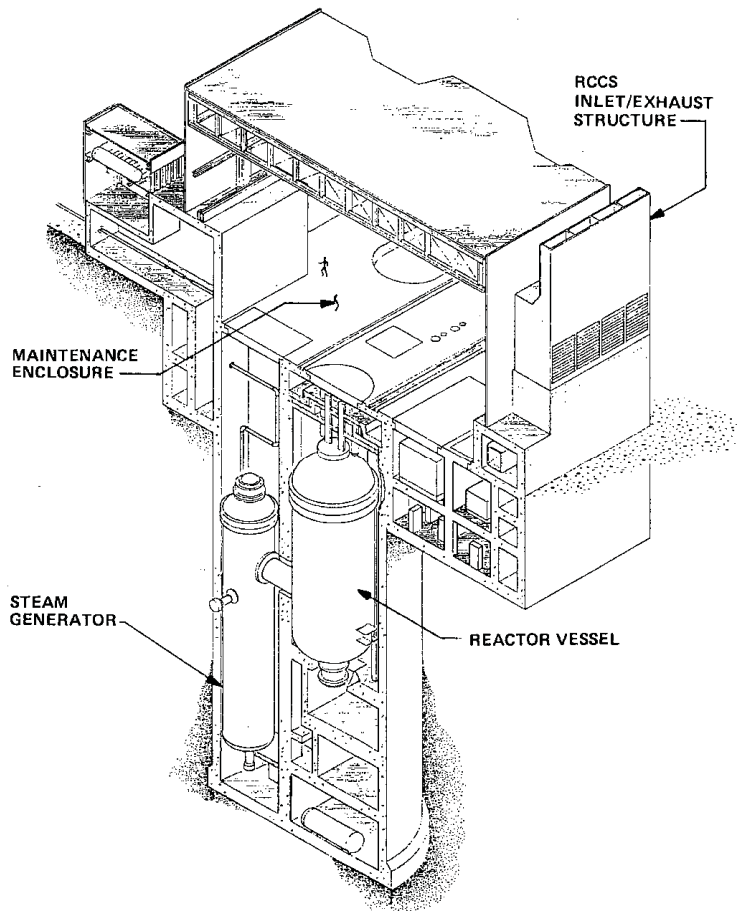


Figure 2-3. Isometric view through MHTGR reactor building (DOE 1986).

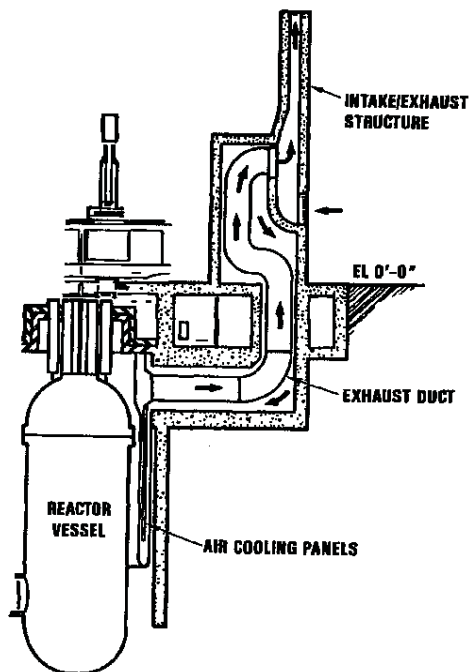


Figure 2-4. RCCS cooling system and air cooling panels.

3. HTTF EXPERIMENTAL MATRIX: DISCUSSION OF PLANNING ACTIVITIES

The preliminary test plan presented in this chapter was extracted from work in progress that exists in draft form as part of the HTTF Program at Oregon State University (OSU; Woods et al. unpublished) and revised to complement the report objectives and direction. The intent of including a summary of the preliminary test plan is to provide the basis for performing the calculations summarized in Chapter 5. The preliminary test plan was constructed (a) as part of Task 4.C of the Basic Research on High Temperature Gas Reactor Thermal Hydraulics and Reactor Physics Cooperative Agreement between NRC, OSU, University of Michigan, and Texas A&M University as described in NRC Contract 04-08-138 and (b) with input and accommodations to the needs of the NGNP methods R&D effort. As a preliminary plan it will identify the operation of interest and test initial, boundary conditions, and data requirements for the anticipated matrix testing under this agreement.

3.1 Background

The HTTF is an integral test facility designed to model the behavior of interest for a very high temperature gas reactor during a DCC event. It also has the potential to conduct limited explorations into the progression of the PCC event and phenomena during normal operations. The facility is scaled 1:4 by height and 1:64 by volume in relation to the Modular High Temperature Gas Reactor (MHTGR). The maximum core power for the facility is approximately 2.2 MW. The core region will be of a modular design to allow for both the prismatic block core and the pebble bed core designs to be tested, though only work using a prismatic core is contained within the current work scope. Details of the facility scaling are discussed in detail in reference [Woods et al 2011].

3.2 Testing Overview

The NGNP Phenomena Identification and Ranking Table (PIRT) was completed for the NRC in 2008.[Ball et al 2008] The HTTF testing program will provide data for the following three of the six general categories of postulated accident scenarios for the very high temperature gas reactor identified in the NGNP PIRT:

1. Pressurized loss of forced convection (P-LOFC)
2. Depressurized loss of forced convection (D-LOFC)
3. Depressurized loss of forced convection with air ingress.

Because the primary mode of heat removal from the core in the event of a loss of forced convection (LOFC) is through conduction and then radiation through the reactor cavity, the P-LOFC event is often referred to as the PCC event and the D-LOFC event as the DCC event. The D-LOFC involves some sort of reactor coolant system break that allows primary coolant to leak into the reactor cavity. The D-LOFC with air ingress is classified as a separate event because not all break scenarios result in significant air ingress. Factors that influence the amount of air ingress are the location and size of break.

Although a number of variations of the above three postulated scenarios will be investigated in the HTTF Program, two experiments, HTTF Experiments 11 and 1, are identified as *signature experiments* for the PCC and DCC scenarios because they serve as references for the remaining experiments in the PCC and DCC scenario investigations.

3.3 RELAP5-3D Scoping Calculations

RELAP5-3D scoping calculations were performed for HTTF Experiments 1 and 11. Section 5 describes the RELAP5-3D model, and Section 6 summarizes the transient calculations.

Presently, RELAP5-3D cannot properly model air ingress via density-gradient-driven stratified flow. However, RELAP5-3D is able to model the natural circulation anticipated in HTTF Experiment 1, where the air ingresses to the vessel lower plenum, moves upward through the core to the upper plenum, then moves down through the risers in the reverse direction.

3.4 Depressurized Conduction Cooldown Tests

The purpose of the DCC tests is to collect data for the air ingress and natural convection phases of the DCC event. All DCC tests will be initiated after the blowdown of the pressure vessel to equalize the pressures between the pressure vessel and the cavity simulation tank. The data will primarily be collected to support code validation efforts, but the data collected should be of sufficient quality and quantity to support the phenomenological analysis of each event.

3.4.1 HTTF EXPERIMENT-001: Double Ended Inlet-Outlet Crossover Duct Break

This test looks at the DCC event initiated by the break of the concentric inlet and outlet ducts, which allows for flow between both plena and the prototypical reactor cavity. It is anticipated that the event will go through three separate phases: (1) air ingress via density-gradient driven stratified flow, (2) air ingress via diffusion, and (3) natural circulation. Table 3-1 lists the initial and boundary conditions, test progression, and data requirements for this test.

3.4.2 HTTF EXPERIMENT-002: Control Rod Drive Nozzle Break

This test looks at the DCC event initiated by a break in one of the control rod nozzles located on the upper head of the MHTGR. Since air ingress by density-gradient driven stratified flow will likely end after the ingressing gas reaches the break location (in the upper plenum in this event), it is likely that there will be only two phases during this event: (1) air ingress via density-gradient driven stratified flow, and (2) natural circulation. Table 3-1 lists the initial and boundary conditions, test progression, and data requirements for this test.

3.4.3 HTTF EXPERIMENT-003: Instrumentation Port Break

This test looks at the DCC event initiated by a break in one of the instrumentation nozzles located on the lower head of the MHTGR. Because of the location and orientation of the instrumentation port, it is likely that there will be only two phases during this event: (1) air ingress via diffusion, and (2) natural circulation. Table 3-1 lists the initial and boundary conditions, test progression, and data requirements for this test.

3.4.4 HTTF EXPERIMENT-004: Inlet Crossover Duct Break

This test looks at the DCC event initiated by the break of the annular inlet duct that allows for flow between the upper plenum and the reactor cavity. Any ingressing gas will have to move up through the upcomer channels to reach the upper plenum. It is thus likely that this event will begin as a gas diffusion until the ingressing gas reaches the upper plenum after which the transient may contain an density-gradient driven stratified flow type component. Like test HTTF EXPERIMENT-001, it is anticipated that the event will go through three separate phases, however the order may be somewhat different: (1) air

ingress via diffusion, (2) air ingress via density-gradient driven stratified flow, and (3) natural circulation. Table 3-1 lists the initial and boundary conditions, test progression, and data requirements for this test.

Table 3-1. HTTF Test Matrix.

Test Number	Test	Initial Conditions	Transient ^b	Data Requirements
<i>Depressurized Conduction Cooldown</i>				
HTTF EXPERIMENT-001	Double Ended Inlet-Outlet Crossover Duct Break	Vessel Pressure: TBD Cavity Simulation Tank Pressure: 0.1 MPa Vessel Gas: Helium Cavity Simulation Tank Gas: Helium—Nitrogen (Mixed) Reference axial and radial temperature profiles.*	Stop forced convection. Open blowdown valve to depressurize vessel within 1 min. Once pressures equalized, open inlet and outlet duct break valves and close normal operations loop valves.	Gas content distribution in vessel and cavity simulation tank. Temperature distribution in core and reflector. Core flow rate. Vessel cavity air flow. Temperature distribution on vessel and RCCS walls. RCCS flow rate. Loop/core pressure drops. Duct density-gradient driven stratified flow rate. Duct flow distribution.
HTTF EXPERIMENT-002	Control Rod Drive Nozzle Break	Vessel Pressure: TBD Cavity Simulation Tank Pressure: 0.1 MPa Vessel Gas: Helium Cavity Simulation Tank Gas: Helium—Nitrogen (Mixed) Reference axial and radial temperature profiles.*	Stop forced convection. Open blowdown valve to depressurize vessel within 1 min. Once pressures equalized, open control rod drive break valve and close normal operations loop valves.	Gas content distribution in vessel and cavity. Temperature distribution in core and reflector. Core flow rate. Reactor cavity air flow. Temperature distribution on vessel and RCCS walls. RCCS flow rate. Loop/core pressure drops.
HTTF EXPERIMENT-003	Instrumentation Port Break	Vessel Pressure: TBD Cavity Simulation Tank Pressure: 0.1 MPa Vessel Gas: Helium Cavity Simulation Tank Gas: Helium—Nitrogen (Mixed) Reference axial and radial temperature profiles.*	Stop forced convection. Open blowdown valve to depressurize vessel within 1 min. Once pressures equalized, open instrumentation port break valve and close normal operations loop valves.	Break flow rate. Break temperature profile.

^b The core power levels employed are scaled to the phase of the scenario. Thus for the air ingress phase, which occurs immediately after the system has depressurized, the core power is 656 kW while core power used during a typical portion of the natural circulation phase is 82 kW.

Test Number	Test	Initial Conditions	Transient ^b	Data Requirements
HTTF EXPERIMENT-004	Inlet Crossover Duct Break	Vessel Pressure: TBD Cavity Simulation Tank Pressure: 0.1 MPa Vessel Gas: Helium Cavity Simulation Tank Gas: Helium— Nitrogen (Mixed) Reference axial and radial temperature profiles.*	Stop forced convection. Open blowdown valve to depressurize vessel within 1 min. Once pressures equalized, open inlet duct break valve and close normal operations loop valves.	
HTTF EXPERIMENT-005	Pressure Relief Valve Break	Vessel Pressure: TBD Cavity Simulation Tank Pressure: 0.1 MPa Vessel Gas: Helium Cavity Simulation Tank Gas: Helium— Nitrogen (Mixed) Reference axial and radial temperature profiles.*	Stop forced convection. Open blowdown valve to depressurize vessel within 1 min. Once pressures equalized, open pressure relief break valve and close normal operations loop valves.	
HTTF EXPERIMENT-006	Double Ended Inlet-Outlet Crossover Duct Break Check	Vessel Pressure: TBD Cavity Simulation Tank Pressure: 0.1 MPa Vessel Gas: Helium Cavity Simulation Tank Gas: Helium— Nitrogen (Mixed) Reference axial and radial temperature profiles.*	Stop forced convection. Open blowdown valve to depressurize vessel within 1 min. Once pressures equalized, open inlet and outlet duct break valves and close normal operations loop valves.	Gas content distribution in vessel and cavity simulation tank. Temperature distribution in core and reflector. Core flow rate. Vessel cavity air flow. Temperature distribution on vessel and RCCS walls. RCCS flow rate. Loop/core pressure drops. Duct density-gradient driven stratified flow rate. Duct flow distribution.
HTTF EXPERIMENT-007	Pressure Relief Valve Break Check	Vessel Pressure: TBD Cavity Simulation Tank Pressure: 0.1 MPa Vessel Gas: Helium Cavity Simulation Tank Gas: Helium— Nitrogen (Mixed) Reference axial and radial temperature profiles.*	Stop forced convection. Open blowdown valve to depressurize vessel within 1 min. Once pressures equalized, open pressure relief break valve and close normal operations loop valves.	Gas content distribution in vessel and cavity. Temperature distribution in core and reflector. Core flow rate. Reactor cavity air flow. Temperature distribution on vessel and RCCS walls. RCCS flow rate. Loop/core pressure drops. Break flow rate. Break temperature profile.

Test Number	Test	Initial Conditions	Transient ^b	Data Requirements
HTTF EXPERIMENT-008	Double Ended Inlet-Outlet Crossover Duct Break	Vessel Pressure: TBD Cavity Simulation Tank Pressure: 0.1 MPa Vessel Gas: TBD. Cavity Simulation Tank Gas: TBD. Reference axial and radial temperature profiles.*	Stop forced convection. Open blowdown valve to depressurize vessel within 1 min. Once pressures equalized, open pressure relief break valve and close normal operations loop valves.	Gas content distribution in vessel and cavity simulation tank. Temperature distribution in core and reflector. Core flow rate. Vessel cavity air flow. Temperature distribution on vessel and RCCS walls. RCCS flow rate. Loop/core pressure drops. Duct density-gradient driven stratified flow rate. Duct flow distribution.
<i>Depressurized Conduction Cooldown with Failed or Degraded RCCS Channels</i>				
HTTF EXPERIMENT-009	Double Ended Inlet-Outlet Duct Break	Vessel Pressure: TBD Cavity Simulation Tank Pressure: 0.1 MPa Vessel Gas: Helium Cavity Simulation Tank Gas: Helium— Nitrogen (Mixed) Reference axial and radial temperature profiles.*	Stop forced convection. Open blowdown valve to depressurize vessel within 1 min. Once pressures equalized, open control rod drive break valve and close normal operations loop valves. Close water inlet valve to one train of RCCS cooling.	Gas content distribution in vessel and cavity simulation tank. Temperature distribution in core and reflector. Core flow rate. Vessel cavity air flow. Temperature distribution on vessel and RCCS walls. RCCS flow rate. Loop/core pressure drops.
HTTF EXPERIMENT-010	Double Ended Inlet-Outlet Duct Break	Vessel Pressure: TBD Cavity Simulation Tank Pressure: 0.1 MPa Vessel Gas: Helium Cavity Simulation Tank Gas: Helium— Nitrogen (Mixed) Reference axial and radial temperature profiles.*	Stop forced convection. Open blowdown valve to depressurize vessel within 1 min. Once pressures equalized, open control rod drive break valve and close normal operations loop valves. Close water inlet valve to two trains of RCCS cooling.	Duct density-gradient driven stratified flow rate. Duct flow distribution.

Test Number	Test	Initial Conditions	Transient ^b	Data Requirements
<i>Pressurized Conduction Cooldown</i>				
HTTF EXPERIMENT-011	Complete loss of flow	Vessel Pressure: 0.8 MPa Vessel Gas: Helium Core exit average gas temperature: 687°C Reference axial and radial temperature profiles.*	Natural circulation.	Temperature distribution in core and reflector. Gas temperature distribution in inlet plenum. Core flow rate. Core coolant flow distributions. Bypass flow. Reactor cavity air flow.
HTTF EXPERIMENT-012	Complete loss of flow with failed or degraded RCCS channels.	Vessel Pressure: 0.8 MPa Vessel Gas: Helium Core exit average gas temperature: 687°C Reference axial and radial temperature profiles.*	Natural circulation.	Temperature distribution in upper head, vessel and RCCS walls. RCCS flow rate. Loop/core pressure drops.
HTTF EXPERIMENT-013	Outlet Duct Break	Vessel Pressure: 0.8 MPa Vessel Gas: Helium Core exit average gas temperature: 687°C Reference axial and radial temperature profiles.*	Open outlet duct break valve. Reactor Protection System response: TBD. Natural circulation.	Temperature distribution in core and reflector. Gas temperature distribution in inlet plenum. Core flow rate. Core coolant flow distributions. Bypass flow. Reactor cavity air flow. Temperature distribution in upper head, vessel and RCCS walls. RCCS flow rate. Loop/core pressure drops. Break flow rate. Pressure drop across break.
HTTF EXPERIMENT-014	Complete loss of flow	Vessel Pressure: 0.8 MPa Vessel Gas: TBD Core exit average gas temperature: 687°C Reference axial and radial temperature profiles.*	Natural circulation.	Temperature distribution in core and reflector. Gas temperature distribution in inlet plenum. Core flow rate. Core coolant flow distributions. Bypass flow. Reactor cavity air flow. Temperature distribution in upper head, vessel and RCCS walls. RCCS flow rate. Loop/core pressure drops.
<i>Inlet Plenum Mixing</i>				
HTTF EXPERIMENT-015	Inlet plenum mixing.	Vessel Pressure: TBD Vessel Gas: TBD	NA	Gas temperature distribution in inlet plenum.
HTTF EXPERIMENT-016	Inlet plenum mixing.	Core exit average gas		Core coolant flow distributions.

Test Number	Test	Initial Conditions	Transient ^b	Data Requirements
HTTF EXPERIMENT-017	Inlet plenum mixing.	temperature: TBD Natural circulation or reverse forced convection.		Temperature distribution in upper head, vessel and RCCS walls.
<i>Normal Operations—Outlet Plenum Mixing</i>				
HTTF EXPERIMENT-018	Outlet Plenum Mixing.	Vessel Pressure: TBD Vessel Gas: TBD	NA	Gas temperature distribution in outlet plenum. Core coolant flow distributions. Temperature distribution in upper head, vessel and RCCS walls.
HTTF EXPERIMENT-019	Outlet Plenum Mixing.	Core exit average gas temperature: TBD Forced convection.		
HTTF EXPERIMENT-020	Outlet Plenum Mixing.			

*Reference profiles will be developed during the shakedown phase.

3.4.5 HTTF EXPERIMENT-005: Pressure Relief Valve Break

This test looks at the DCC event initiated by an inadvertent opening of the primary loop pressure relief valve and the subsequent sticking open of that valve. This break is different than the other initiated breaks because of its distance from the vessel, since the pressure relief valve is on the steam generator. This distance, however, might allow for the cleanest boundary conditions of all the break scenarios, thus, from a code validation standpoint, the collection of this test data will be quite valuable. Table 3-1 lists the initial and boundary conditions, test progression, and data requirements for this test.

3.4.6 HTTF EXPERIMENT-006: Double Ended Inlet-Outlet Crossover Duct Break

This test is a repeat of HTTF EXPERIMENT-001. The purpose of such a test is to demonstrate the repeatability of the phenomena in the HTTF. Table 3-1 lists the initial and boundary conditions, test progression, and data requirements for this test.

3.4.7 HTTF EXPERIMENT-007: Pressure Relief Valve Break

This test is a repeat of HTTF EXPERIMENT-005. The purpose of this test is to demonstrate the repeatability of the operational procedures at the HTTF, since this is potentially the cleanest core boundary condition, allowing for the most effective comparison between tests. Table 3-1 lists the initial and boundary conditions, test progression, and data requirements for this test.

3.4.8 HTTF EXPERIMENT-008: Double Ended Inlet-Outlet Crossover Duct Break, Gas Similarity

With the exception of the gases in the pressure vessel and the cavity simulation tank, this test is a repeat of HTTF EXPERIMENT-001. Because of the geometric scaling of the HTTF, there is significant scaling distortion in the air ingress by density-gradient driven stratified flow phase in the HTTF when using prototypical gases [Woods et al 2009]. There is also uncertainty in the gas mixture that will exist in the reactor cavity affecting the air ingress phase of the accident. The purpose of this test is to run a test for which there is less scaling distortion during the air ingress by density-gradient driven stratified flow phase. It is anticipated that the distortion reduction can be accomplished by using a different gas set in the vessel and cavity simulation tank, however, the actual gas selection has yet to be completed. See Table 3-1 for the initial and boundary conditions, test progression and data requirements for this test.

3.5 Depressurized Conduction Cooldown Tests with Degraded RCCS

The DCC tests with degraded RCCS were designed to consider the effect of likely failures in the RCCS as surmised from the NRC PIRT exercise.

3.5.1 HTTF EXPERIMENT-009: Double Ended Inlet-Outlet Crossover Duct Break with failure of single train of RCCS

This test is a repeat of HTTF EXPERIMENT-001 but with the loss of one train of RCCS cooling. The HTTF RCCS is comprised of eight forced water cooling sections, where each section is considered a single train. Each section is fed by its own inlet and outlet valve and piping systems. In this test, one of the eight RCCS sections will be disabled. The purpose of the test is to look at the asymmetry in core and reflector temperatures that develop as the result of the asymmetrical cooling situation. Table 3-1 lists the initial and boundary conditions, test progression and data requirements for this test.

3.5.2 HTTF EXPERIMENT-010: Double Ended Inlet-Outlet Crossover Duct Break with failure of two trains of RCCS

This test is a repeat of HTTF EXPERIMENT-009 but with the loss of two trains of RCCS cooling. It is yet to be determined whether or not the two sections that are disabled are consecutive or separated by an operable RCCS section. Again, the purpose of this test is to look at the asymmetry in core and reflector temperatures that develop as the result of the asymmetrical cooling situation. Table 3-1 lists the initial and boundary conditions, test progression, and data requirements for this test.

3.6 Pressurized Conduction Cooldown Tests

PCC tests are needed to collect data that measure the conduction and radiation heat transfer within the core that dominates the facility cooling during the PCC event. Again, the data collected will primarily be used to support code validation efforts, but the data collected should be of sufficient quality and quantity to support the phenomenological analysis of each event.

3.6.1 HTTF EXPERIMENT-011: Complete loss of flow

This test looks at the PCC event initiated by a complete loss of gas flow. The HTTF core will be brought to an initial core and reflector temperature condition typical of normal operations. The test will be initiated by turning off the gas circulator to stop forced convection through the HTTF core. It is anticipated that as the gas inertia decreases, the flow through some core channels will begin to reverse and move into a situation of intracore recirculation. Table 3-1 lists the initial and boundary conditions, test progression, and data requirements for this test.

3.6.2 HTTF EXPERIMENT-012: Complete loss of flow with failure of single train of RCCS

This test is a repeat of HTTF EXPERIMENT-011 with the loss of one train of RCCS cooling. The HTTF RCCS is comprised of eight forced water cooling sections, where each section is considered a single train. Each section is fed by its own inlet and outlet valve and piping systems. In this test one of the eight RCCS sections will be disabled. The purpose of the test is to look at the asymmetry in core and reflector temperature that develop as the result of the asymmetrical cooling situation during a PCC event. Table 3-1 lists the initial and boundary conditions, test progression, and data requirements for this test.

3.6.3 HTTF EXPERIMENT-013: Outlet Duct Break

This test looks at the PCC event initiated by a break in the outlet duct. In the prototype, a leak path would develop between the inlet and outlet concentric ducts. For the HTTF in this scenario, a valve between the inlet and outlet ducts in the HTTF will be opened which will allow for a recirculation path to develop for the gas flow. The primary system gas can either go through the steam generator or move straight from the outlet plenum to the upcomers without being cooled in the steam generator. Following the outlet duct break the progression of this test will progress as per the anticipated MHTGR Reactor Protection System actions which have yet to be determined for the HTTF. Table 3-1 lists the initial and boundary conditions, test progression, and data requirements for this test.

3.6.4 HTTF EXPERIMENT-014: Complete loss of flow, gas similarity

With the exception of the gases in the pressure vessel, this test is a repeat of HTTF EXPERIMENT-011. Because of the pressure scaling, there is significant scaling distortion in the natural circulation phase of the PCC for inlet plenum mixing and potentially for the intracore circulation when using prototypical gases [Ball et al 2008]. The purpose of this test is to run a test for which there is less

scaling distortion during the natural circulation phase of the PCC for these phenomena. It is anticipated that the distortion reduction can be accomplished by using a different gas in the vessel, but the actual gas selection has yet to be completed. Table 3-1 lists the initial and boundary conditions, test progression, and data requirements for this test.

3.7 Inlet Plenum Mixing Tests

HTTF EXPERIMENT-015, -016, and -017 are the inlet plenum mixing tests. These tests will focus on the inlet plenum, and thus be more similar to separate effects tests than the previous 14 tests discussed. During the PCC event as the system moves into an intracore natural circulation phase, it is anticipated that hot gas plumes will exit the top of the core. These tests will examine the strength of these plumes and the mixing that will occur in the upper plenum prior to the impingement of these plumes on the upper head. Because of the reduced pressure at the HTTF it is anticipated that there will be significant distortions when modeling this event. However, there are a number of ways available at the facility to change the scaling parameters, Reynolds Number (Re), and Froude Number (Fr) in order to make the tests more prototypical—(1) change vessel gas, (2) reverse forced flow or natural circulation, and/or (3) change the temperature of the gas jets. Although, these tests may not be able to be completed with complete similarity, tests for a number of configurations will be completed in order to understand the effects of these distortions and scaling parameters on the inlet plenum mixing and heat transfer.

3.8 Normal Operations—Outlet Plenum Mixing Tests

HTTF EXPERIMENT-018, -019, and -020 are the outlet plenum mixing tests. These tests will focus on the outlet plenum. During normal operations, gas jets exit the core into the outlet plenum where they interact with the structures in the outlet plenum as they make their way to the outlet duct. There is a potential that some of the jets exiting the core will be at a significantly higher temperature than the core exit average temperature. If these hot jets do not mix significantly prior to entering the outlet duct, there is a possibility that some damage can occur to the structures downstream of the outlet plenum. The mixing of these jets will be explored in these tests. Because of the reduced pressure at the HTTF, it is anticipated that there will be significant distortions when modeling this event. Again, there are a number of ways available to change the scaling parameters, Re, in order to make the tests more prototypical—(1) change vessel gas, (2) change flow rate, and/or (3) change the temperature of the gas jets. Although, these tests may not be able to be completed with complete similarity, tests for a number of configurations will be completed in order to understand the effects of these distortions and scaling parameters on the outlet plenum mixing and heat transfer.

4. HTTF TO MHTGR SCALING RATIOS

The HTTF facility is a 1/4 geometric length scale, 1/2 time scale, representation of the MHTGR design. The facility will operate at full-scale temperature using helium as the working fluid at reduced pressure. The scaling analysis presented by Woods et al. (2009) indicates that HTTF will simulate the following phenomena:

- Core conduction and radiation heat transfer
- Vessel radiation heat transfer
- Core temperature profiles
- Air-ingress by density-gradient driven stratified flow
- Air-ingress by molecular diffusion
- Single-phase air natural circulation.

The HTTF is also capable of limited primary side blow-downs and PCC studies at an operating pressure of 8 bars.

In general, MHTGR behavior of a quantity as a function of time may be predicted by multiplying the same measured quantity in HTTF by a scaling factor and expanding the time scale by a factor of two. For this reason the scaling factors are included in this section—and some of them were employed to compare the behavior of the HTTF and the MHTGR for selected parameters, e.g., time. If the quantity is dimensionless and scaling is preserved in HTTF (e.g., Power/initial Power, Pressure/initial Pressure, etc.), then it is equivalent to the HTTF data in the MHTGR as a function of scaled time. If a dimensional quantity (e.g., convection heat transfer coefficient) or nondimensional parameter (e.g., Reynolds number or Nusselt number) is distorted from prototypical, an assessment of the distortion is required to predict MHTGR conditions from HTTF data. A preliminary list of plots of predicted MHTGR behavior that may be generated from HTTF data and the associated scaling relationships is given in Table 4-1 to Table 4-4.

Although some scaling parameters and scaling distortions may be estimated from the basic scaling relationships of the HTTF facility (such as scaled Reynolds number as a function of scaled velocity and scaled diameter), some more complicated distortions (such as heat transfer relationships that are a function of several variables), will require analysis of HTTF data to accurately quantify it. Also, some scaling parameters (such as those that relate to core heat transfer) await the final design choice before they may be quantified. Presently the most comprehensive way to compare the thermal-fluid behavior in the HTTF with that of the MHTGR is via the use of models of both systems in systems analysis codes such as RELAP5-3D. This approach considers the give and take of each of the current contributing phenomena and will ultimately allow assessment of atypicalities inherent to the HTTF with respect to the MHTGR.

Steps required to predict MHTGR behavior from HTTF data include:

1. Collection of HTTF data.
2. Assessment of HTTF data validity and data uncertainties.
3. Assessment of scaling distortions in HTTF data; the scaling distortion assessment will be a function of the choice of materials and the fundamental material properties of these materials relative to the MHTGR materials.
4. Scaling HTTF data to MHTGR using basic scaling relationships and incorporating scaling distortions from Item 3.
5. Assessment of uncertainties of scaled MHTGR behavior.

Table 4-1. Relationships between MHTGR and HTTF primary variables.^{cd}

Time Scale	
Time = t	$t_{MHTGR} = 2 t_{HTTF}$
Dimensional Quantities	
Temperature = T	$T_{MHTGR} = T_{HTTF}$
Differential temperature increase across core = ΔT	$\Delta T_{MHTGR} = \Delta T_{HTTF}$
Pressure = P	$P_{MHTGR} = P_{HTTF}$
Differential pressure across core = ΔP	$\Delta P_{MHTGR} = \Delta P_{HTTF}$
Density = ρ	$\rho_{MHTGR} = \rho_{HTTF}$
Velocity = V	$V_{MHTGR} = V_{HTTF} * 2$
Mass flow rate = \dot{M}	$\dot{M}_{MHTGR} = \dot{M}_{HTTF} * (A_{MHTGR} / A_{HTTF}) * 2$
Heat flux to atmosphere = q	$q_{MHTGR} = q_{HTTF} / 2.11$ (subject to final design)
Core heat flux = q_{core}	$q_{c-MHTGR} = q_{c-HTTF} * (A_R L_R^{1/2}) = 1 / 30.9$
Convection heat transfer coefficient = h	$h_{MHTGR} = h_{HTTF} * f(Re)^e$

Table 4-2. Relationships between MHTGR and HTTF non-dimensional quantities.^f

Non-dimensional Quantities and Scaling Ratios	
$P/P_{initial}$	$P/P_{initial-MHTGR} = P/P_{initial-HTTF}$
$T/T_{initial}$	$T/T_{initial-MHTGR} = T/T_{initial-HTTF}$
Power/Power _{initial}	Power/Power _{initial-MHTGR} = Power/Power_{initial-HTTF}}}
Core $\Delta P/P$	Core $\Delta P/P_{MHTGR} = Core \Delta P/P_{HTTF}$
Radial temperature profile	$(T - T_{outside-radius}) / (T_{center} - T_{outside-radius})$ v. $Radius/outside-Radius$ determined by final design
Axial temperature profile	$(T - T_0) / (T_{max} - T_0)$ v. z/L determined by final design
Thermal striping	$\frac{(T_{max} - T_{min})_{Hot-duct}}{(T_{hot} - T_{cold})_{core\ exit\ channels}}$ unknown functions of mixing and therefore of Reynolds number
$\frac{(T_{max} - T_{min})_{Hot\ duct}}{\bar{T}_{Hot\ duct}}$	Same as thermal striping
Re	$Re_{MHTGR} = Re_{HTTF} * (V_{MHTGR} / V_{HTTF}) * (D_{MHTGR} / D_{HTTF})$

c. Subscripts indicate whether variable pertains to HTTF or MHTGR.

d. All HTTF data may be shown as a function of either t_{HTTF} or $t^* = 2t_{HTTF} = t_{MHTGR}$. In some cases HTTF data and ratios may be shown as a function of other variables for analysis or characterization purposes.

e. Re = Reynolds number.

f. All HTTF data may be shown as a function of either t_{HTTF} or $t^* = 2t_{HTTF} = t_{MHTGR}$. In some cases HTTF data and ratios may be shown as a function of other variables for analysis or characterization purposes, e.g., radial temperature profile.

Table 4-3. Relationships between MHTGR and HTTF primary heat transfer variables^g

Core Conduction Heat Transfer	
Biot modulus ^h = Bi	$Bi = Bi_{HTTF} (h_{MHTGR} / h_{HTTF}) (D_{MHTGR} / D_{HTTF}) / (K_{MHTGR} / K_{HTTF})$
Core Fourier modulus ⁱ = Fo	$Fo_{MHTGR} = Fo_{HTTF} (\alpha_{MHTGR} / \alpha_{HTTF}) * 32$
Convection Heat Transfer	
Nusselt number ^j = Nu	$Nu_{MHTGR} = Nu_{HTTF} * (h_{MHTGR} / h_{HTTF}) * (D_{MHTGR} / D_{HTTF})$
Heat Flux Ratios	
$q_{convection} / q_{total}$	$q_{convection}$ is a function of Re and Gr ^k
$q_{radiation} / q_{total}$	q_{total} is a function of Re, Gr, and emissivity

g. All HTTF data may be shown as a function of either t_{HTTF} or $t^* = 2t_{HTTF} = t_{MHTGR}$. In some cases HTTF data and ratios may be shown as a function of other variables for analysis or characterization purposes.

h. K = thermal conductivity of core material.

i. $\alpha = K_{core} / (C_p \rho)$.

j. D = characteristic diameter.

k. Gr = Grashof number.

Table 4-4. Relationships between MHTGR and HTTF quantities specific to DCC and PCC scenarios.¹

DCC Specific Quantities	
Mass ratio ^m	$M(t)_{\text{system}}/M(t_{\text{initial}})_{\text{system}}$
Pressure ratio	$P/P_{\text{initial}} \text{ v. } M/M_{\text{initial}}$
Mass ratio with respect to M_{MHTGR}	$M_{\text{MHTGR}} = M_{\text{HTTF}} (Volume_{\text{MHTGR}} / Volume_{\text{HTTF}})$
$\dot{m}_{\text{break}} = dm/dt$	$\dot{m}_{\text{MHTGR}} = \dot{m}_{\text{HTTF}} (Volume_{\text{MHTGR}} / Volume_{\text{HTTF}})$ where, $\dot{m}_{\text{MHTGR}} = dm_{\text{MHTGR}} / dt^*$
$P(t)$	with individual curves for each break size
$M_{\text{air}}/M_{\text{total}}$	$(M_{\text{air}}/M_{\text{total}})_{\text{MHTGR}} = (M_{\text{air}}/M_{\text{total}})_{\text{HTTF}}$
Height of air ingress level = H	$H_{\text{MHTGR}} = H_{\text{HTTF}} * 4$
Froude number for air ingress = Fr	$Fr_{\text{MHTGR}} = Fr_{\text{HTTF}}$
Densimetric Froude number ⁿ = Fr_D	$(Fr_D)_{\text{MHTGR}} = (Fr_D)_{\text{HTTF}}$
Air mole fraction = mf	at various non-dimensional elevations (H/H_{max}) for either stratified flow or diffusion
Mole fraction on basis of MHTGR	$mf_{\text{MHTGR}} = mf_{\text{HTTF}} at (L_R)^2 = mf_{\text{HTTF}} at 16t$
PCC Specific Quantities	
Loop natural convection velocity = V	$V_{\text{MHTGR}} = V_{\text{HTTF}} * 2$
In-core natural convection	Dependant on final choice of channel diameter. See Section 6 on in-core natural convection.
Bypass flow	Dependant on final core design.

1. All HTTF data may be shown as a function of either t_{HTTF} or $t^* = 2t_{\text{HTTF}} = t_{\text{MHTGR}}$. In some cases HTTF data and ratios may be shown as a function of other variables for analysis or characterization purposes.

m. $M(t)$ = mass of system as a function of time.

n. Densimetric Froude number = $g' = (g \Delta \rho) / \rho_{\text{air}}$ where g = gravitational acceleration and $\Delta \rho = \rho_{\text{air}} - \rho_{\text{helium}}$.

5. STUDIES OF STEADY-STATE BEHAVIOR IN MHTGR AND HTTF USING RELAP5-3D AND COMPUTATIONAL FLUID DYNAMICS

Thermal-hydraulic analyses of the HTTF were performed to support the facility design effort. Of particular interest was how facility scaling might result in behavior different from the reference nuclear reactor (distortions). To address this concern, scoping models for both the reference MHTGR and HTTF were developed using the RELAP5-3D computer code [RELAP5 Code Development Team 2005]. Computational fluid dynamics (CFD) simulations of the HTTF were also performed using the STAR-CCM+ computer code. Stress analyses were performed using the ABAQUS computer code to investigate the effects of the steady-state thermal gradients on the core ceramic blocks.

5.1 MHTGR Modeling and Analysis

A scoping RELAP5-3D model of a portion of the MHTGR was developed to provide an indication of how the core would respond to conduction cooldown transients. Steady-state and transient simulations were performed that included uncertainties in certain geometric design parameters.

5.1.1 RELAP5-3D Input Model Description

The RELAP5-3D input model for the MHTGR was developed as a scoping model to provide reference simulations to compare with HTTF simulations. The model included the reactor vessel, reactor cavity atmosphere, and RCCS. Boundary conditions were applied where the cross vessel connects to the reactor vessel flow inlet and outlet. Information used to develop the model was obtained from the MHTGR Preliminary Safety Information Document [DOE/HTGR-86-024 1986].

Figure 5-1 shows the reactor vessel nodalization for the model. Cold helium enters the reactor vessel, flows into a region below the outlet plenum, then passes into the coolant riser channels on the outside of the core barrel. This flow enters the upper plenum before passing through a number of parallel channels in the core and reflectors. Flow exiting these paths is collected in the outlet plenum before flowing back out of the reactor vessel into the hot duct. The helium between the core barrel and reactor vessel, outside of the riser channels, was also included in the model.

A cross section of the MHTGR reactor vessel in the core region is shown in Figure 5-2, and the corresponding RELAP5-3D modeling approach is presented in Figure 5-3. Each reflector ring was modeled as a separate heat structure, with a gap in between rings through which helium flows. Two input models were developed, one that allowed radial flow between adjacent gap flow channels and one that did not. The reflector rings closest to the core were further divided into halves. The half farther away from the fuel is solid, and the other half contains the control rod holes; Figure 5-4 illustrates the modeling. Radiative and convective heat transfer was modeled between the reflector rings.

Three core rings were modeled using representative unit cells, which are shown in Figure 5-5. A coolant hole is in the center, surrounded by concentric rings of graphite, helium, fuel, and more graphite. Heat is transferred from the core to the adjacent reflector rings via conduction. The coolant gaps in the core are only connected to the middle core ring; this was done in expectation that modeling a convective path between the core and reflector would result in an uncharacteristically large radial heat transfer, because the actual block surface area in contact with the coolant gaps is much smaller than the modeled surface area in the core rings.

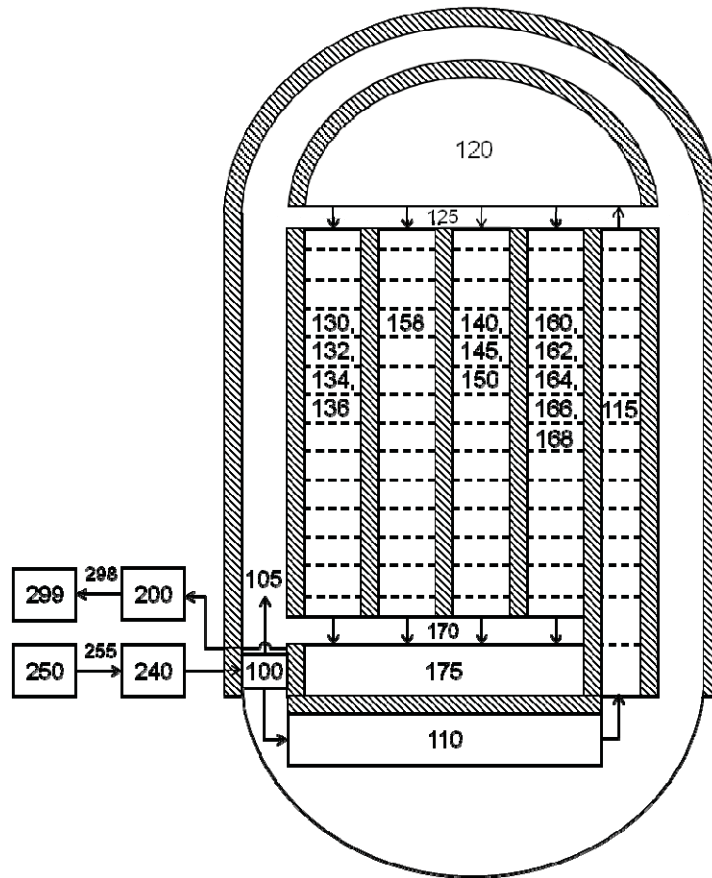


Figure 5-1. RELAP5-3D nodalization of the MHTGR reactor vessel.

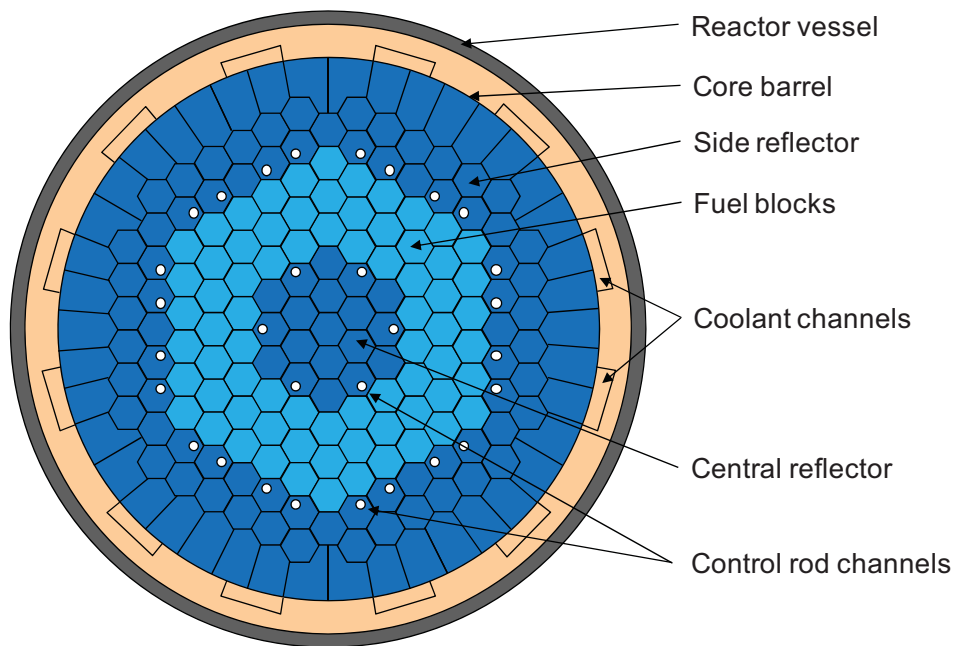


Figure 5-2. Cross section of the MHTGR reactor vessel in the core region.

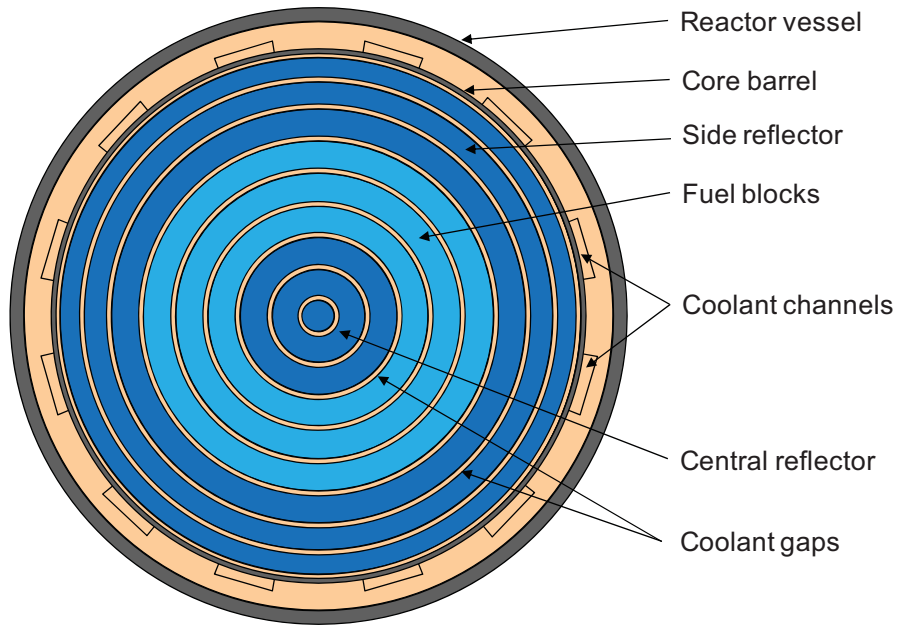


Figure 5-3. Cross-section of the RELAP5-3D model of the MHTGR reactor vessel.

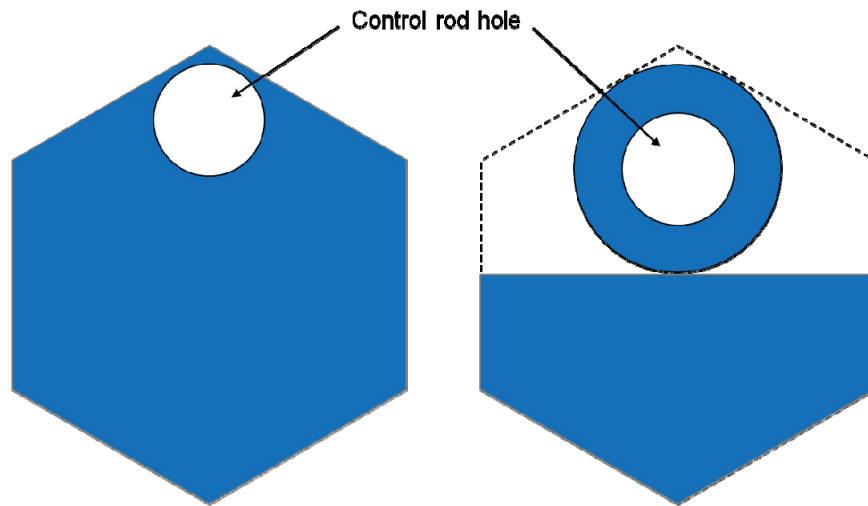


Figure 5-4. RELAP5-3D modeling of the MHTGR control rod reflector rings.

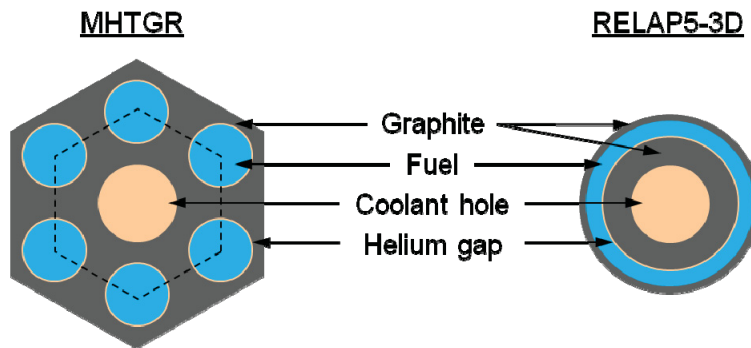


Figure 5-5. Unit cell for the core rings in the RELAP5-3D MHTGR model.

Radiation and convection were modeled from the side reflector to the core barrel, from the barrel to the riser channels and reactor vessel, and from the reactor vessel to the air-cooled RCCS. Radiation was also modeled from the top reflector to the upper plenum shield, from the shield to the upper head, and from the bottom reflector to the outlet plenum bottom plate. Axial conduction was modeled in all of the vertical structures except the building wall; the code's 2-D conduction model was used.

Figure 5-6 presents the nodalization of the RCCS and reactor cavity. Air enters the RCCS intake structure, flows through the downcomer to the lower plenum, then flows up through the risers before exiting back to the atmosphere. The back side of the downcomer is attached to a 1.5-m thick concrete wall. On the outside of the wall, 6 m of soil is modeled, with the outer edge being held at a constant temperature of 300 K. The reactor cavity (Component 900) is modeled as a 1-D stack of volumes maintained at a constant pressure. The axial nodalization in the cavity and RCCS matches that in the core and reactor vessel.

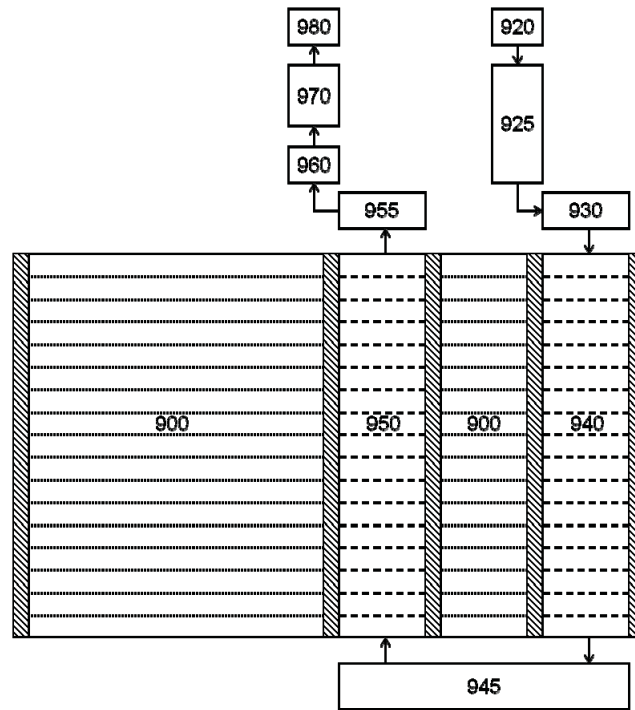


Figure 5-6. Nodalization of the RCCS and reactor cavity in the RELAP5-3D MHTGR model.

The total reactor power was set to 350 MW. A constant radial power density was assumed in the fuel blocks, with a chopped cosine axial power shape with a peak-to-average ratio of 1.2. During steady-state, 98.7% of the power is deposited in the fuel, with the remainder being generated in the reflector blocks, representing gamma and neutron heating of the reflectors; after scram, the power split is 95% in the fuel and 5% in the reflectors.

5.1.2 RELAP5-3D Calculations

Steady-state calculations were performed for both models (with and without radial cross flow). The model was adjusted as necessary to obtain a total bypass flow of 10.5 to 11%, primarily by changing the hydraulic diameters of the various bypass flow channels. The results from the two calculations were nearly identical. Table 5-1 presents the calculated initial conditions compared to the operating conditions provided in the Preliminary Safety Identification Document. All of the calculated parameters were at or very near the desired values.

Table 5-1. Desired and calculated MHTGR steady-state conditions.

Parameter	Desired (PSID)	Calculated
Reactor power (MW)	350	350
Helium inlet temperature (°C)	258.6	258.6
Helium outlet temperature (°C)	687	687
Coolant flow rate (kg/s)	157.05	156.77
Total bypass flow (%)	10.5-11	10.7
Central reflector gap flow (%)	0.5	0.5
Fuel region gap flow (%)	1.0-1.5	1.3
Side reflector gap flow (%)	3.0	2.9
Reflector/core barrel gap flow (%)	3.0	3.0
Control rod hole flow (%)	3.0	3.0
Inlet pressure (MPa)	6.38	6.38
Core pressure drop (kPa)	31.4	32.0
RCCS heat removal (MW)	0.7	0.7

5.2 HTTF Thermal-hydraulic Modeling and Analysis

Steady-state modeling of the HTTF has been performed to address both thermal-hydraulic and thermal stress concerns. The analyses are considered scoping because the design has not been finalized, and not all material properties are known.

5.2.1 Background

The development of the RELAP5-3D input model has been an evolutionary process over the past two years as the design of the facility has been developed and refined. This section summarizes the principal steps taken in arriving at the current model, which is described in the next section.

The original HTTF scoping calculations used a modified MHTGR input model, similar to that described in the previous section, in which the height and radial dimensions were scaled down to ¼ size. Steady-state calculations were performed with this model at several different facility operating powers. Table 5-2 provides Reynolds numbers from the reference plant and from these scaled calculations; the MHTGR values in the table are from an earlier version of the input model than that described in Section 5.1.1. The original power for the HTTF was planned to be near 650 kW. As seen in the table, at this power flow through the various core channels was predicted to be laminar in the test facility, compared to turbulent in the MHTGR. The lower heat transfer coefficients associated with the laminar flow resulted in an undesirable radial temperature distribution in the experiment facility, with the reflector temperatures much closer to the core temperatures than was the case for the MHTGR. To ensure that the flow in at least the core channels remained turbulent, so that the steady-state temperature distribution would be closer to that in the reference plant, the HTTF power was upgraded to 2.2 MW.

With an increased power, the core was redesigned. Several iterations were made addressing the number, size, and location of the heater rod holes and the various coolant channels in the core and reflector regions. RELAP5-3D sensitivity calculations were performed to determine the bypass flow provided by different numbers and sizes of control rod holes in the reflectors. The impetus for this study was the desire to avoid placing orifices at the coolant channel inlets in the upper plenum; not having orifices simplifies the design and operation of the facility. Table 5-3 shows results from some of these sensitivity calculations at a power of 2.0 MW.

Table 5-2. Calculated steady-state Reynolds numbers for the scaled MHTGR model.

Flow Channel	MHTGR	Scaled Model Power			
		500 kW	700 kW	1500 kW	2000 kW
Gap 0-1	2367	2	3	10	21
Gap 1-2	2317	2	3	10	20
Reflector holes	18755	241	335	868	1264
Fuel Ring 3	37171	779	1162	2670	3570
Fuel Ring 4	37849	781	1162	2683	3578
Fuel Ring 5	37314	844	1231	2696	3630
Gap 5-6	2108	2	3	10	20
Gap 6-7	2372	2	3	13	25
Gap 7-8	2408	3	4	16	31
Core barrel gap	12592	4	6	25	49

Table 5-3. Sample results from HTTF reflector hole size sensitivity calculations.

Parameter												
Number of central reflector holes	6	12	12	12	12	12	18	24	24	24	24	24
Central reflector hole diameter (in.)	0.94	0.94	0.5	0.5	0.5	0.5	0.5	0.5	0.5	0.5	0.5	0.5
Number of side reflector holes	24	24	24	24	36	48	48	48	60	72	84	96
Side reflector hole diameter (in.)	0.94	0.94	0.94	0.5	0.5	0.5	0.5	0.5	0.5	0.5	0.5	0.5
Core bypass flow (%)	18	21	16	5	7	8	10	9	11	12	13	15

CFD calculations using the STAR-CCM+ computer code were also performed at this stage to estimate the temperature distribution in the block, so that potential hot spots could be identified and mitigated. These calculations used a one-sixth symmetry model of the core blocks and assumed an adiabatic boundary at the edge of the block. Figure 5-7 shows the calculated temperatures in the block near the bottom of the core with the base model, and Figure 5-8 shows temperatures in the same location with a different control rod hole pattern. The first figure indicates that there may be significant temperature variations in the side reflector, that the central reflector is very hot, and that hot spots are located near the peripheral heater rods that have relatively few cooling channels around them. The second figure shows a more uniform temperature distribution in the reflectors, with a marked decrease in the temperature peaking around the peripheral heater rod locations.

But Figure 5-8 also shows a remaining problem: the reflectors are hotter than the core, because there are heater rods on the core periphery that are in direct contact with the reflectors. To eliminate this distortion, the core was again redesigned, this time placing six coolant holes around each heater rod. Because the control rod holes were no longer needed for core cooling, they were moved away from the core to represent the core bypass flow. RELAP5-3D sensitivity calculations were performed again to estimate the total core bypass flow provided by different sizes of holes. A second issue was trying to make the core channel helium outlet temperatures as uniform as possible by using different size holes around the peripheral heater rods. RELAP5-3D calculations were used to confirm that the proposed channel diameter variations would provide a relatively uniform helium outlet temperature across the core. This version of the input model is described further in the next two sections.

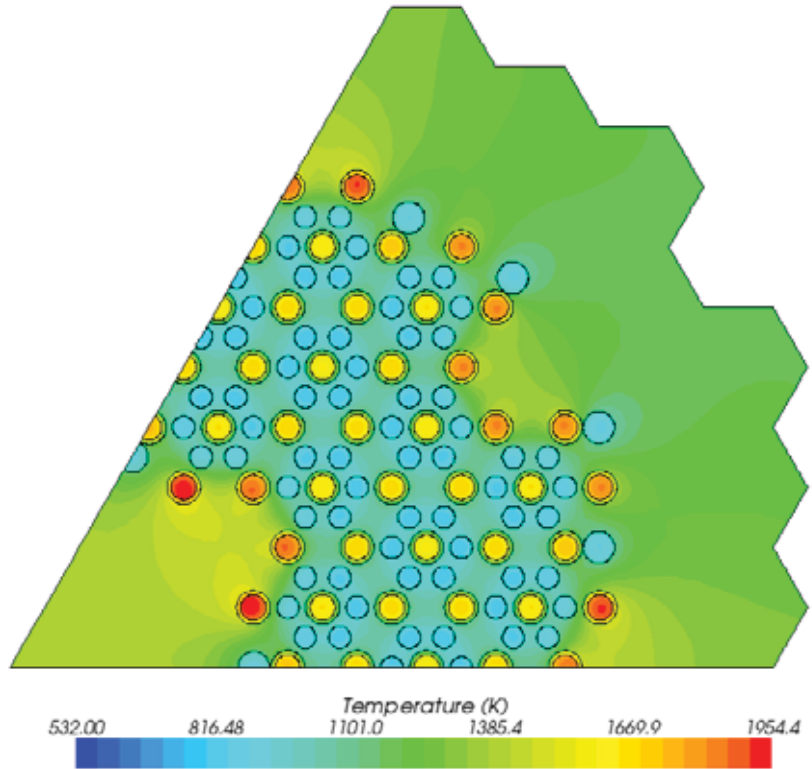


Figure 5-7. Calculated HTTF temperatures in the bottom portion of the core for the 2.2 MW base case.

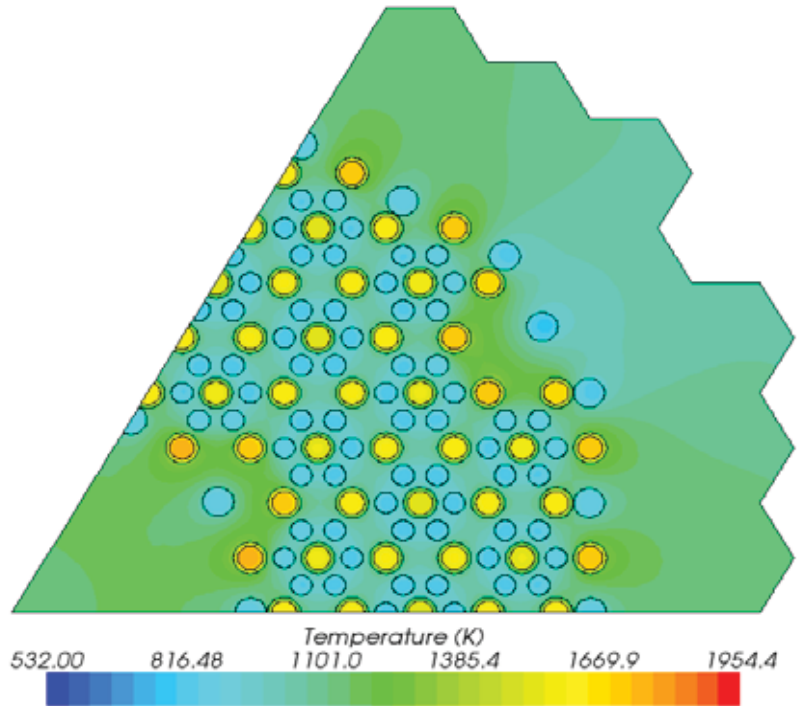


Figure 5-8. Calculated HTTF temperatures in the bottom portion of the core for the 2.2 MW control rod hole sensitivity case.

5.2.2 RELAP5-3D Input Model

The RELAP5-3D input model for the HTTF was developed with the objective of being as consistent with the MHTGR input model as practical, just as the objective of the facility is to be as representative of the reference plant as scaling will allow. The focus of the model was the reactor vessel; a simplified RCCS was modeled as heat structures with a constant surface temperature of 71.85°C on the back (nonradiating) side. Flow boundary conditions were applied at the reactor vessel flow inlet and outlet. The input model is based on design information available as of November 2011.

Figure 5-9 shows the reactor vessel nodalization for the model. The model is similar to the MHTGR model, but with no coolant risers and fewer flow paths inside the core barrel. The inlet flow proceeds up through the annulus between the reactor vessel and the core barrel, enters the upper plenum, flows down through the coolant channels in the core and reflector to the outlet plenum, then exits the vessel into the hot duct. Note that the gaps on either side of the permanent side reflector (Components 164 and 166) are only connected to the outlet plenum, as the upper plenum plate prevents flow from entering the tops of these channels.

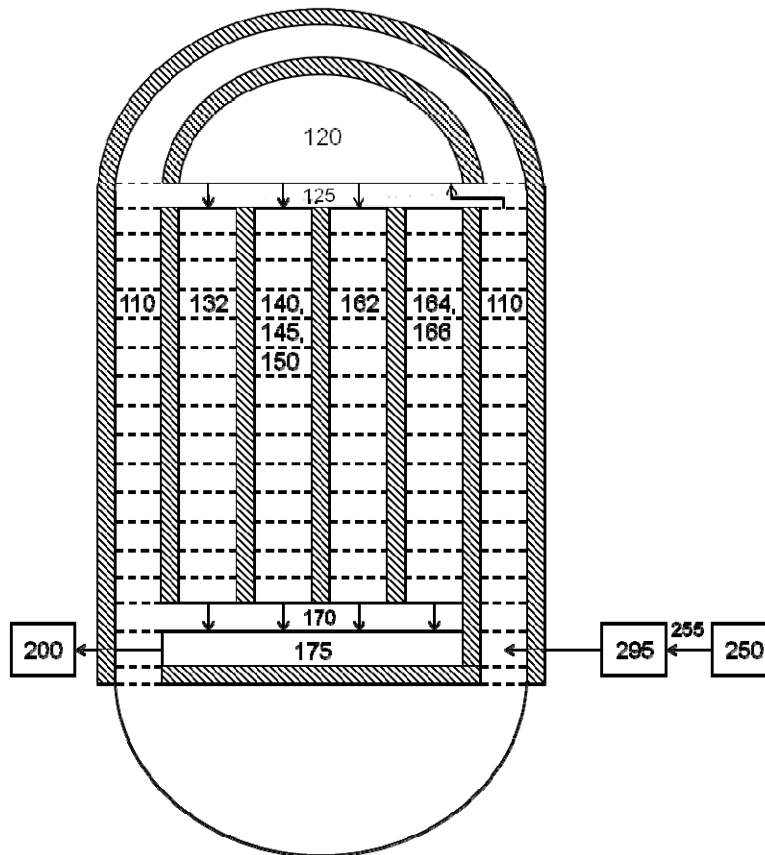


Figure 5-9. RELAP5-3D nodalization of the HTTF reactor vessel.

A cross-section of the model in the core region is shown in Figure 5-10. The central reflector is modeled in three parts: a solid-center cylinder, a middle ring containing six 1.9-cm (0.75-in.) diameter control rod holes, and a solid outer ring. Figure 5-11 shows how this middle region is modeled, as a number of coolant holes are surrounded by a proportional amount of ceramic material. The core region is modeled as three rings containing heater rods, coolant holes, and ceramic. The unit cell modeled in these regions is also shown in Figure 5-11. The heater rod is modeled as a heat structure that radiates to the ceramic surrounding a coolant hole. The side reflector was modeled similarly to the central reflector, with two solid ceramic rings on either side of a middle ring containing 36 1.59-mm (0.625-in.)-diameter holes. The permanent side reflector was separated from the side reflector by a 2.0-mm (0.079-in.) gap and from the core barrel by a 3.18-mm (0.125-in.) gap. Heat transfer between the core and central and side reflectors was modeled using conduction enclosures, with radiation modeled across the gaps between the other structures. Axial conduction was modeled using either the 2-D conduction model in the code or conduction enclosures.

The heater rods were all assumed to have the same power and a flat axial power shape. Flow resistance through the reflector cooling holes was adjusted to provide a total core bypass flow of about 11%. The core ceramic material was assumed to be Greencast-94 F Plus and the permanent side reflector ceramic was assumed to be Thor 80.

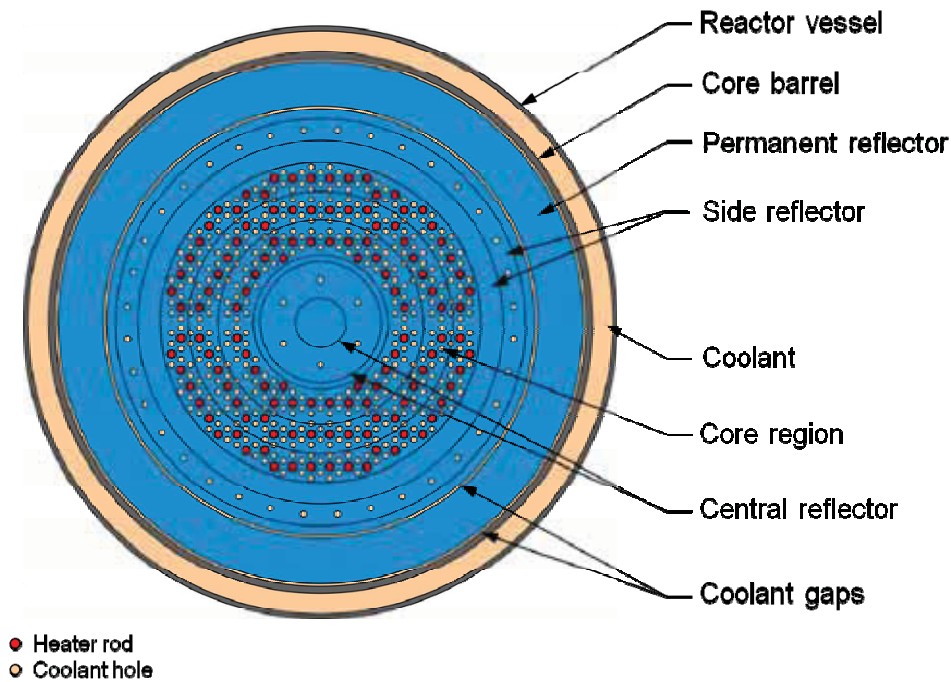


Figure 5-10. Cross-section of the RELAP-3D model of the HTTF reactor vessel.

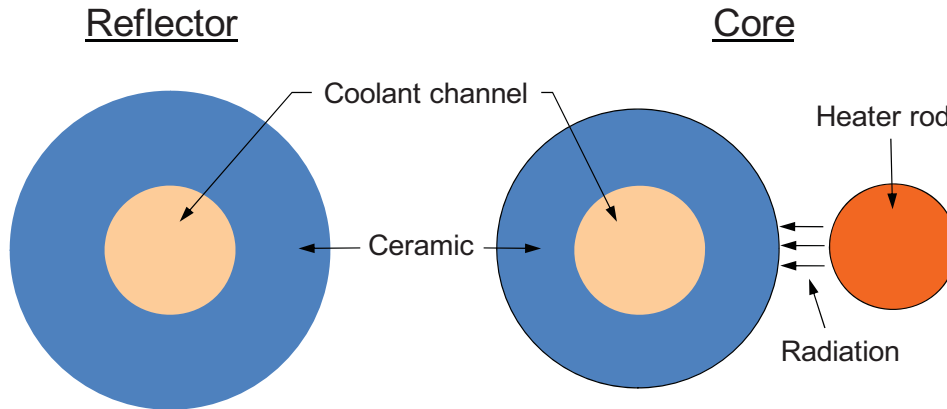


Figure 5-11. Unit cells used in the RELAP5-3D model of the HTTF reactor vessel.

5.2.3 Steady-State Calculations

A steady-state calculation was performed. No adjustments to the model were made, as there are no data with which to benchmark the input model. Tables 5-4 through 5-7 compare various parameters from this calculation to those from the reference MHTGR steady-state calculation.

General system parameters are contained in Table 5-4. With the same coolant inlet and outlet temperatures, the HTTF flow rate is reduced proportionately with the power. The predicted core bypass fraction in HTTF is a bit higher, but still well within the anticipated range of bypass flows over the course of an MHTGR operating cycle (10 to 25%) as the graphite block dimensions change during irradiation. One parameter that is distorted in these scoping models is RCCS heat removal. During steady-state operation, the parasitic heat loss in the MHTGR is 0.2% of the core power, while it is 2.3% in the HTTF. This percentage may change as more information on the RCCS operation is developed and incorporated into the RELAP5-3D input model. Also, the HTTF cannot operate at the full scaled (1/32) power of 10.9 MW, which would reduce the RCCS heat loss to 0.5%.

Table 5-4. Calculated steady-state conditions for the HTTF and MHTGR.

Parameter	HTTF	MHTGR
Reactor power (MW)	2.2	350
Reactor vessel helium inlet temperature (°C)	258.6	258.6
Reactor vessel helium outlet temperature (°C)	687	687
Coolant flow rate (kg/s)	0.965	156.77
Core bypass flow (%)	12.0	10.7
Reactor vessel inlet pressure (MPa)	0.70	6.38
Core pressure drop (kPa)	1.7	32.0
RCCS heat removal (MW)	0.05	0.7

Table 5-5 shows Reynolds numbers for the five flow channels through the HTTF core and reflectors; the gaps on either side of the permanent side reflector are blocked at the top, and thus are not active flow paths. The values in the HTTF core region are an order of magnitude lower than those in the MHTGR, but are still in the turbulent regime. The flow in the HTTF reflector coolant holes is also turbulent, with Reynolds Nos. 2 to 3 times higher than those in the MHTGR 1-mm gaps between the blocks, and about half that of the MHTGR flow between the core barrel and the permanent side reflector.

Table 5-5. Calculated HTTF and MHTGR steady-state Reynolds numbers.

Flow Channel	HTTF	MHTGR
Central reflector coolant holes (HTTF) or gaps (MHTGR)	8376	2543
Fuel ring 3	3835	40726
Fuel ring 4	4249	41850
Fuel ring 5	3636	40824
Side reflector coolant holes (HTTF) or gaps (MHTGR)	7049	3160
Core barrel gap	0	16786

Coolant channel outlet helium temperatures are provided in Table 5-6. The central and side reflector bypass channel temperatures presented for the MHTGR are flow-weighted average values for the gaps and control rod channels. The objective to have fairly uniform temperatures across the core appears to have been met, with an 11°C spread in the HTTF and 18°C in the MHTGR. The bypass channel outlet temperatures are reasonably close. The helium at the bottom of the gap between the permanent side reflector and core barrel is hotter in HTTF than in the MHTGR because this is stagnant flow region in the experimental facility.

Table 5-6. Calculated HTTF and MHTGR steady-state core channel outlet helium temperatures (°C).

Flow Channel	HTTF	MHTGR
Central reflector bypass	455	485
Fuel ring 3	741	731
Fuel ring 4	731	713
Fuel ring 5	730	726
Side reflector bypass	358	346
Core barrel gap	329	283

Calculated temperatures averaged over the heated length of the core are shown for various structures in Table 5-7. The temperatures in the fuel rings are those of the ceramic (HTTF) or graphite moderator (MHTGR), not those of the fuel or heater rods. The core region temperatures are much higher in the HTTF than in the MHTGR for several reasons: the heat transfer coefficient is more than six-times smaller because of the lower Reynolds number, the thermal conductivity of the ceramic is about ten-times lower than that of graphite, and the thickness of the ceramic between the coolant hole and heater rod hole is about 40% larger than the corresponding graphite thickness in the MHTGR. The MHTGR temperature in Fuel Ring 4 is somewhat depressed because this graphite is cooled by the gap flow between the blocks as well as by the helium flowing through the coolant channels in the block. The reflectors are also hotter in HTTF, especially in the central reflector. The MHTGR has gaps between each ring of blocks that allow for incremental radial cooling that the discrete cooling holes in HTTF cannot reproduce. There is a potentially large uncertainty in the RELAP5-3D input model in how the conduction in the reflectors is modeled, as the 2-D RELAP5-3D model is not well suited to model the heterogeneity associated with the discrete cooling hole locations, particularly in the central reflector. System characterization data will be needed for benchmarking the RELAP5-3D input model.

Table 5-7. Calculated HTTF and MHTGR steady-state structure axial average temperatures (°C).

Structure	HTTF	MHTGR
Central reflector center column	500	399
Central reflector middle ring	474	419
Central reflector outer ring	645	425
Fuel ring 3	786	603
Fuel ring 4	795	588
Fuel ring 5	754	602
Side reflector inner ring	543	385
Side reflector middle ring	358	—
Side reflector outer ring	344	327
Permanent side reflector	316	282
Core barrel	263	278
Reactor vessel barrel	242	217

5.2.4 Thermal Stress Analysis

A concern was raised about the structural viability at operating temperature of the ceramic material used in constructing the core for the HTTF at OSU. The thermal stresses that will be imposed on the ceramic will actually be caused by temperature gradients. Such gradients will occur between the high temperatures of the heat rods and the lower temperatures of the coolant channels, the center reflector, and the outer walls. While it may be the case that higher temperature gradients are possible during the heat-up prior to a steady-state test, it was decided to first perform a stress analysis on the ceramic material at its projected steady-state operating temperature.

The design and layout of the coolant and bypass channels in the HTTF core has undergone a series of reconfigurations. Though some relatively minor modifications may still occur to the design of the core, the configuration on which the presently reported calculations are based should be close to the final design. It was determined to perform the stress calculations using a commercial finite-element stress analysis code. However, it was further determined that the temperature distribution would be computed using a conjugate flow and heat transfer analysis with a commercial CFD code. Upon completing the CFD analysis, the calculated temperatures would then be transferred for use by the stress analysis code. The mesh used in the stress code, though different than that used in the CFD code, has about the same mesh density. The CFD code is used to map or interpolate the temperature distribution onto the stress mesh as described below.

5.2.4.1 CFD Model

In order to be able to perform stress analysis for the thermally stressed ceramic in the HTTF core, the temperature distribution of the ceramic is needed. The temperature of the HTTF core for steady-state conditions is computed for the conjugate fluid flow and heat transfer problem using a fine-grid CFD model. The calculations are made using the commercial CFD code STAR-CCM⁺ [STAR-CCM+ 2010]. Temperature dependent properties are used for the helium coolant. Material properties for ceramic Greencast 94F are used for the core. These properties are supplied by the manufacturer. While the CFD model does not include the permanent side reflector, information from a RELAP5 [RELAP5-3D Development Group 2005] calculation, which did include the side reflector, for the outer temperature boundary condition is used. For the RELAP5 model, properties used for the permanent side reflector are

those for ceramic Thor 80. The configuration for the HTTF core is Revision E, with an overall hexagonal shape for the core (excluding the permanent side reflector).

The CFD model is run iteratively, adjusting the pressure drop across the core, until the overall mass-averaged outlet temperature is approximately 960 K, based on a 528 K inlet temperature. Properties for Greencast 94F and the heater rod material used in the CFD model are as follows:

- density = 2930 kg/m³
- heat capacity = 1200 J/kg K
- thermal conductivity = function of T (W/m K) as shown in Figure 5-12.

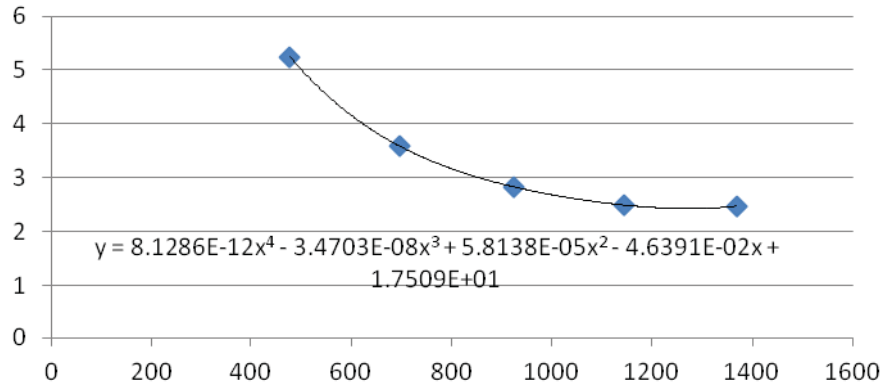


Figure 5-12. Thermal conductivity (W/m K) of Greencast 94F as a function of temperature (K).

Material properties used for the heater material:

- density = 1800 kg/m³
- heat capacity = $4.041 \times 10^{-14} T^5 - 4.464 \times 10^{-10} T^4 + 1.964 \times 10^{-6} T^3 - 0.004353 T^2 + 5.062 T + 471$ J/kg K
- thermal conductivity = $0.0166 T + 14.204$ W/m K.

Details for the CFD model include the following:

- All heater rods have the same power (1.8443×10^7 W/m³, 2.188 MW total, 210 heater rods).
- The axial power profile is flat.
- The coolant used in the model is helium. Helium properties, (obtained from the National Institute of Standards and Technology (NIST) [NIST 2010]) at 700 kPa are used. The properties for density, thermal conductivity, and dynamic viscosity are fitted to curves, which curves are used in the CFD code. The properties are valid from 300 to 2200 K.
- The helium inlet temperature is set to 528 K.
- The inlet boundary condition is set to stagnation pressure at 1,370 Pa; the outlet pressure is set to 0 Pa. To obtain the absolute pressure, a reference pressure of 698.552 kPa must be added to the above pressures. The pressure losses at coolant channel inlets and outlets are part of the solution.
- A one-twelfth sector of the HTTF core is modeled with symmetry boundary conditions on the sides of the model. Figure 5-13 shows the layout of the CFD model showing the upper reflector toward the upper left, the heated core in the middle, and the lower reflector toward the lower right. Figure 5-14 provides a cross sectional view of the CFD model indicating the locations of the inner and outer

bypass channels (which function as coolant channels), the normal coolant channels and the heater rods, each surrounded by a narrow annulus filled with stagnant helium.

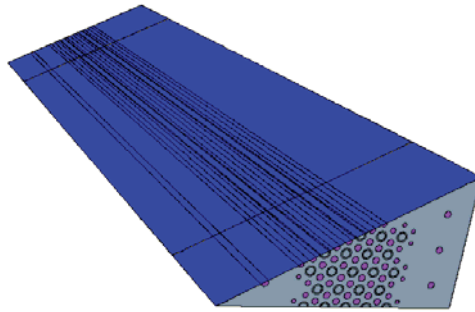


Figure 5-13. Illustration of the CFD model for the 1/12 sector.

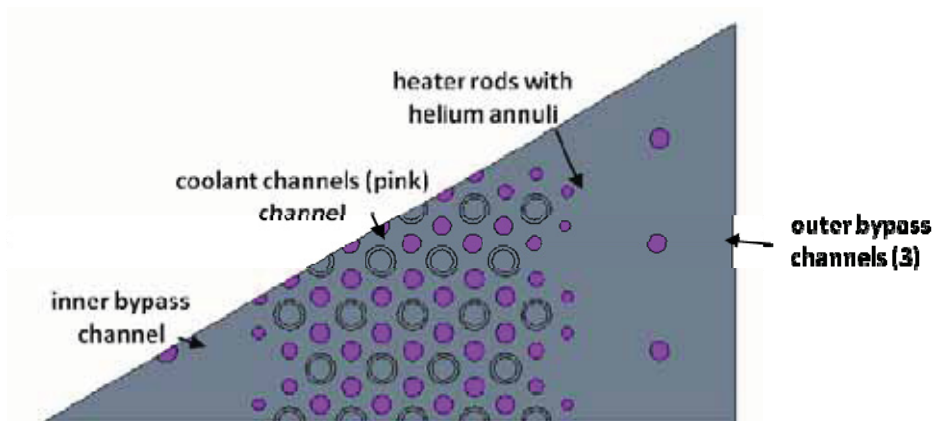


Figure 5-14. Cross sectional view of the CFD model.

- The outer boundary is based on temperatures computed from a RELAP5 model, which includes the permanent side reflector. Hence, the inner surface of the permanent side reflector represents the outer surface of the CFD model. The axial (vertical) temperature distribution computed by RELAP5 and used for the outer boundary condition for the CFD model is shown in Figure 5-15.

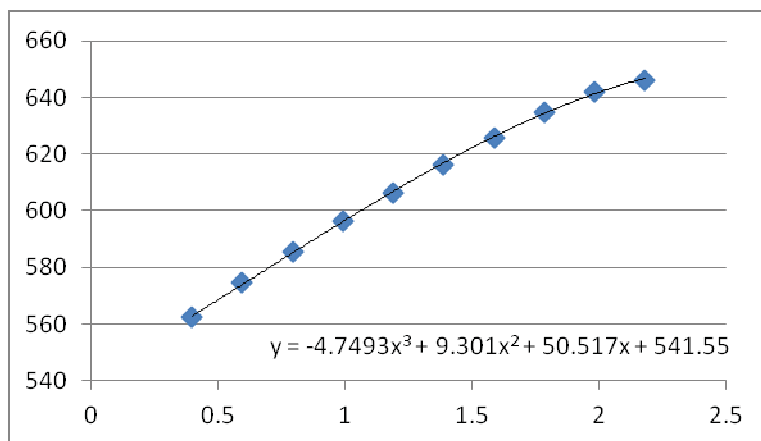


Figure 5-15. Temperature (K) distribution along the vertical edge of the permanent side reflector (m) (temperature increasing with core depth as measured from the top).

- The inlet and outlet faces of the core are adiabatic.
- There are continuous flow paths through the HTTF, with no junctions between disks.
- The initial 0.2974 m of core is unheated (upper reflector).
- The following 1.9825 m of core is heated.
- The last 0.4 m of core is unheated (lower reflector).
- The realizable two-layer $k\text{-}\epsilon$ turbulence model with the two-layer all y^+ wall treatment are used for the coolant flow in the model. This turbulence model has produced excellent results for wall shear stress and heat transfer coefficient for turbulent flow in smooth tubes [Tung et al 2011].
- The annuli between the 0.75-in.-dia. heater rods and the 1.0-in.-dia. holes in the core that contain the heater rods are assumed to filled with stagnant helium.
- The inner bypass channel is 0.75 in. in diameter.
- The three outer bypass channels are 0.625 in. in diameter.
- The coolant channels surrounding the heater rods vary from 0.375, to 0.5, to 0.625 in.
- The CFD mesh has about 18.1 million cells.

5.2.4.2 Results for Temperature Distribution in HTTF

The mass flow and temperatures of the simulation are given in Tables 5-8 and 5-9 and compared to those of the RELAP5 calculation. Figure 5-16 illustrates the temperature contours in a plane in the ninth disk, which is the hottest disk in the core. Figure 5-17 shows a close-up view of the temperature contours in the ceramic only and the mesh. The larger circles are the locations of the heaters; the smaller circles are the locations of the coolant channels. The close-up is taken from the approximate center of the CFD model. Note that it is the temperature *gradient* that creates the thermal stresses.

The temperature field computed by STAR-CCM+ is then transferred to stress analysis code ABAQUS/Standard [ABAQUS 2010]. This is accomplished by reading an input file from ABAQUS/Standard which contains mesh information for the ABAQUS/Standard mesh. The temperatures are then mapped onto the ABAQUS/Standard grid from the CFD grid and output to a file that can be read by ABAQUS/Standard. Figure 5-18 plots the temperature computed by the CFD code compared to that which has been remapped (interpolated onto) the ABAQUS/Standard mesh, giving an indication of the accuracy of the remapping procedure.

Table 5-8. Mass flows and exit temperature: HTTF coolant channels for CFD and RELAP5 results.

Parameter	Inner Bypass		Outer Bypass		Main Coolant Chans.	
	RELAP5	CFD (x12)	REALP5	CFD (x12)	RELAP5	CFD (x12)
Mass flow (kg/sec)	0.01712	0.02701	0.09868	0.10048	0.84983	0.838305
Exit Temp (K)	728.4	665.9	630.4	640.6	1003.0–1014.5	1007.5

Table 5-9. Overall mass flows and temperatures for the CFD results compared to RELAP5 results.

Parameter	Total mass flow (kg/sec)	Inlet temperature (K)	Mass average outflow temp (K)	Total energy input (MW)
RELAP5	0.96545	528.8	960.15	2.2
CFD	0.9658	528	959.79	2.188

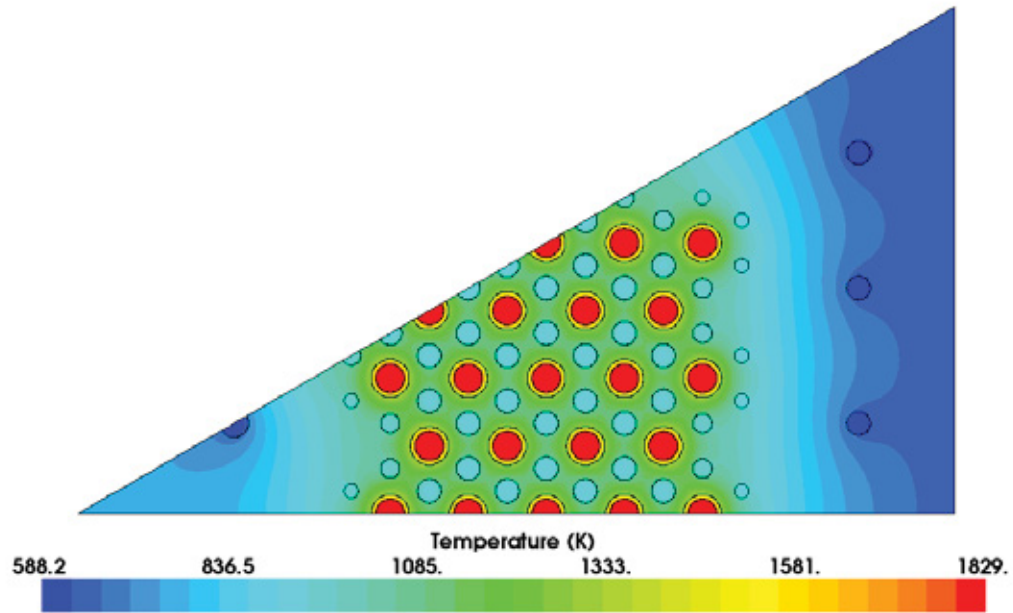


Figure 5-16. Temperature contours in the plane of the ninth lowest disk.

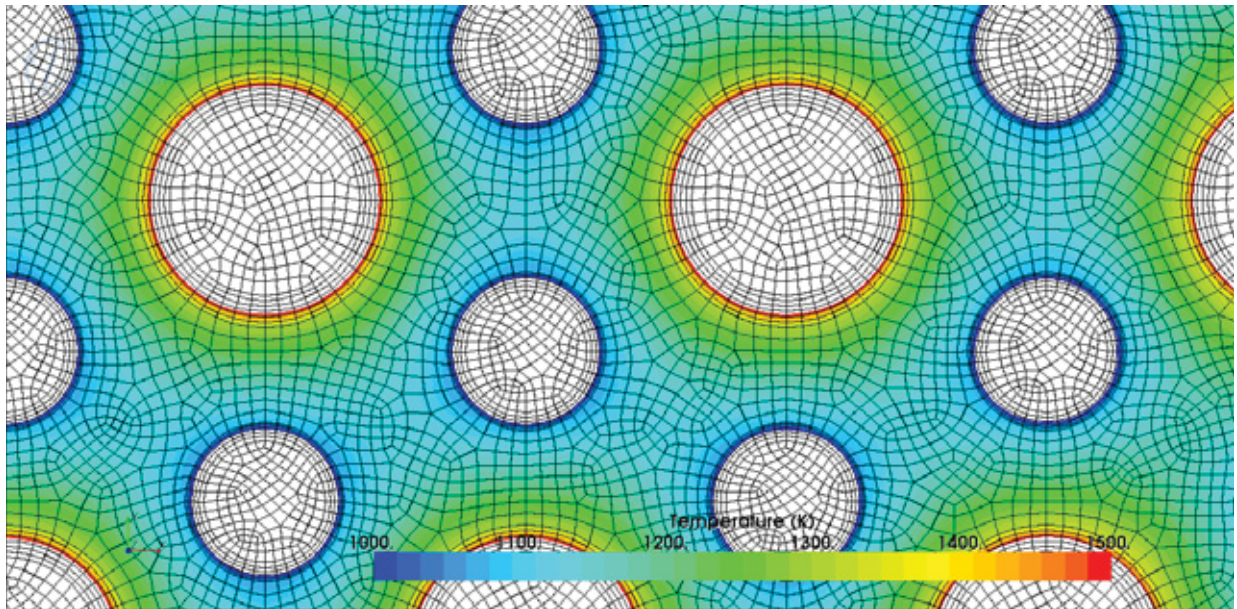


Figure 5-17. Close-up view of temperature contours in the ceramic core and the mesh for the CFD result.

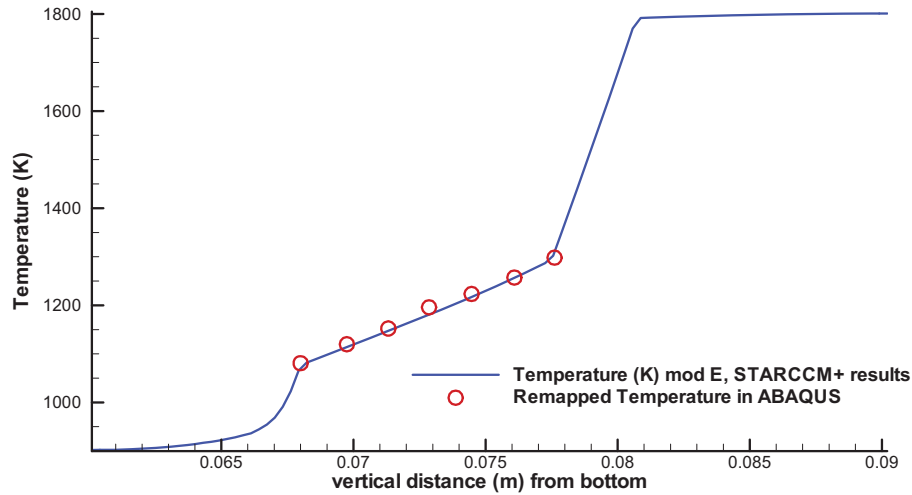


Figure 5-18. Comparison of temperature computed using CFD code to that remapped onto the stress analysis mesh.

5.2.4.3 Thermal Stress Analysis

A finite element model of a section of the ninth disk was created using I-DEAS NX6 [I-DEAS 2010]. This finite element model (see Figure 5-19) uses standard brick or hexahedral elements. The model was meshed with a density that approximated the STAR-CCM+ mesh used to obtain the temperature distribution for the ceramic core. The elements have an aspect ratio of about 8:1 in the Z or axial direction since the temperature gradient is very gradual in this direction. This finite element model was converted to an ABAQUS/Standard input file and solved for thermal stresses resulting from thermal gradients.

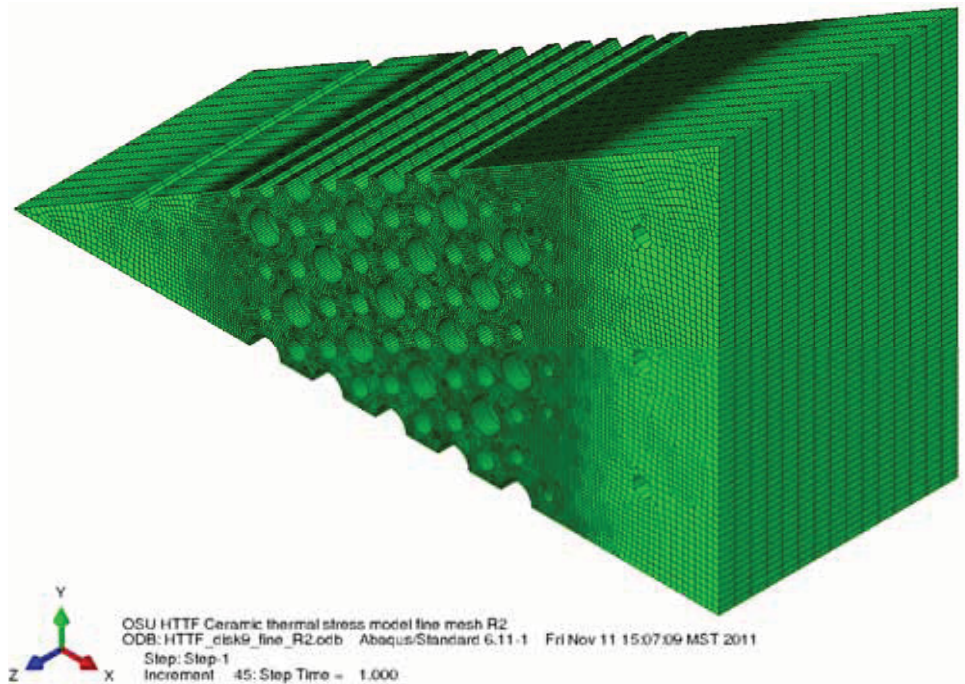


Figure 5-19. ABAQUS/Standard finite element mesh of a section of ninth disk.

This model of 1/12th of the disk uses symmetry boundary conditions to represent the entire disk. The bottom face was restrained from movement in the Y-direction as shown in Figure 5-19 for the coordinate system orientation. The whole part was restrained from movement in the Z-direction by weak springs in each of the three corners. All of the nodes on the slanted upper face were placed in a transformed coordinate system where the transformed X-axis runs along the corner of the upper face and the front face of the model and the transformed Y-axis is perpendicular to the upper face. The Z-axis remained unchanged. Using this transformed coordinate system, the nodes on the upper face were restrained from movement perpendicular to the face. This restrained the model from movement in the X-direction while allowing radial thermal expansion to occur.

The input file for this finite element model was used to map the temperatures from STAR-CCM+, as described above. STAR-CCM+ returned a file that mapped the calculated temperatures to the nodes in this model (Figure 5-20). Figure 5-21 shows a close-up view of the temperatures in the center part of the model.

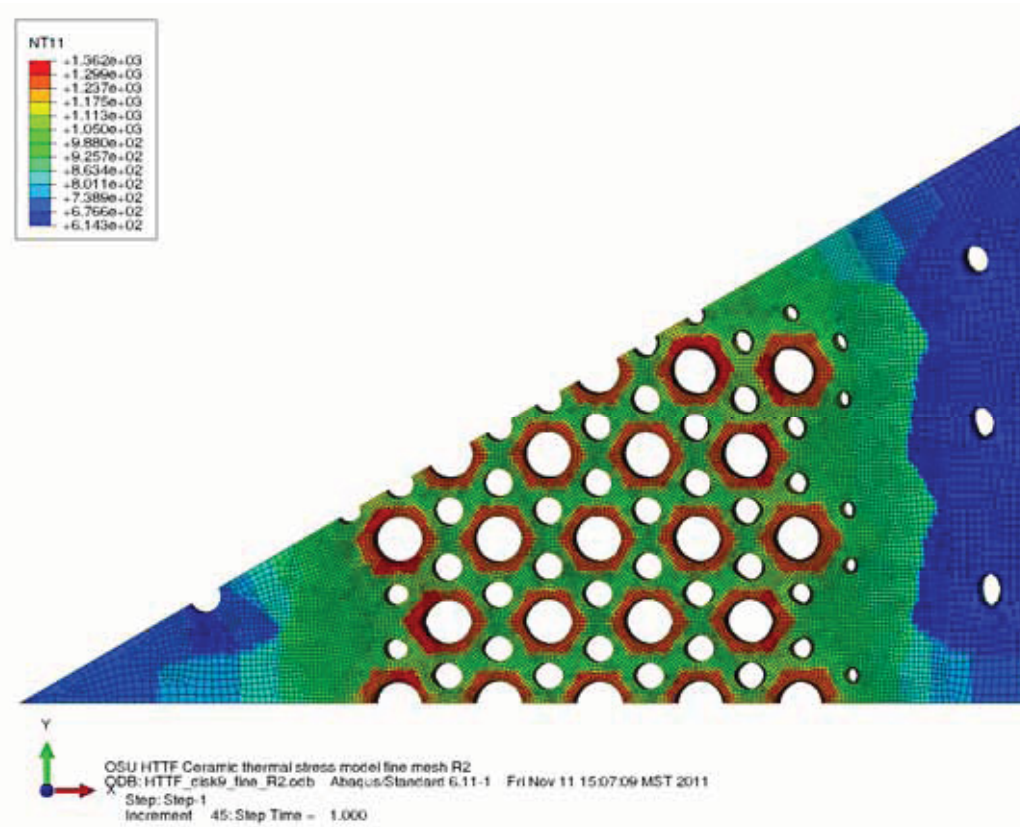


Figure 5-20. STAR-CCM+ model temperatures (K) mapped onto the ABAQUS/Standard model.

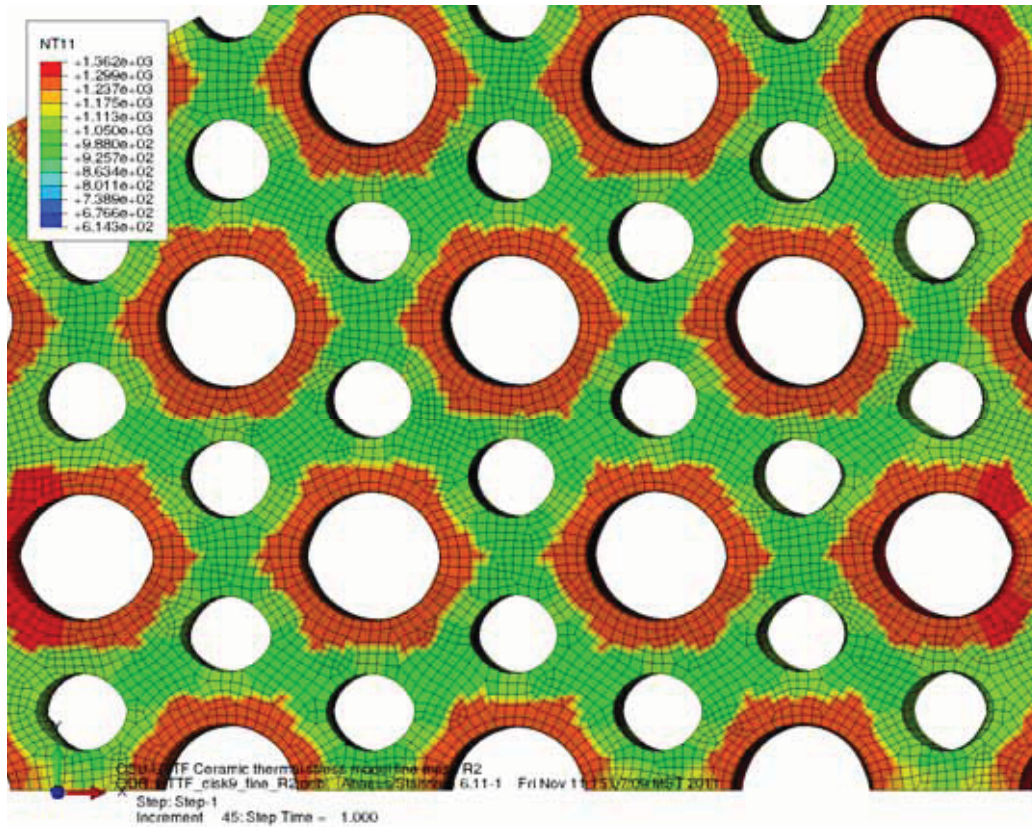


Figure 5-21. Close-up view of the mapped temperatures (K) in the ABAQUS/Standard model.

5.2.4.4 Material Properties

The Greencast 94F cast ceramic material was modeled as an elastic-perfectly plastic material, meaning that the material was treated as a linear elastic material until the yield strength was reached and then it was perfectly plastic. This permitted the elements that exceeded the yield strength to be displayed with plastic strain (PEEQ) (Figure 5-24). The material properties shown in Table 5-10 and Figure 5-22 were furnished by B. Jackson (OSU) for use in this analysis.

Table 5-10. Greencast 94F material properties.

Material Property	Value		Units
Modulus of elasticity	4.2265E+10		Pa
Poisson's ratio	0.090		unitless
Density	2912.6		Kg/m ³
Thermal expansion	See Figure 5-22		1/K
Yield strength	17.2	1089 K	MPa
	19.3	1644 K	MPa
	23.4	1755 K	MPa

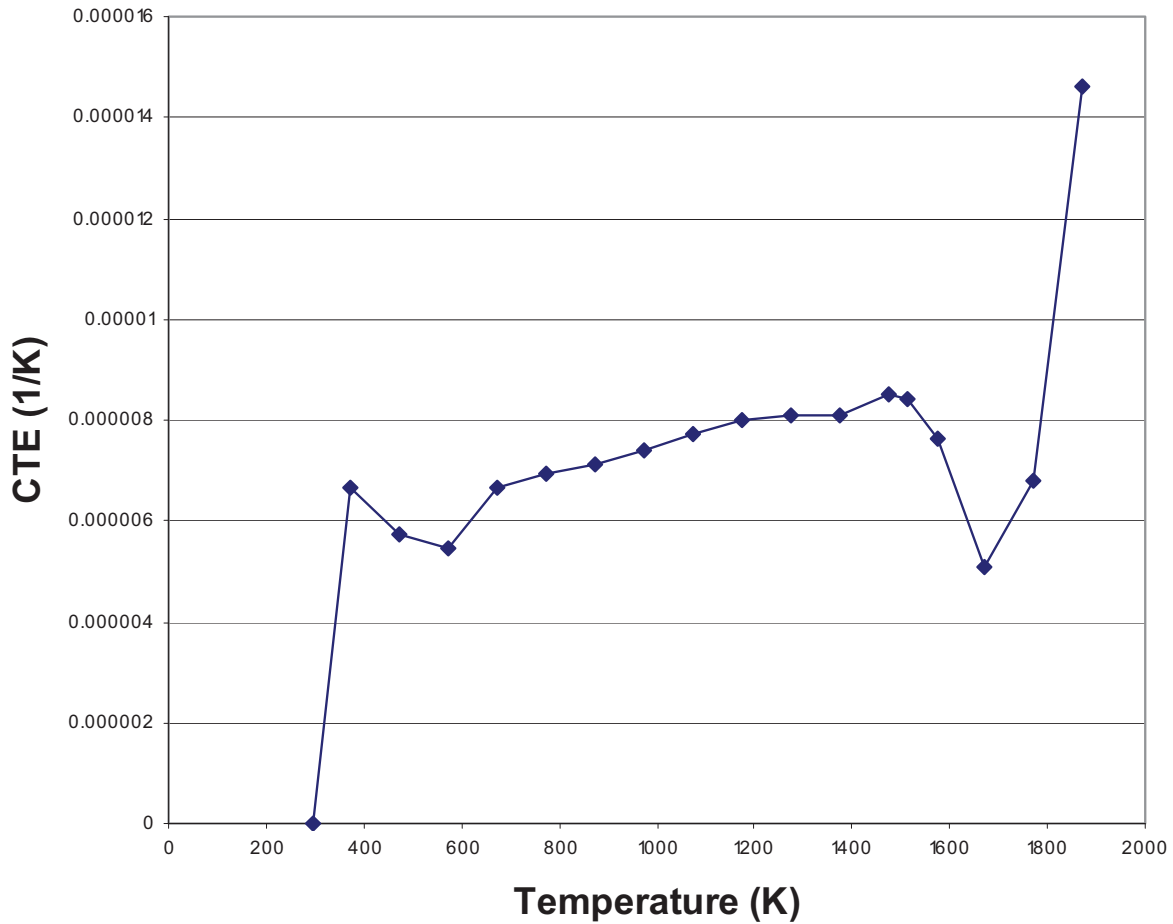


Figure 5-22. Measured coefficient of thermal expansion for Greencast 94F.

5.2.4.5 Results

Results of the thermal stress analysis using this model are shown in Figures 5-23 and 5-24. The calculated von Mises stress is shown in Figure 5-23. The stresses shown in Fig. 5-23 can be compared to the yield stresses in Table 5-10. The maximum stresses exceed the yield strength, which shows that plastic strain occurs in the model. Figure 5-24 illustrates the plastic strain. Wherever the plastic strain is above zero, the material has exceeded the yield strength calculated for that temperature and cracking is predicted to occur. Generally speaking, these predicted areas of cracking occur between the heater rod holes and the coolant channels. Figure 5-25 shows all elements where any plastic strain occurs. Exceeding the yield strength is an indication of cracking for brittle materials. However, it is expected that a small amount of plastic strain would occur in the ceramic before the onset of cracking. This would reduce the amount of cracking in the model. Figure 5-26 shows the calculated deformation in the model. The maximum movement (radially) is just over 3 mm.

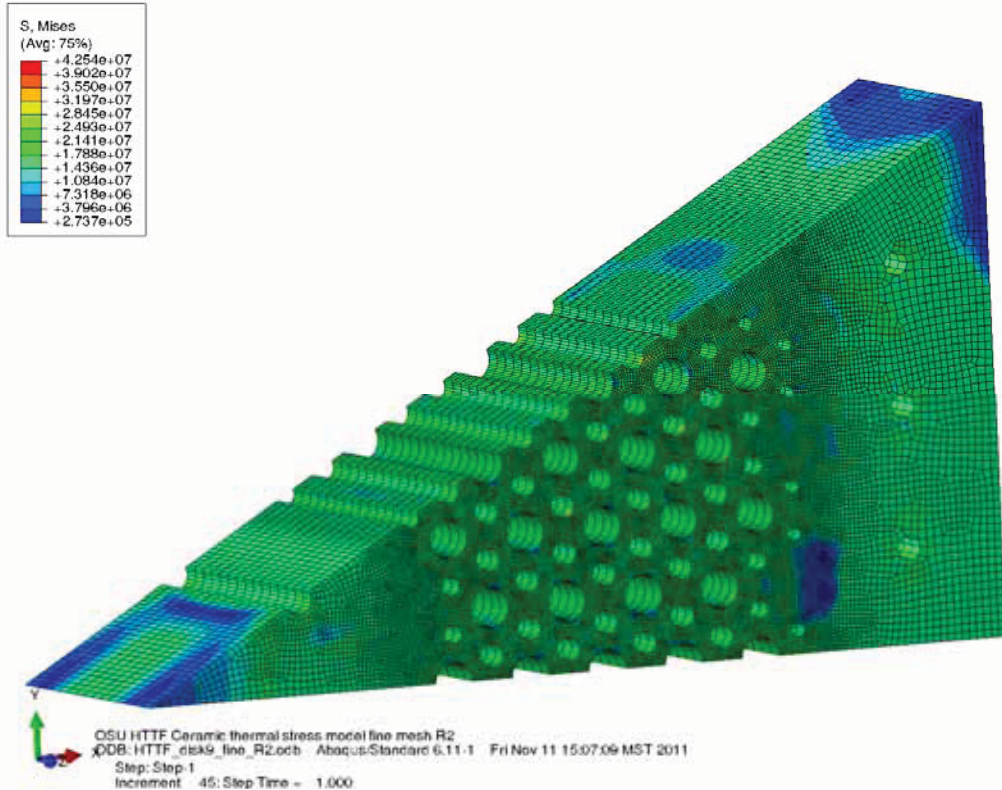


Figure 5-23. Calculated von Mises stress (Pa) in the Greencast 94F ceramic.

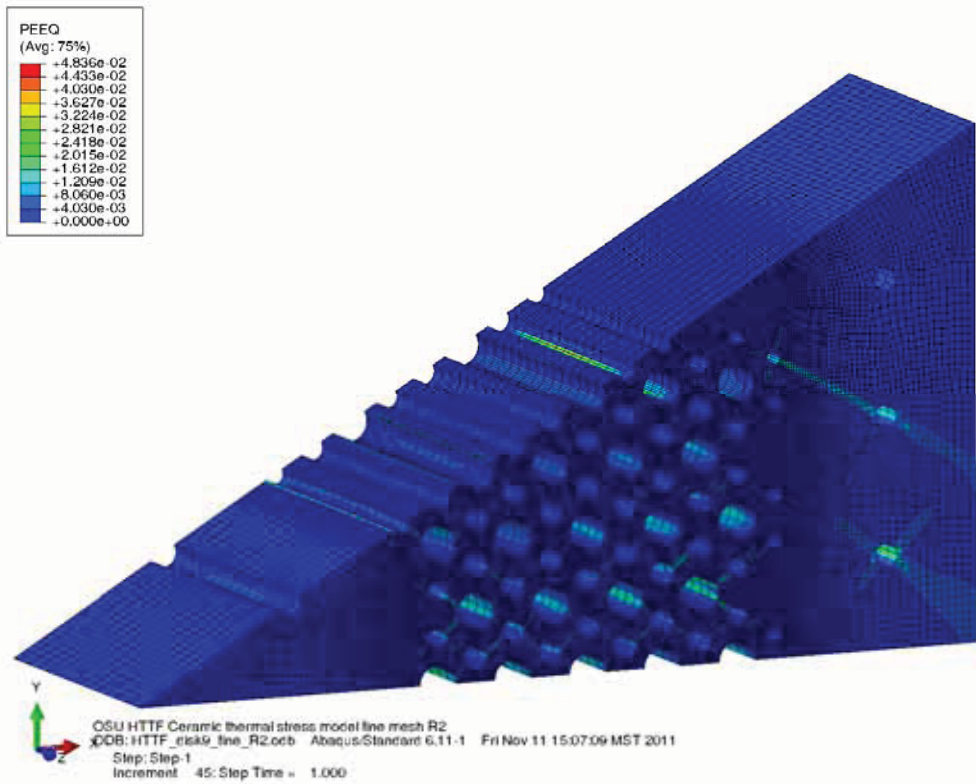


Figure 5-24. Calculated plastic strain from thermal expansion.

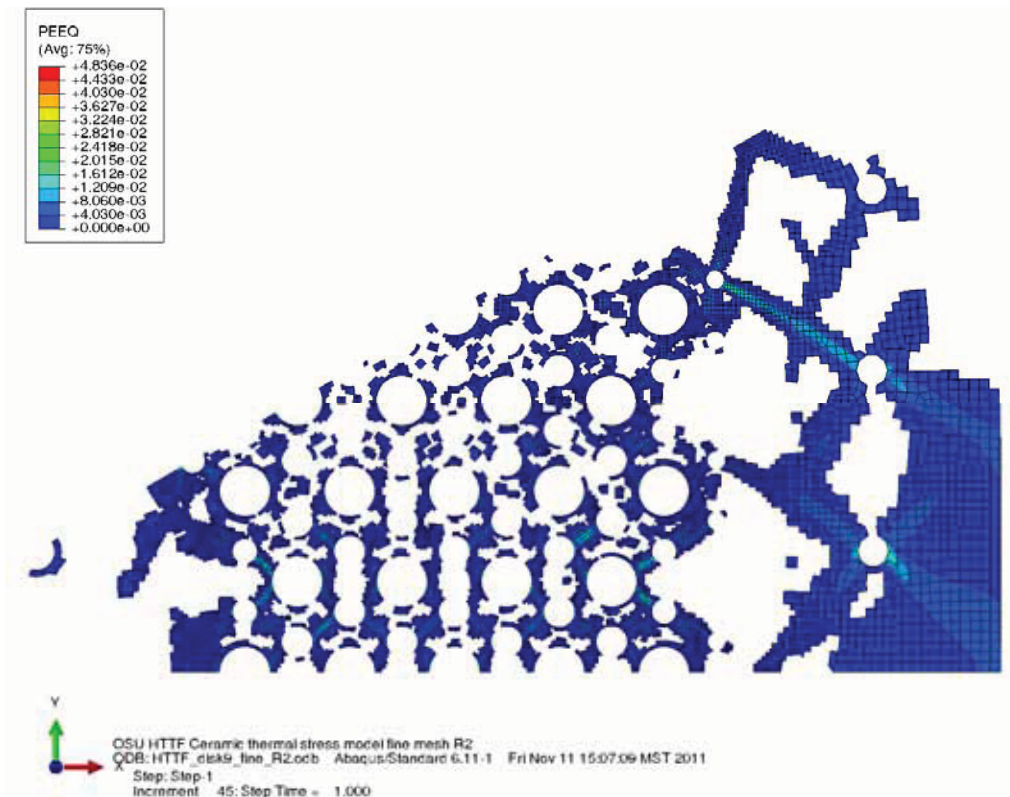


Figure 5-25. Elements exhibiting some degree of plastic strain.

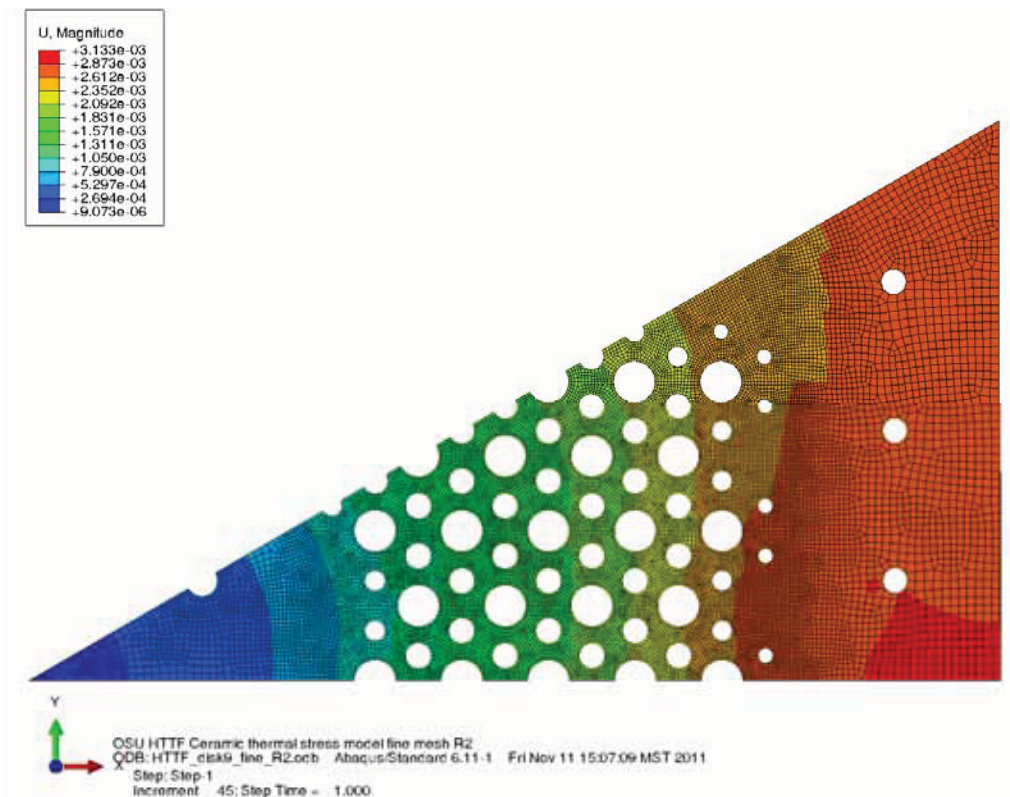


Figure 5-26. Calculated deformation (m) in the disk.

5.2.5 Summary

Steady-state simulations of the MHTGR and the HTTF have been performed. The calculations addressed the thermal-hydraulic behavior of both, as well as the thermal stress response of the HTTF.

Reference calculations of the MHTGR were performed using the RELAP5-3D computer code. The input model represented the reactor vessel, reactor cavity, and RCCS. The core and reflectors were modeled as a series of concentric rings with a coolant gap in between. The reflector rings containing control rod holes were further divided into two rings, one solid and one containing the holes. Unit cells based on a coolant channel were used to model the fuel blocks. Radiation and 2-D conduction were modeled to transfer heat from the core through the reflectors to the core barrel, reactor vessel, and RCCS. The RCCS was modeled as an air-cooled system with flow driven by natural convection.

The initial HTTF scoping calculations were performed with a scaled-down version of the MHTGR input model. These calculations identified a problem with the facility. With the facility at full power, with prototypical helium inlet and outlet temperatures, the flow through the core was laminar. This resulted in reduced heat transfer from the core to the coolant, which in turn caused the initial temperatures in the core and reflectors to be too high. The power was subsequently upgraded from 650 kW to 2.2 MW to alleviate this problem.

Sensitivity calculations using both RELAP5-3D and STAR-CCM+ were performed to help investigate the next HTTF core design. The RELAP5-3D calculations looked at how different combinations of reflector coolant holes affected the core bypass. The STAR-CCM+ calculations estimated the local temperatures in the core for several of the reflector coolant hole geometry options. These simulations indicated that significant hot spots could occur in the core and that the proposed arrangements of cooling holes resulted in the reflectors being hotter than the core ceramic.

These results precipitated another core redesign, resulting in the current model. RELAP5-3D sensitivity calculations were again performed to address the bypass flow provided by different cooling hole sizes and locations. Comparisons with the MHTGR steady-state calculations show good agreement with the overall conditions and with the helium temperatures at the entrance to the reactor vessel outlet plenum. Although the Reynolds numbers in the core are an order of magnitude lower than those in the reference plant, the Reynolds numbers are nevertheless representative of turbulent flow and the flow behavior anticipated in the HTTF can be linked to the behavior in the MHTGR using the scaling laws. The lower turbulent flow rates in the HTTF do result in reduced convective heat transfer; together with differences in thermal conductivity, this yields much higher structure temperatures in the core and reflectors than in the MHTGR. But again, the linkage between the HTTF and the MHTGR via the scaling laws enable defensible comparisons between the two to be performed. It is anticipated that data

Also at steady-state conditions, thermal stress analyses were performed to investigate the likelihood of catastrophic cracking in the ceramic core. These calculations indicate that some cracking will occur in the HTTF ceramic core. Although the calculational model is unable to predict the size or length of the cracks, visual observations based on heating ceramic samples in ovens at high temperatures have shown that the cracks will likely be surface cracks that do not penetrate the full thickness of the ceramic structures and furthermore will be narrow with rough walls and won't open free-flowing passages for the HTTF working fluid. The first plastic strain observed in the model occurred when the temperature was ramped up to about half of the final temperature, indicating that the temperatures would have to be reduced by about half to prevent the onset of any cracking. In anticipation that the cracking will materialize itself in the form of surface cracks, as noted above, it is unrealistic to try to operate the system to not have some cracks. Therefore, the test matrix will be tuned to chronologically perform the experiments in the order of lowest anticipated temperatures first followed by the higher anticipated

temperatures as the experimental program continues. Further analysis is needed to apply these calculational results to both design HTTF experimental operating guidelines and to more rigorously order the experimental test matrix.

6. STUDIES OF TRANSIENT SCENARIOS IN MHTGR AND HTTF USING RELAP5-3D

The two base transients simulated using the RELAP5-3D computer code are depressurized and pressurized conduction cooldowns. Comparable calculations were performed using both facility input models. A scoping initial heatup calculation for the HTTF was also performed. All of the simulations used the input models described in the previous chapter.

6.1 Depressurized Conduction Cooldown

After the desired steady-state conditions were achieved, simulations of DCC transients were performed. The DCC was modeled by imposing a 10-second depressurization to atmospheric pressure, after which both the reactor vessel inlet and outlet were open to helium-filled volumes at atmospheric pressure, simulating a break of the cross duct. This configuration results in a once-through natural convection pattern, with flow entering the outlet plenum from the break, being heated as it flows up through the core to the inlet plenum, then flowing down through the coolant risers (MHTGR) or the core barrel-vessel gap (HTTF) and out the break. A reactor scram signal was assumed to be generated at transient initiation. The calculations were terminated after all of the structure temperatures had reached their peaks and begun to cool down, at 168 hours for the MHTGR and 48 hours for the HTTF. Base case and sensitivity calculations were also performed.

6.1.1 Base Case Calculations

Figure 6-1 presents the MHTGR peak fuel temperatures. The inner and middle ring temperatures increase at the beginning of the transient, reaching peak values near 48 hours before beginning a slow decrease. The outer ring peak temperature initially decreases slightly before beginning a gradual heatup, reaching a peak value near 72 hours.

Figure 6-2 presents the HTTF peak heater rod temperatures. As in the MHTGR simulation, the inner and middle ring temperatures increased at the onset of the transient, while the outer ring temperature decreased. The basic shape of the curves, however, is somewhat different from that of the MHTGR. The overall peak temperatures are reached in the first 2 hours (at steady-state for the outer ring). The temperatures then slowly decrease before leveling off, or slightly increasing, at 6 hours. A subsequent peak occurs from 13 to 15 hours in all three regions, after which the temperatures decrease continually.

The core axial average temperature response, shown in Figures 6-3 and 6-4, is more similar. The temperatures all rise from the beginning of the transient; the middle ring starts with the highest temperature, but is soon surpassed by the inner ring for the rest of the simulation. In the MHTGR, the peak temperatures in the inner and middle rings occur near 60 hours, and are 300-350°C higher than the initial values. The outer ring peak occurs near 72 hours, about 200°C above the steady-state value. In the HTTF, the inner and middle ring temperatures peak near 15 to 16 hours, 100 to 200°C above the initial values, while the outer ring temperature peaks near 17 hours less than 100°C above its initial value.

Central reflector average temperatures are presented in Figures 6-5 and 6-6 for the MHTGR and the HTTF, respectively. In both facilities, the reflector ring nearest the core stays the hottest throughout the transient. In the MHTGR, the peak temperatures occur between 70 and 80 hours, peaking first nearest the core then working toward the center of the reflector. In the HTTF, the outer ring temperature peaks near 18 hours, with the other two rings peaking 3 hours later. The inner and middle ring temperatures are tied more closely together in the HTTF than in the MHTGR because the only cooling for the inner reflector is through the cooling holes in the middle ring, while in the MHTGR there are coolant gaps in contact with the center reflector column.

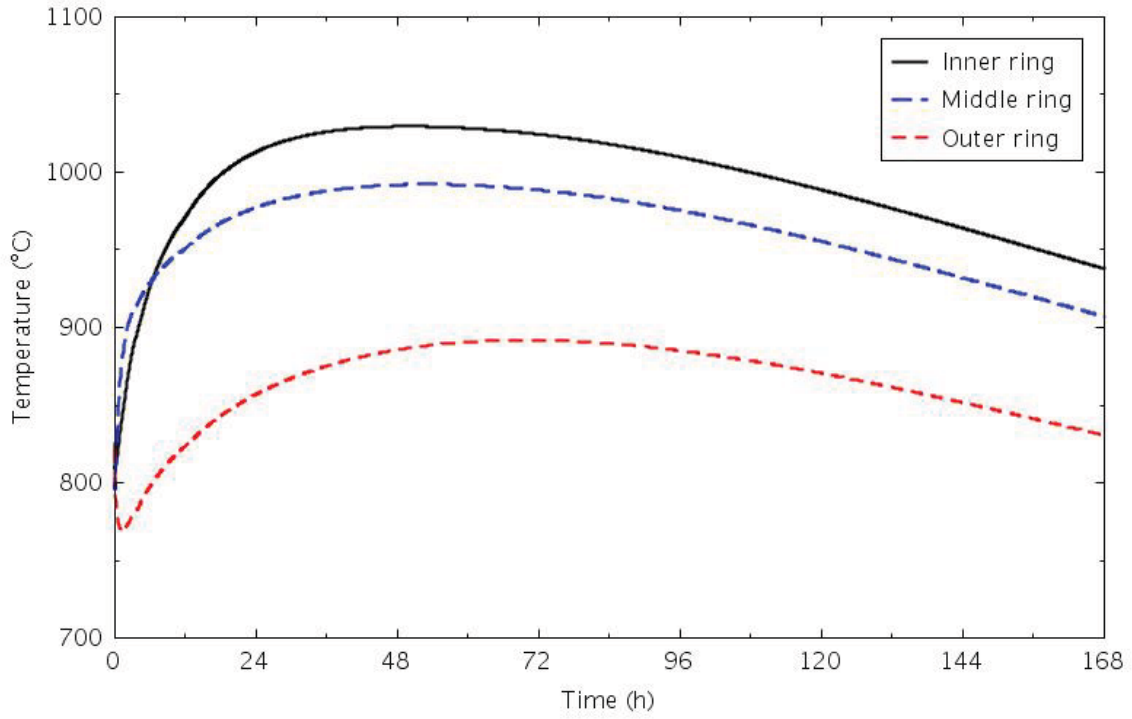


Figure 6-1. Calculated peak fuel temperatures for the MHTGR DCC transient.

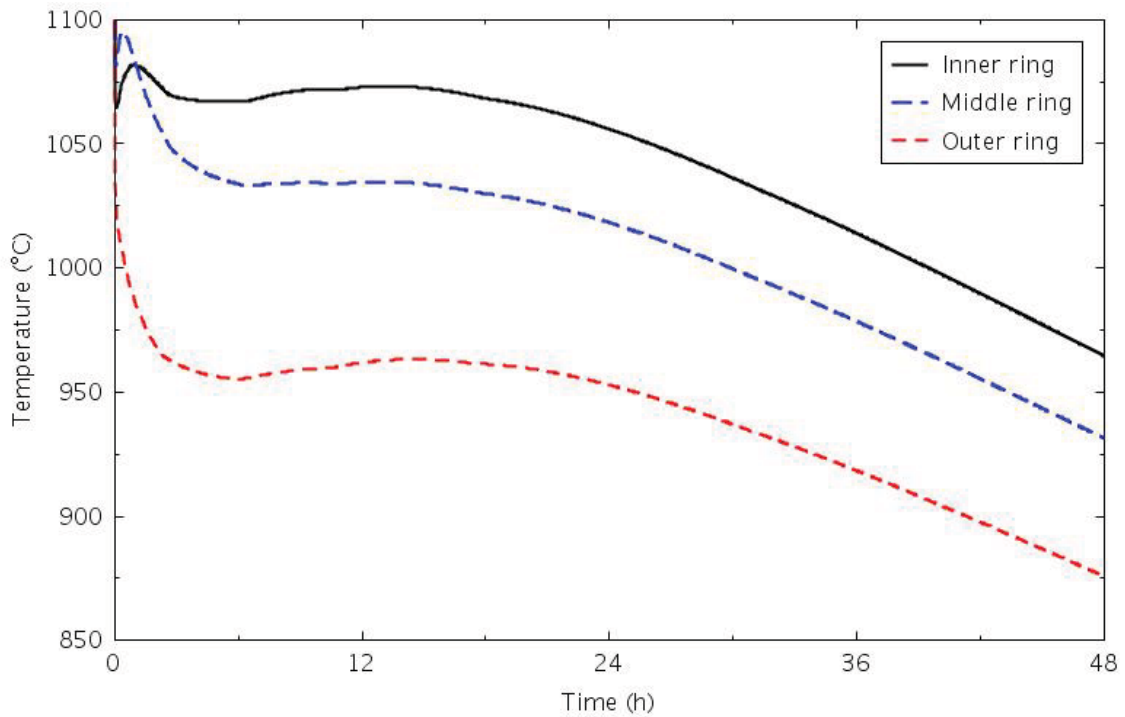


Figure 6-2. Calculated peak heater rod temperatures for the HTTF DCC transient.

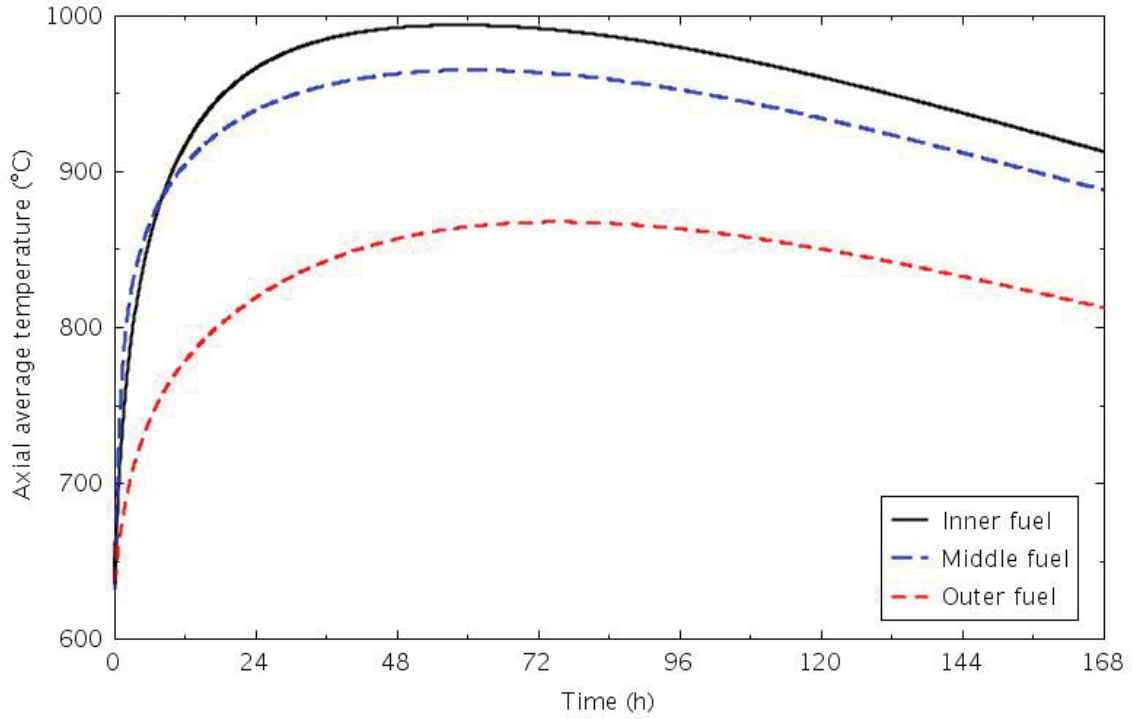


Figure 6-3. Calculated fuel axial average temperatures for the MHTGR DCC transient.

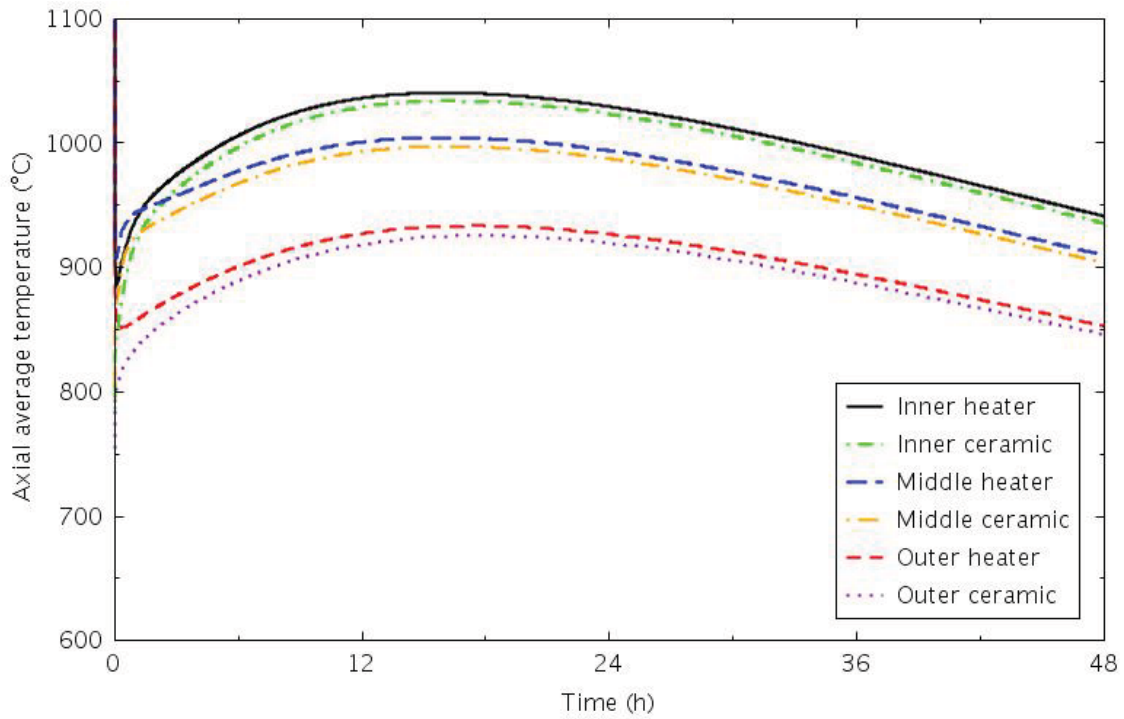


Figure 6-4. Calculated core region axial average temperatures for the HTTF DCC transient.

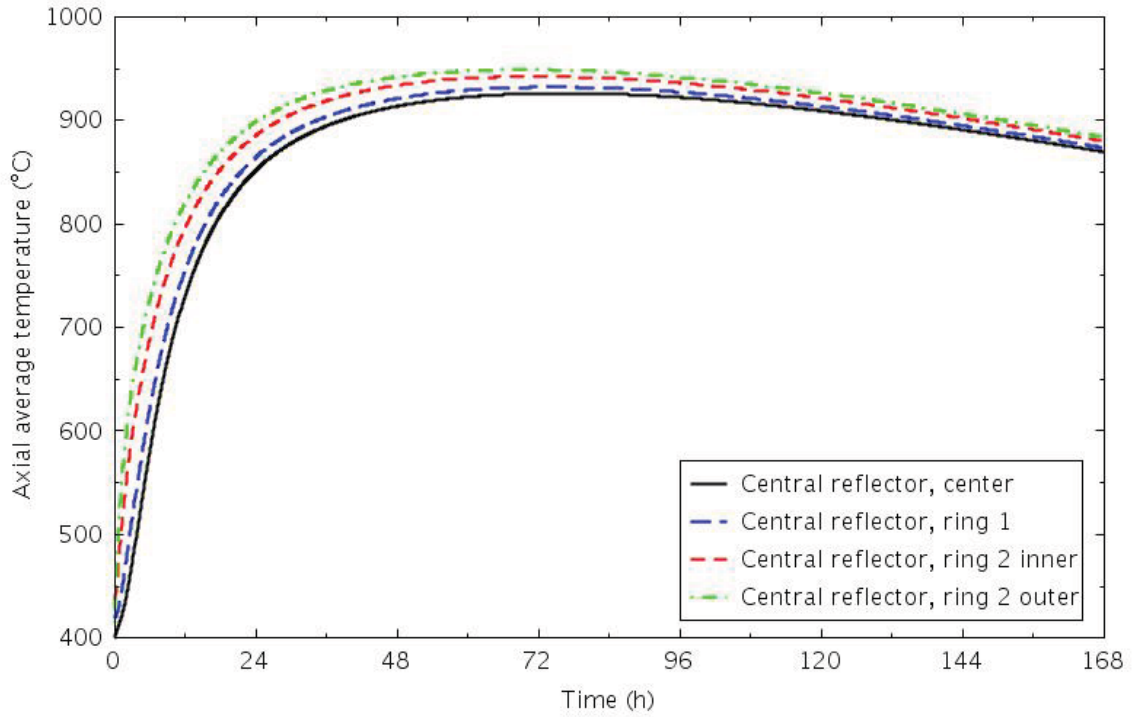


Figure 6-5. Calculated central reflector axial average temperatures for the MHTGR DCC transient.

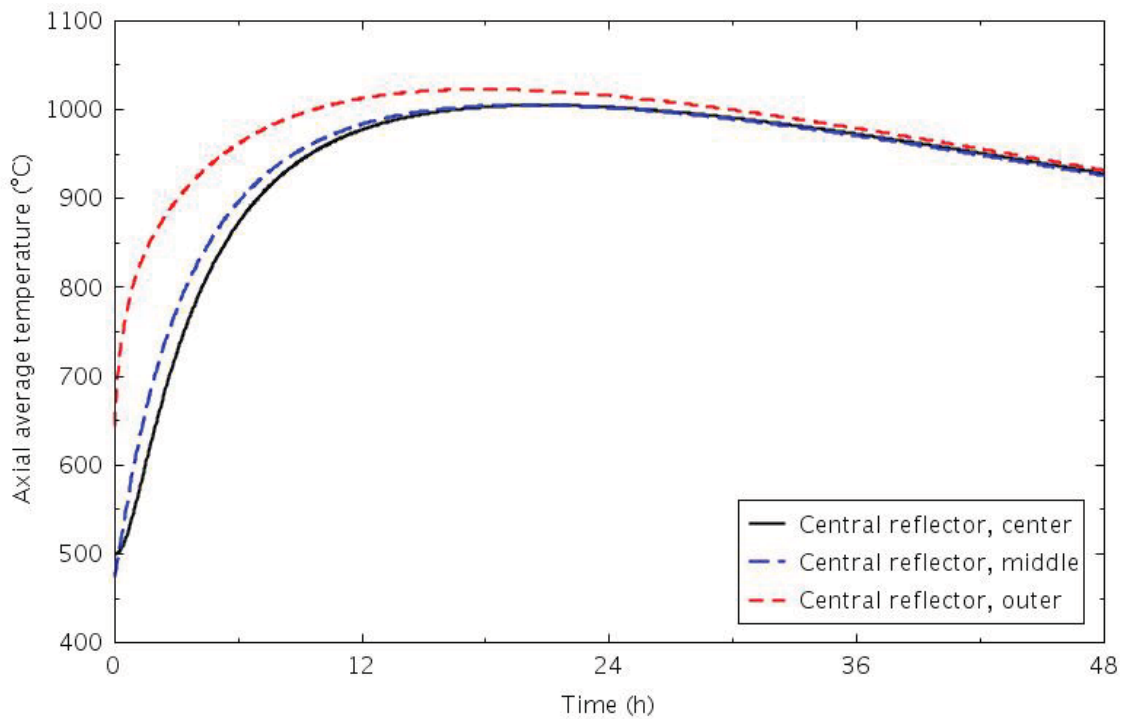


Figure 6-6. Calculated central reflector axial average temperatures for the HTTF DCC transient.

Average temperatures in the side reflector are shown in Figures 6-7 and 6-8. The peak inner ring temperatures are comparable in the two facilities, with the maximum value occurring near 90 hours in the MHTGR and near 21 hours in the HTTF. The radial gradient is larger in the HTTF, with the outer ring being 200 to 250°C cooler than the inner ring; the difference is about 100°C less in the MHTGR.

Figures 6-9 and 6-10 present the temperatures in the permanent side reflector, core barrel, and reactor vessel wall for the two facilities; in the MHTGR, two core barrel temperatures are shown, one for the portion connected to the coolant risers and one for the remaining portion. The reactor vessel temperatures are nearly the same in the two calculations. The permanent side reflector and core barrel temperatures in the MHTGR are about 100°C higher than the corresponding HTTF components, consistent with the temperature difference in the outer ring of the side reflector.

The heat removal through the reactor vessel is shown in Figures 6-11 and 6-12. The heat removal includes the convection heat transfer to the reactor cavity and the radiation heat transfer to the RCCS from both the reactor vessel shell and the upper head. For comparison, the total decay power is also provided in the figures. The heat removal exceeds the power input after 111 hours in the MHTGR and after 26 hours in the HTTF.

Coolant velocities at the top of selected core and reflector channels are presented in Figures 6-13 and 6-14; negative velocities indicate that flow is up through the channel. With both the inlet and outlet to the reactor at atmospheric pressure, all of the flow inside the core barrel is up through the core and down through the coolant risers to the vessel inlet side of the break. The velocities in the core channels are nearly the same in both facilities, as the coolant channel diameters are similar. The velocities in the HTTF reflector cooling channels are higher than those in the MHTGR because the cooling holes with diameters of 15.9 and 19.1 mm offer much less flow resistance than the 1-mm gaps between blocks.

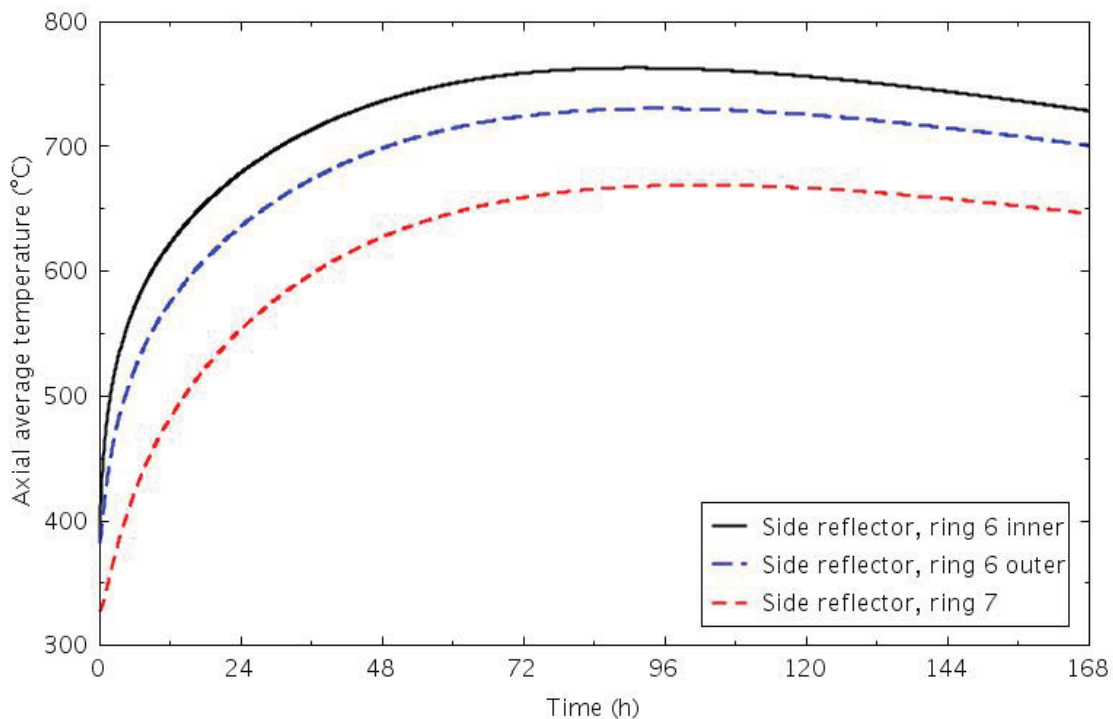


Figure 6-7. Calculated side reflector axial average temperatures for the MHTGR DCC transient.

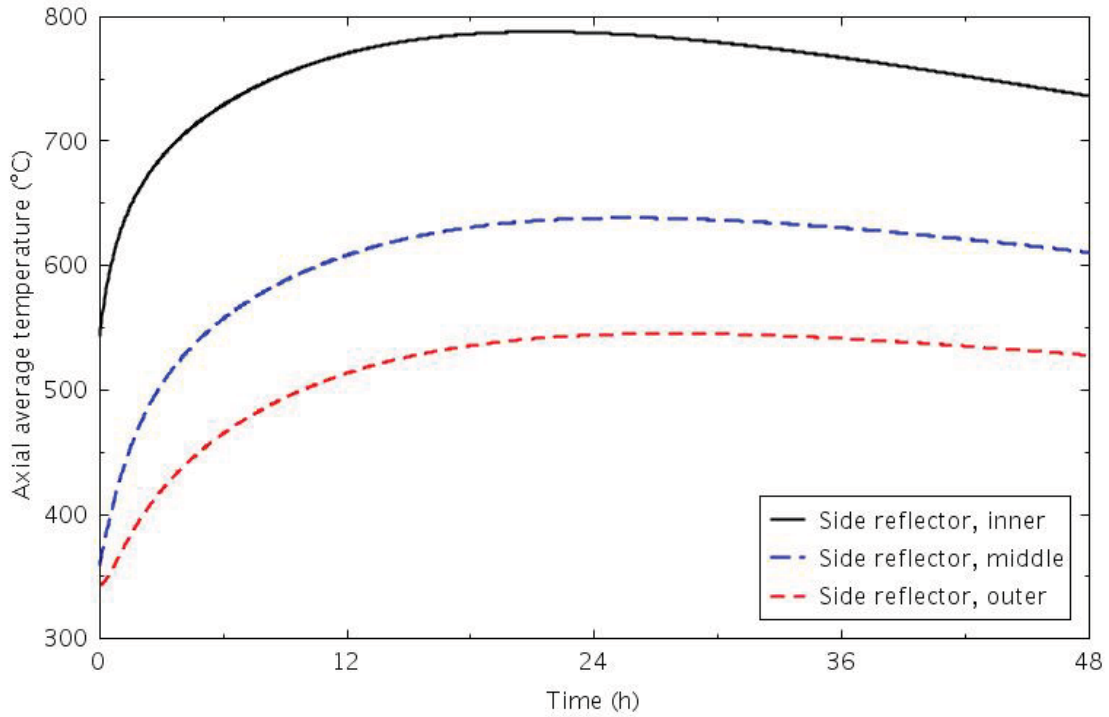


Figure 6-8. Calculated side reflector axial average temperatures for the HTTF DCC transient.

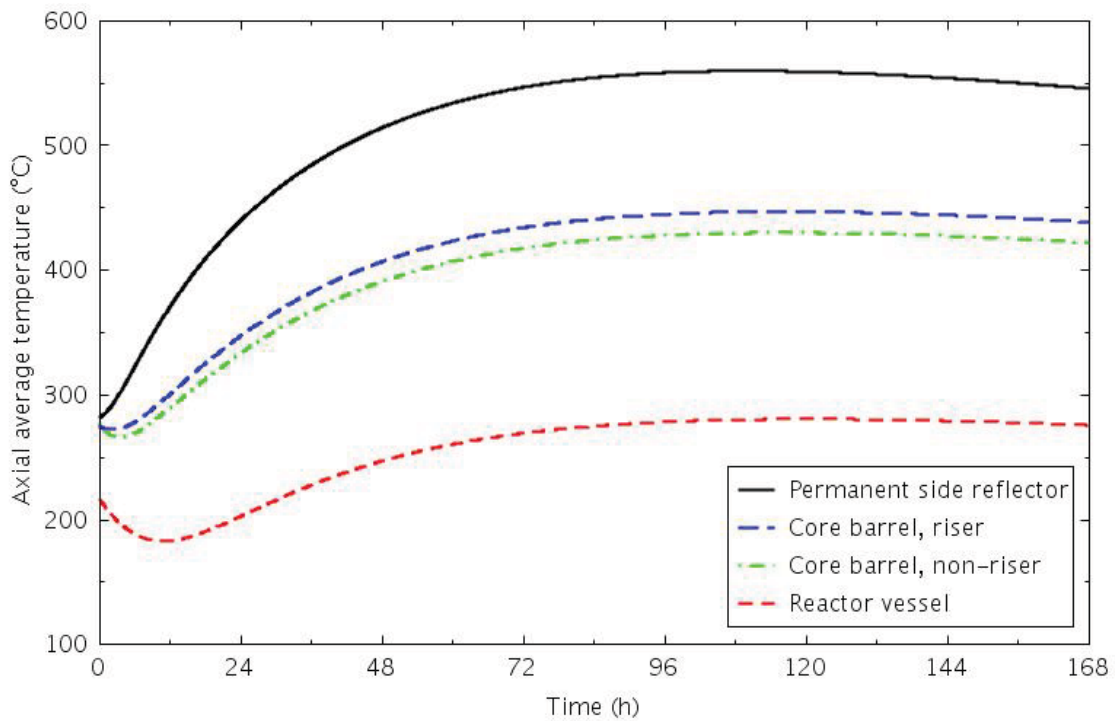


Figure 6-9. Calculated permanent side reflector, core barrel, and reactor vessel axial average temperatures for the MHTGR DCC transient.

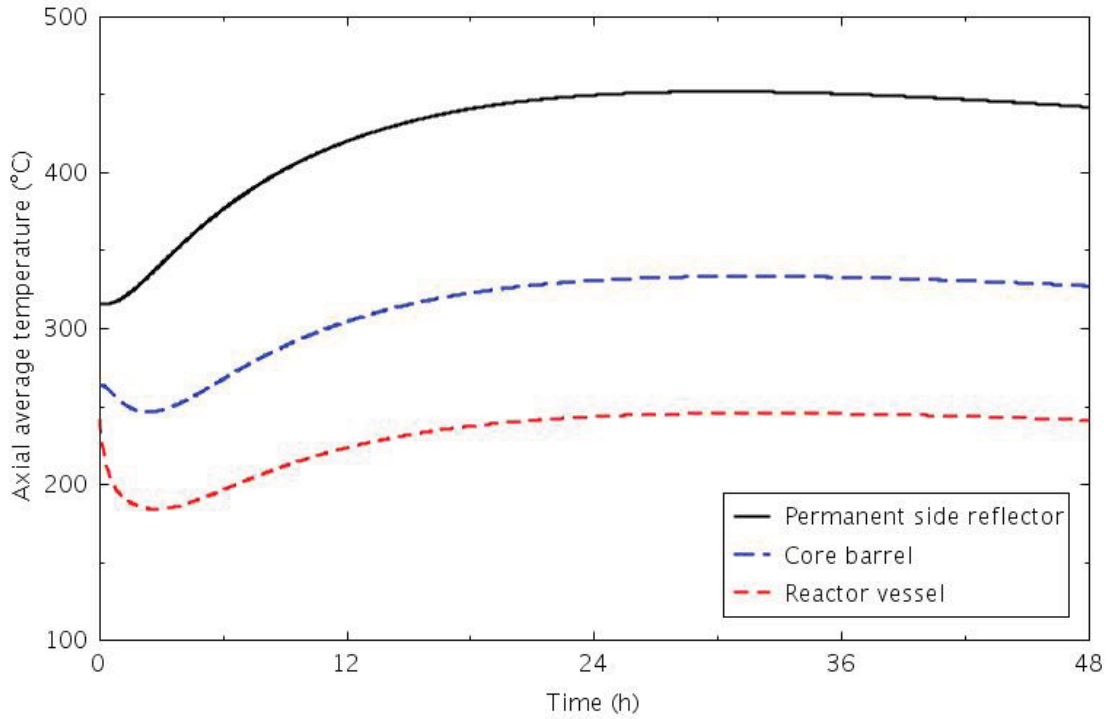


Figure 6-10. Calculated permanent side reflector, core barrel, and reactor vessel axial average temperatures for the HTTF DCC transient.

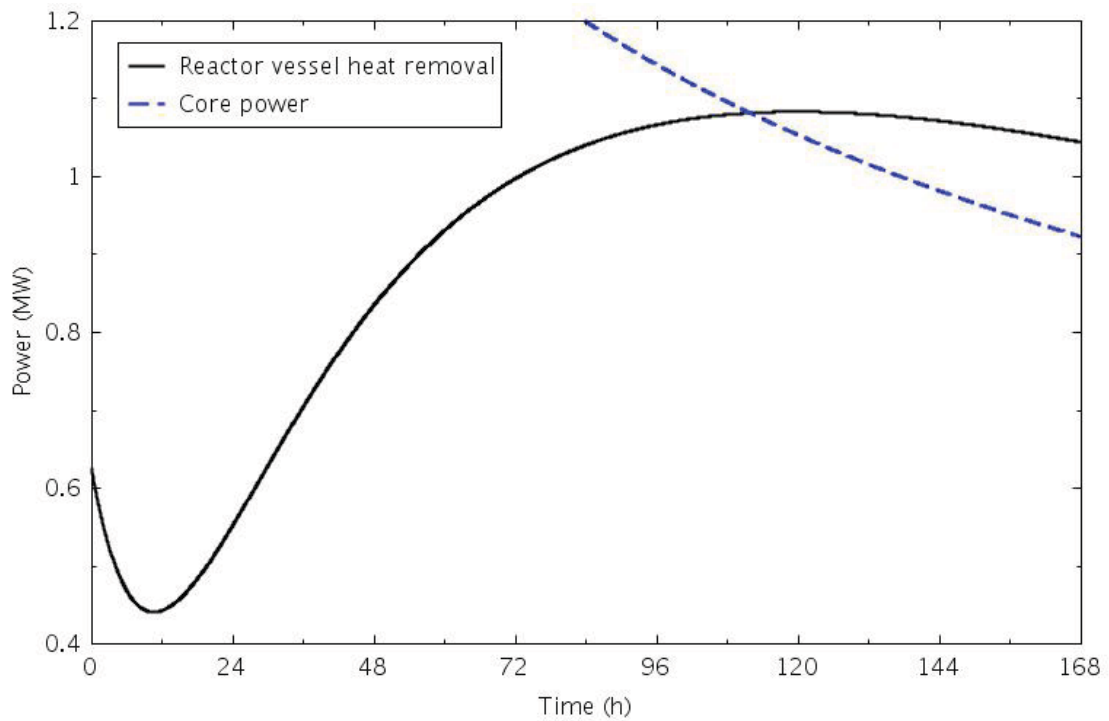


Figure 6-11. Calculated reactor vessel heat removal and core power for the MHTGR DCC transient.

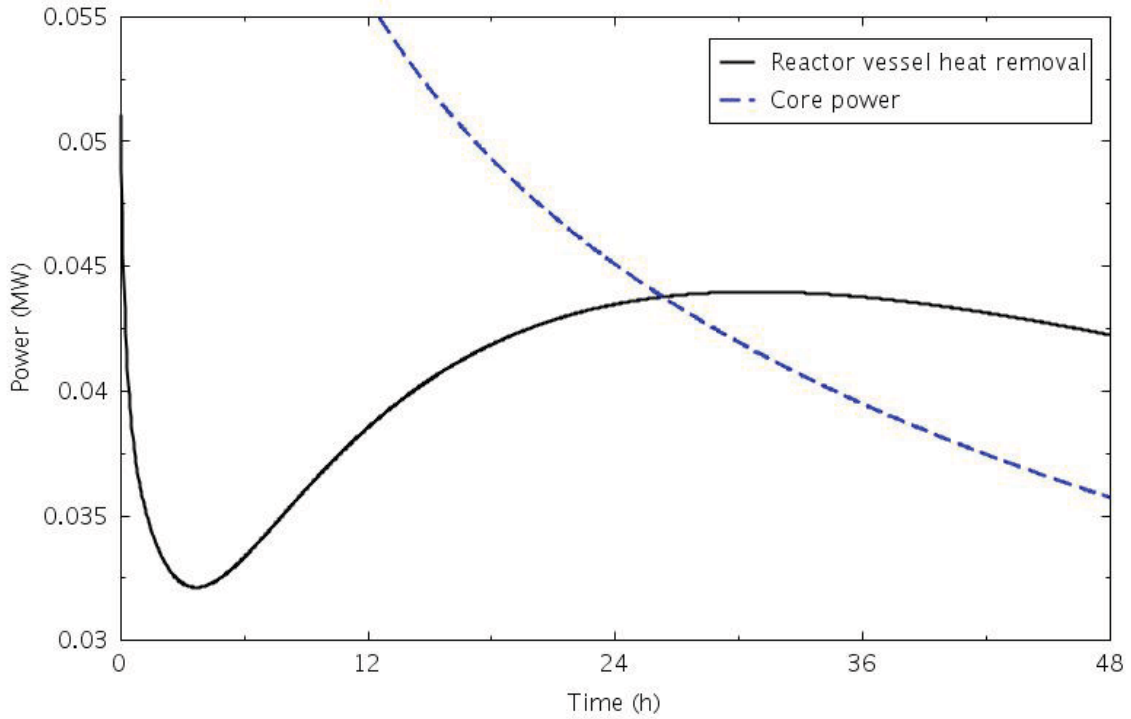


Figure 6-12. Calculated reactor vessel heat removal and core power for the HTTF DCC transient.

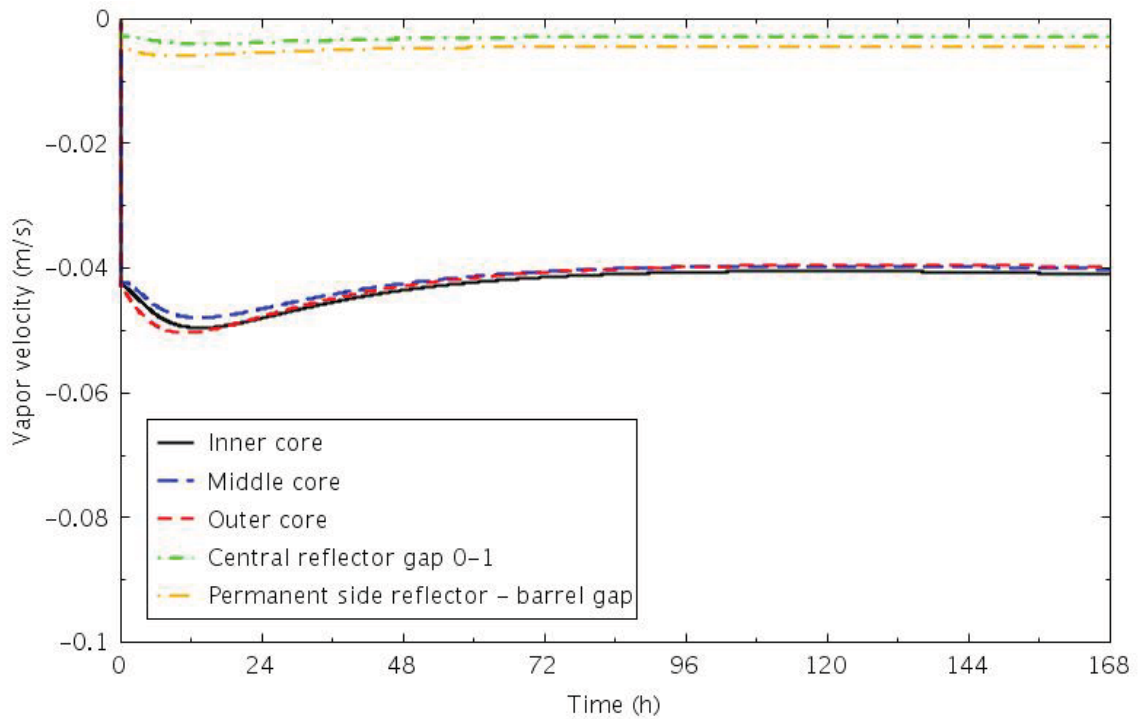


Figure 6-13. Calculated channel inlet coolant velocities for the MHTGR DCC transient.

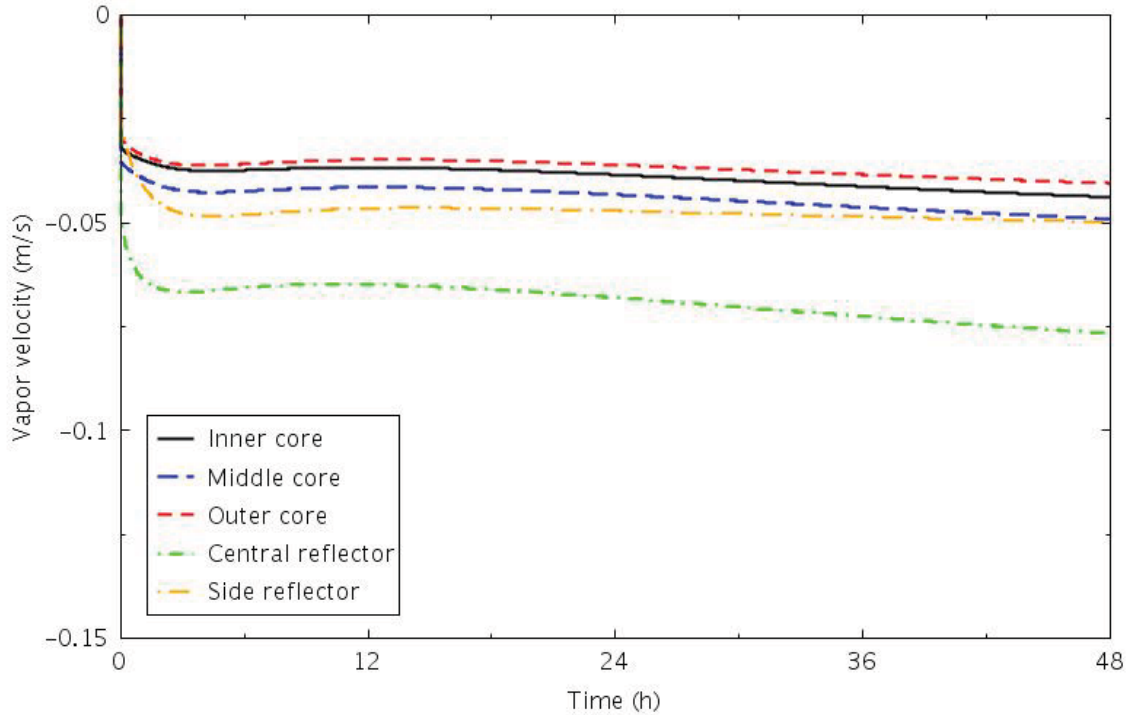


Figure 6-14. Calculated channel inlet coolant velocities for the HTTF DCC transient.

6.1.2 Sensitivity Calculations

Two sensitivity calculations were performed for both the MHTGR and the HTTF. The first addressed uncertainty in the decay power. The second investigated the effect of the reactor cavity gas composition.

In the first sensitivity calculations, the decay power was increased by 20%. Peak fuel temperatures from the MHTGR base and sensitivity calculations are compared in Figure 6-15. The peak temperatures were 100 to 150°C higher and occurred about 12 hours later with the higher decay power. Figure 6-16 shows the corresponding heater rod temperatures from the HTTF calculations. These peak temperatures also increased 100 to 150°C, with a delay of about 6 hours.

Peak reactor vessel temperatures are shown in Figures 6-17 and 6-18. For the MHTGR, the peak temperature occurred near 120 hours in both cases, but was 25°C higher with the increased decay heat. In the HTTF simulation, the peak temperature increased about 15°C, but was delayed about 5 hours. The peak vessel temperatures were about 75°C lower in the HTTF than in the MHTGR.

Figure 6-19 presents the calculated reactor vessel heat removal for the MHTGR, together with the decay power. The peak heat removal is 0.2 MW higher than in the base case (see Figure 6-11), and the time at which the heat removal exceeds the decay heat is about 2 hours later. The corresponding variables from the HTTF simulation are shown in Figure 6-20. Compared with Figure 6-12, the peak heat removal is about 6 kW higher in the sensitivity calculation, and the cross-over with the decay heat occurs about 5 hours later.

The second set of sensitivity calculations modeled the reactor cavity as containing pure air to provide an indication of the range of differences that might be seen in the calculated temperatures for different mixtures of helium and air. Graphite oxidation in the MHTGR was not modeled; only the effects of the different fluid properties on the heat transfer were considered.

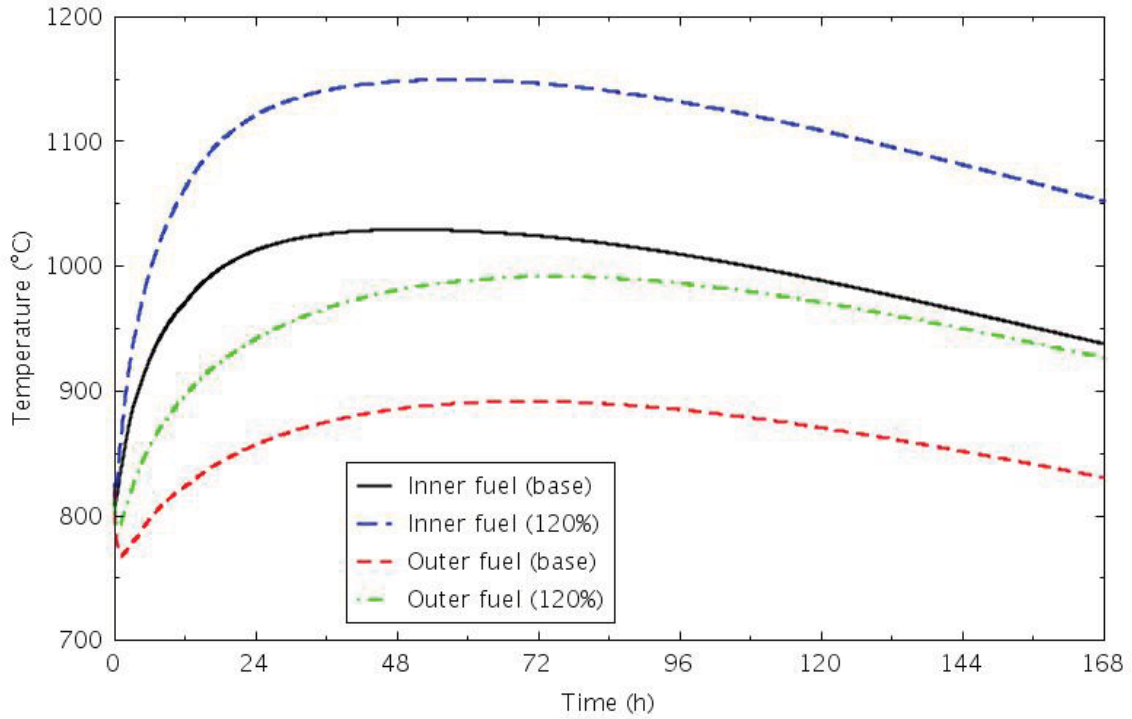


Figure 6-15. Peak fuel temperatures for the MHTGR DCC base and 120% decay power cases.

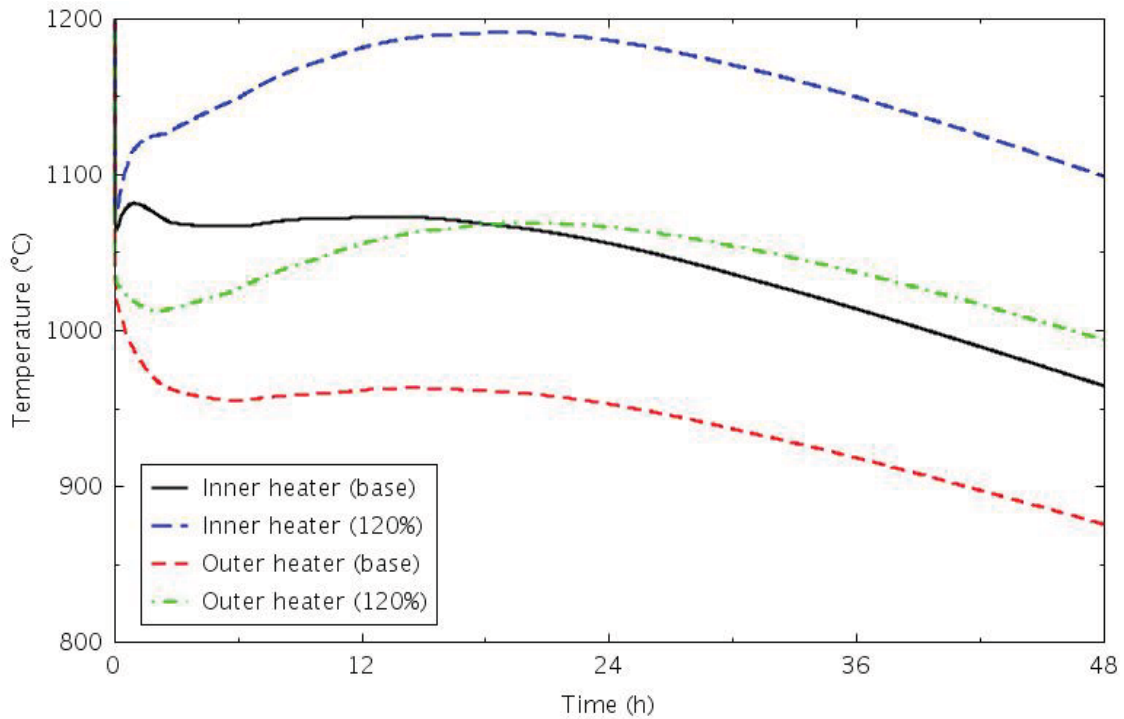


Figure 6-16. Peak heater rod temperatures for the HTTF DCC base and 120% decay power cases.

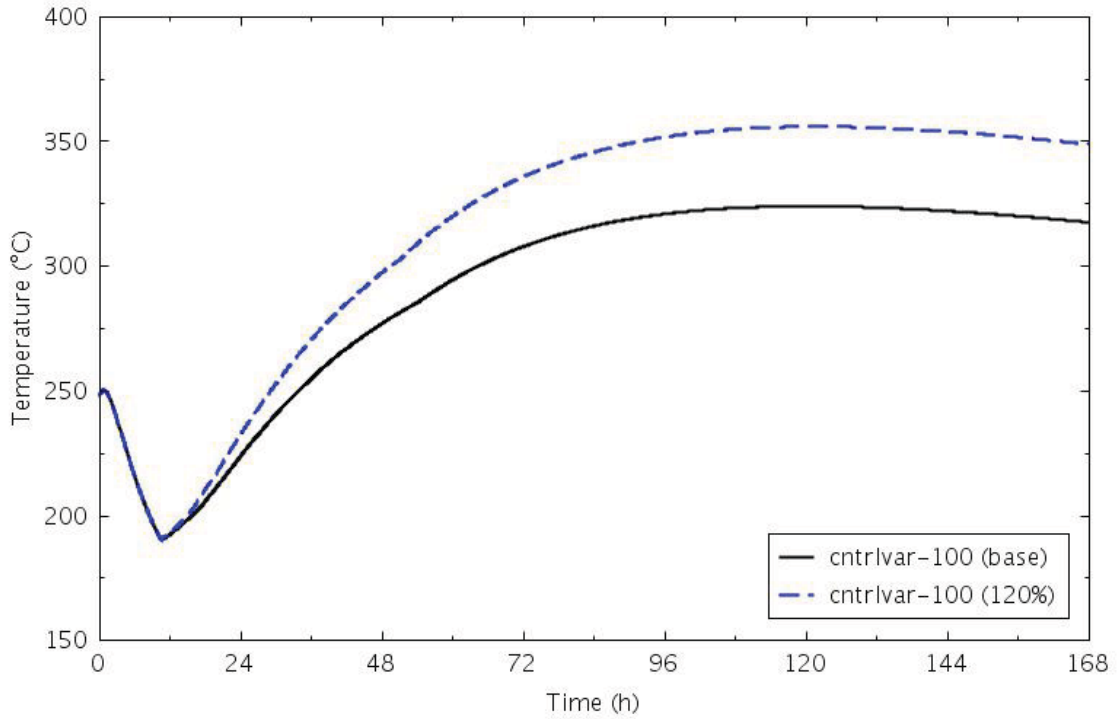


Figure 6-17. Peak reactor vessel temperatures for the MHTGR DCC base and 120% decay power cases.

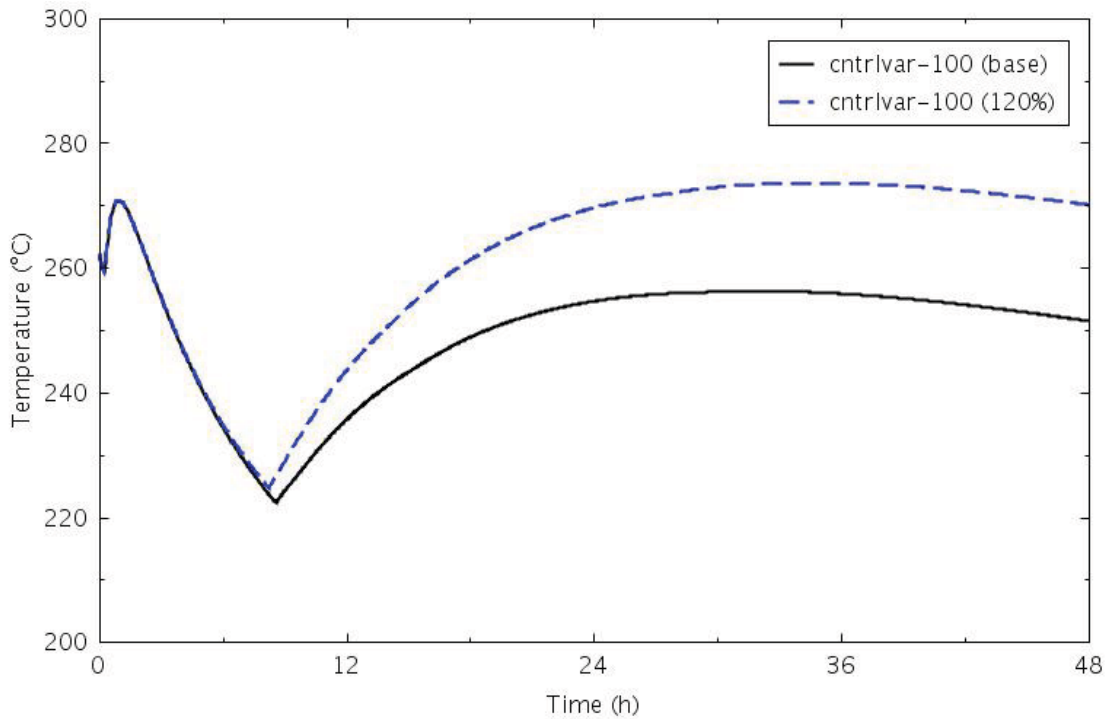


Figure 6-18. Peak reactor vessel temperatures for the HTTF DCC base and 120% decay power cases.

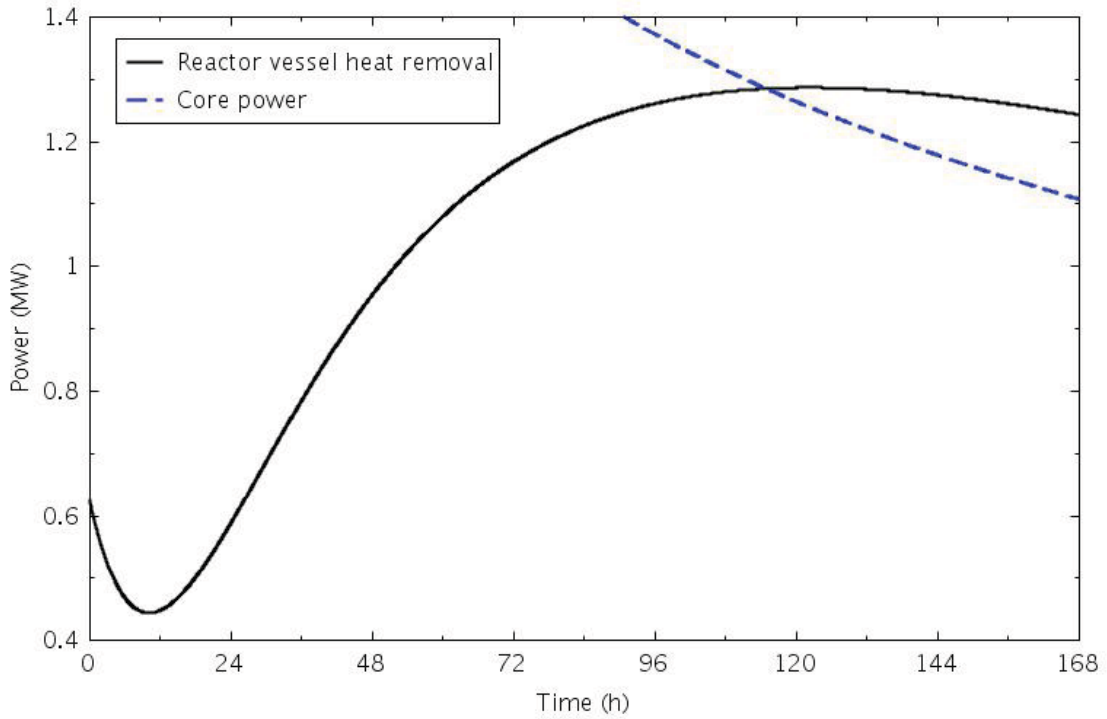


Figure 6-19. Calculated reactor vessel heat removal and core power for the MHTGR DCC 120% decay power case.

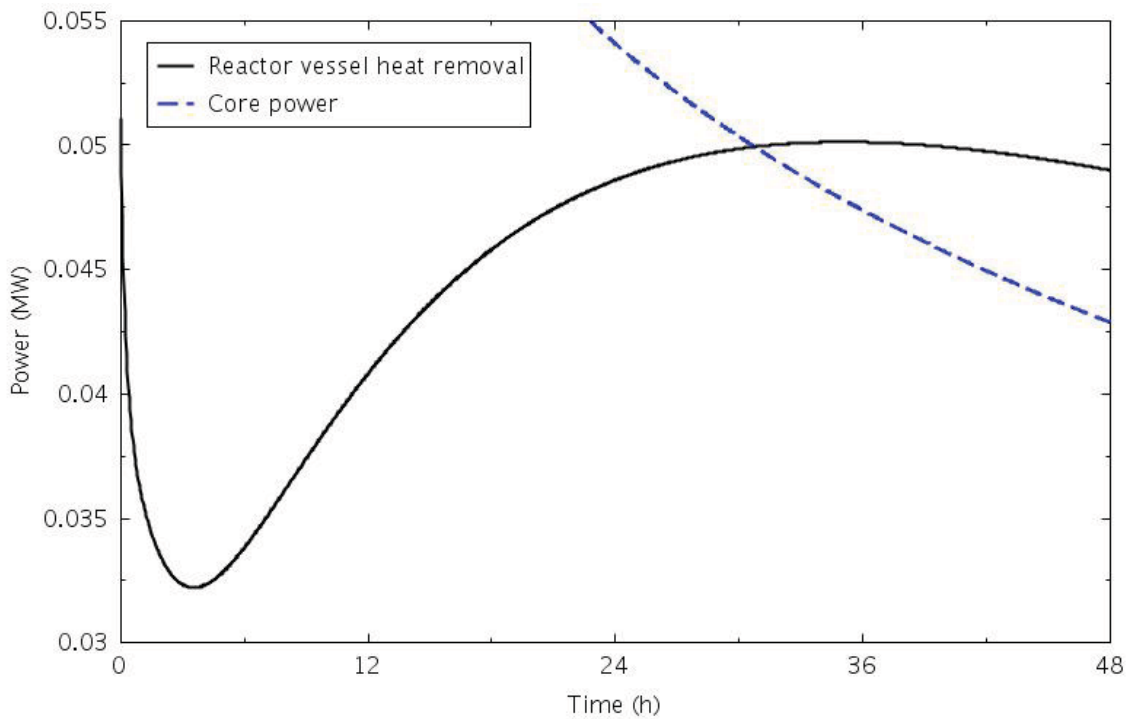


Figure 6-20. Calculated reactor vessel heat removal and core power for the HTTF DCC 120% decay power case.

Adding air had little effect on the calculated peak temperatures. Figure 6-21 shows that the MHTGR peak fuel temperatures increased less than 20°C, and Figure 6-22 shows that the peak heater rod temperatures in the HTTF transient only increased about 10°C. The peak reactor vessel temperatures, presented in Figures 6-23 and 6-24, were virtually unchanged from the base case calculation.

There were differences in the flow behavior. Selected channel inlet velocities for the MHTGR are presented in Figure 6-25. With helium, all of the channels had upward flow. With the introduction of air, only the central reflector gap is clearly flowing upward; the rest of the channels are nearly stagnant, and there is a very small downward flow in many of the channels, including all three core coolant channels. The core channel flow rates are on the order of 10^{-3} kg/s, with the gap flows several orders lower. This results in negligible convective heat transfer in the core. In the base case calculation, the convective heat transfer from the fuel blocks was three orders of magnitude lower than the conduction heat transfer; in this sensitivity calculation, it is nearly six orders of magnitude lower.

Similar flow effects are seen in the HTTF simulation, as shown in Figure 6-26. The velocities are very low, with flow going up in the side reflector and outer core ring coolant channels, and moving downward in the two inner core channels and central reflector. At these velocities, the mass flow rate in the core channels is on the order of 10^{-8} kg/s.

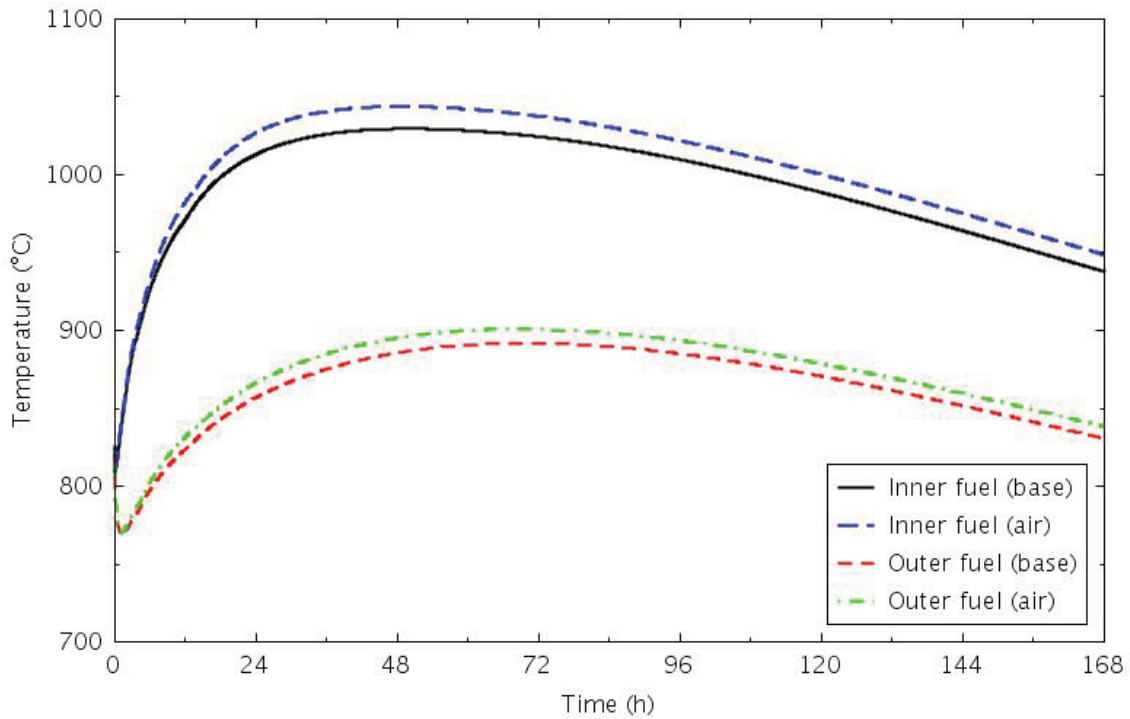


Figure 6-21. Peak fuel temperatures for the MHTGR DCC base and reactor cavity air cases.

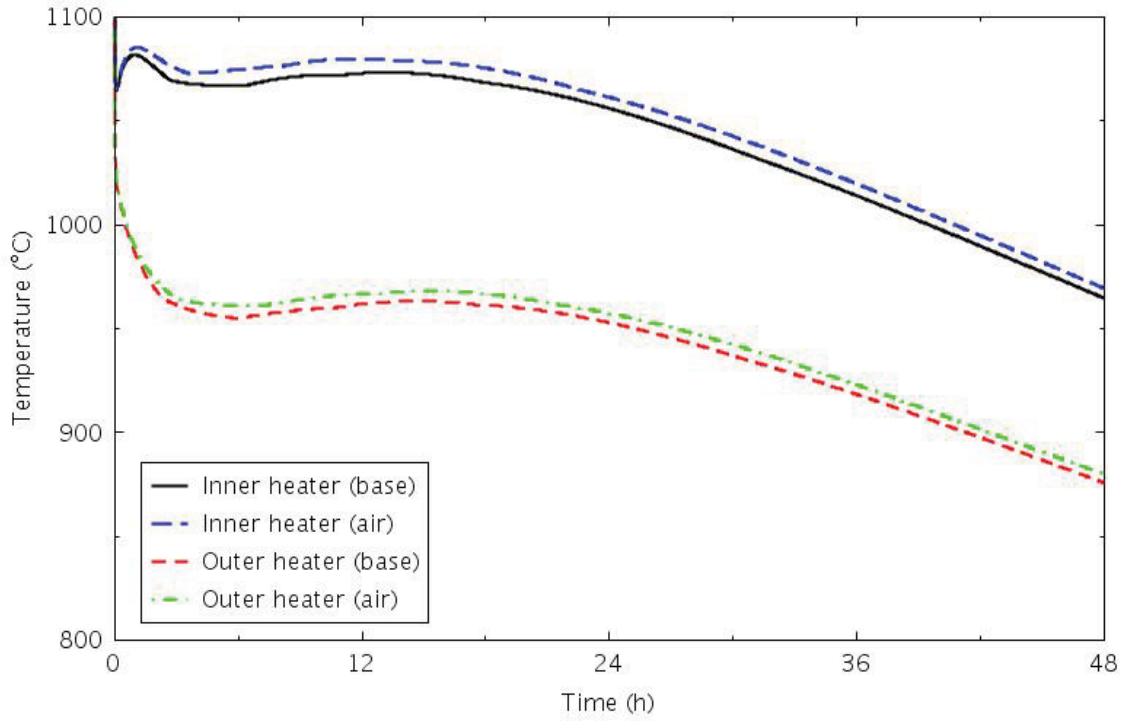


Figure 6-22. Peak heater rod temperatures for the HTTF DCC base and reactor cavity air cases.

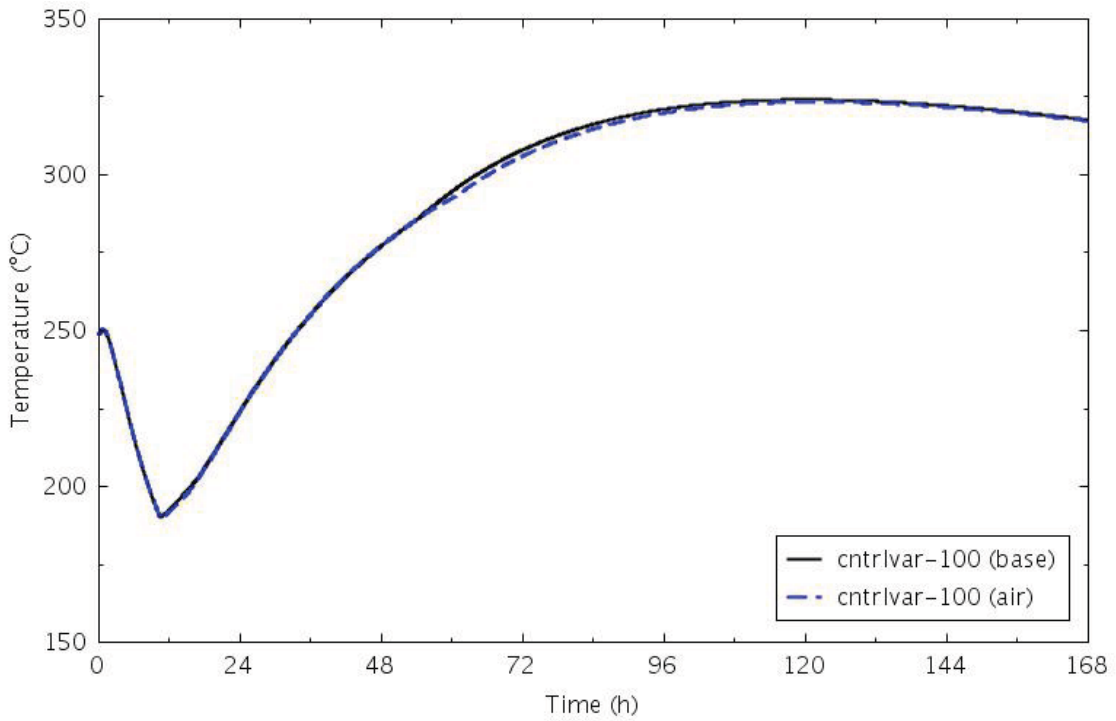


Figure 6-23. Peak reactor vessel temperatures for the MHTGR DCC base and reactor cavity air cases.

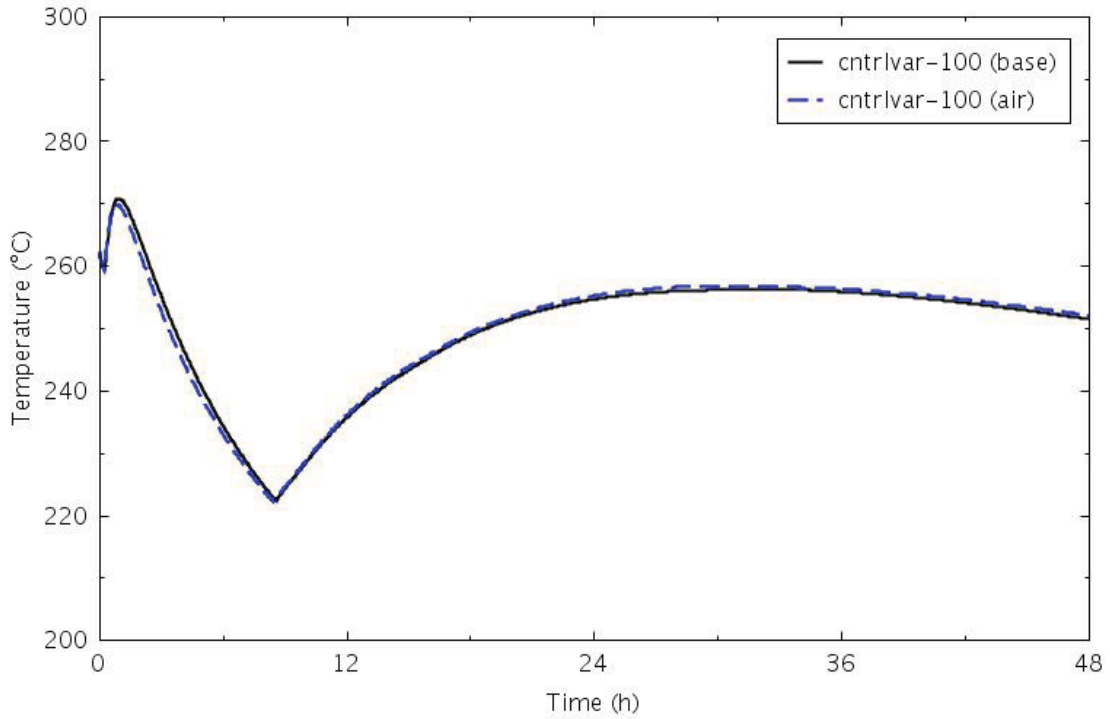


Figure 6-24. Peak reactor vessel temperatures for the HTTF DCC base and reactor cavity air cases.

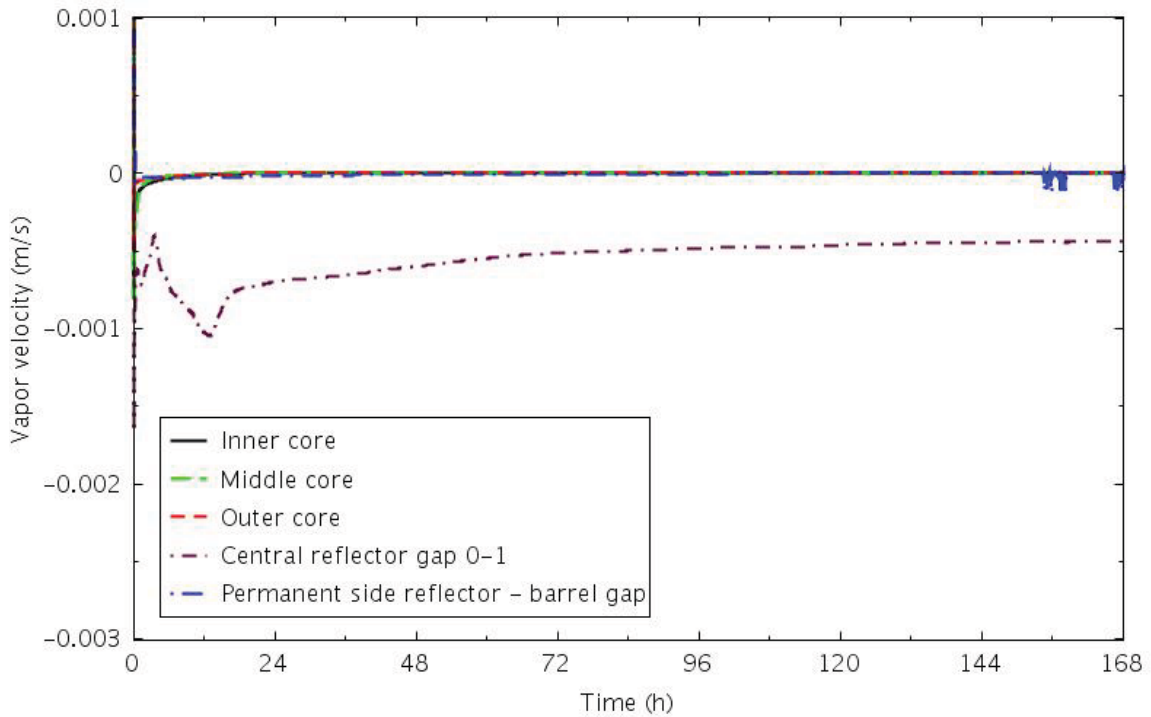


Figure 6-25. Coolant channel inlet velocities for the MHTGR DCC base and reactor cavity air cases.

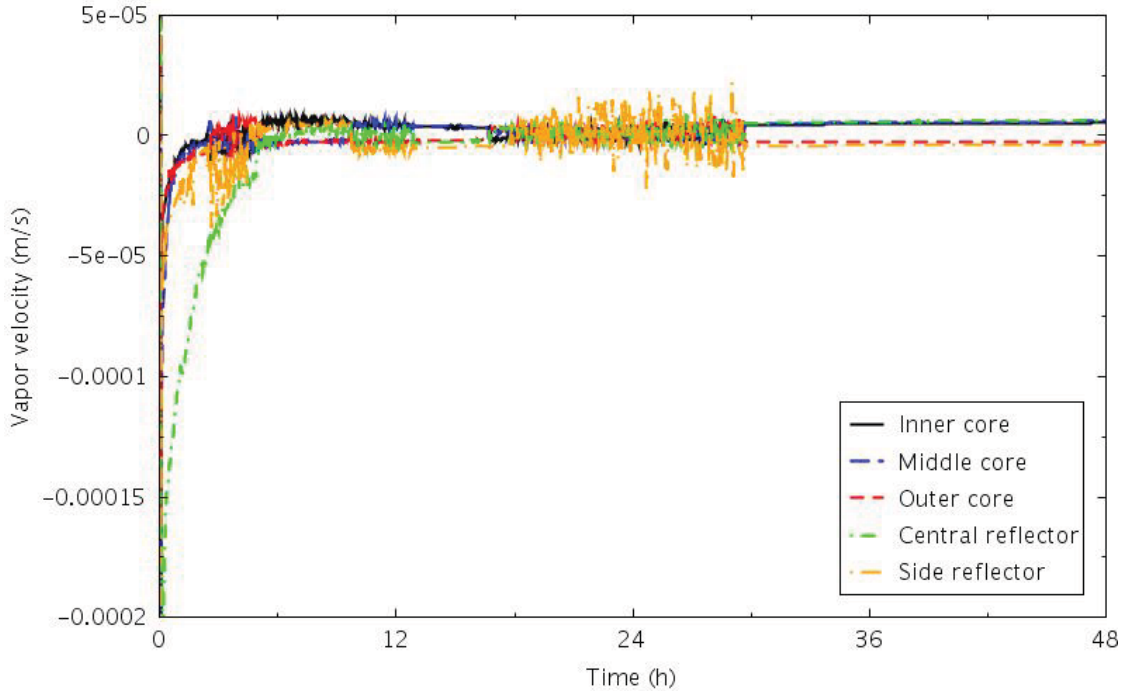


Figure 6-26. Coolant channel inlet velocities for the HTTF DCC base and reactor cavity air cases.

6.2 Pressurized Conduction Cooldown

Simulations of PCC transients were also performed. The PCC was modeled by imposing a 60-second linear flow coastdown from the initial value to zero. The pressure at the reactor vessel outlet was held constant at the steady-state value, and the inlet line was isolated. This configuration results in a recirculating natural convection pattern, with flow entering the outlet plenum from the break, being heated as it flows up through some of the coolant channels to the inlet plenum, then flowing down through other coolant channels to the outlet plenum. A reactor scram signal was assumed to be generated at transient initiation. The calculations were terminated after all of the structure temperatures had reached their peaks and begun to cool down—at 168 hours for the MHTGR and 48 hours for the HTTF. Base case and sensitivity calculations were performed.

6.2.1 Base Case Calculations

Figure 6-27 presents the MHTGR peak fuel temperatures. During the first minute, the temperatures decreased because the power was decreasing more rapidly than the flow. This allowed some of the stored energy in the core to be removed, resulting in 100 to 150°C lower peak temperatures than were calculated for the DCC transient. The maximum temperatures were reached at 45, 46, and 53 hours in the inner, middle, and outer rings respectively. The two inner ring times are comparable to those for the DCC, but the outer ring is about 24 hours earlier.

Figure 6-28 presents the HTTF peak heater rod temperatures. The initial response is different from the MHTGR because the flow coastdown does not remove much of the stored energy in the core. The principal reason for this is the low flow Reynolds numbers during steady-state. While the initial flow rate through the core is turbulent, it quickly transitions to laminar as the flow rate is decreased. This reduces the convective heat transfer to the coolant, keeping the structures hotter. The overall effect is that the PCC temperatures are only slightly (less than 20°C) cooler than the DCC temperatures. The peak temperatures before the final cooldown also occur at the same time—between 13 and 15 hours.

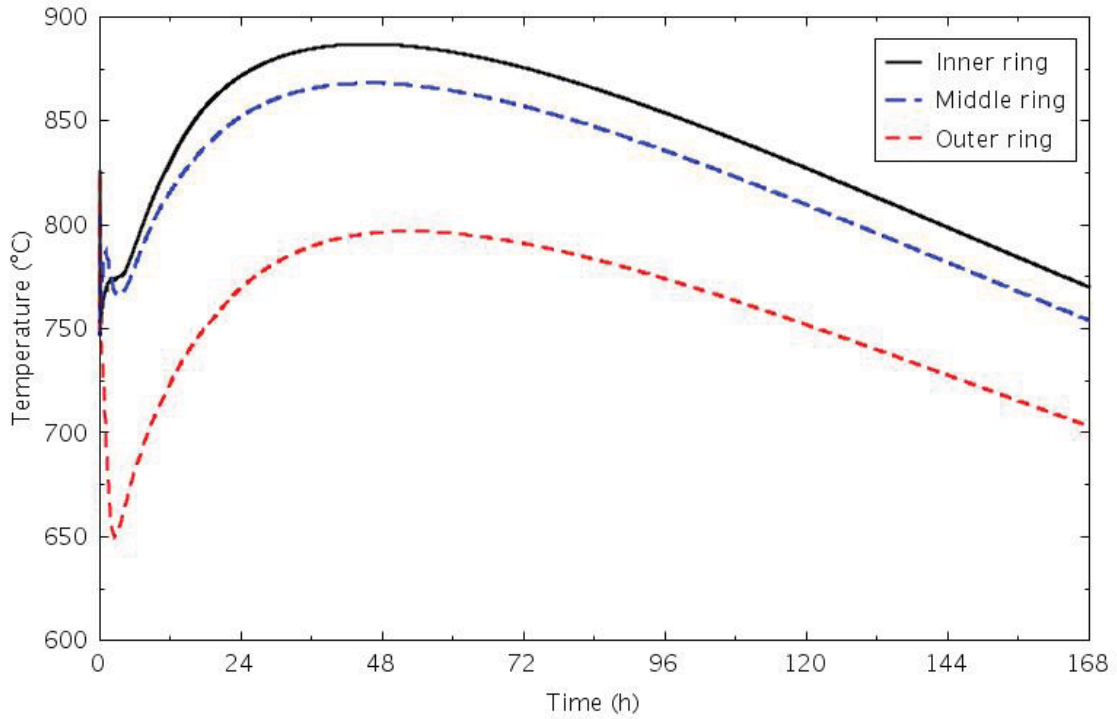


Figure 6-27. Calculated peak fuel temperatures for the MHTGR PCC transient.

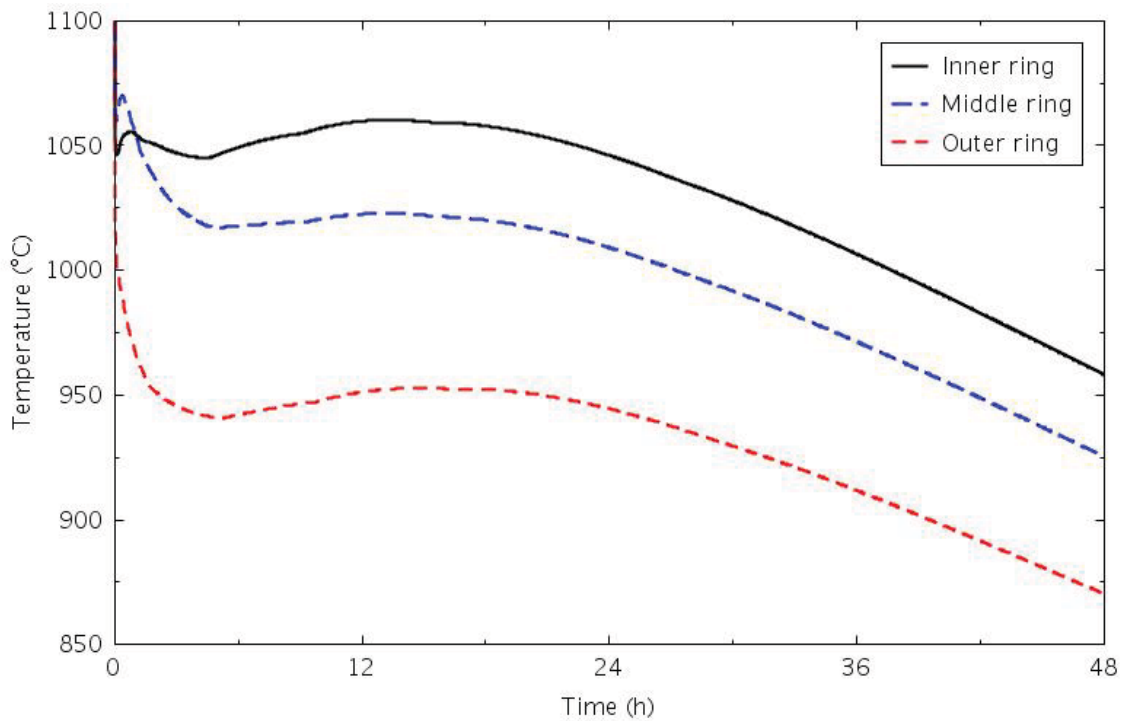


Figure 6-28. Calculated peak heater rod temperatures for the HTTF PCC transient.

The core axial average temperature response is shown in Figures 6-29 and 6-30. In the MHTGR, the peak temperatures in all three rings occur around 60 hours, and are 100 to 200°C lower than in the DCC transient. The HTTF temperature response is essentially the same as in the DCC transient, with the maximum temperatures occurring around 16 hours.

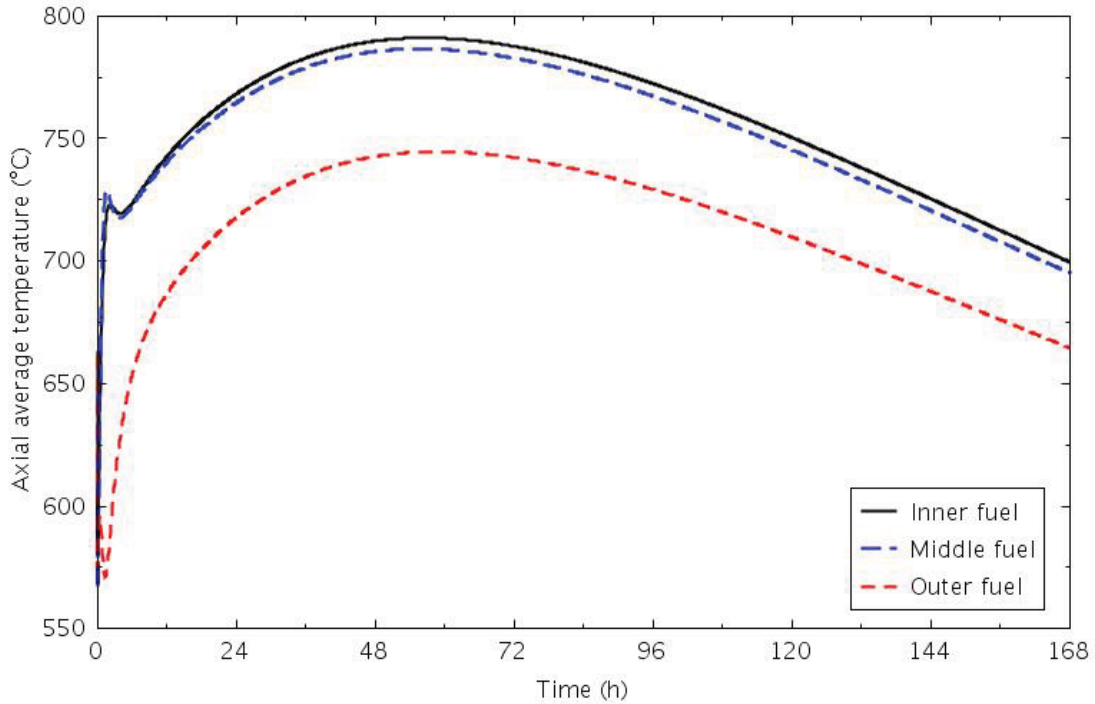


Figure 6-29. Calculated fuel axial average temperatures for the MHTGR PCC transient.

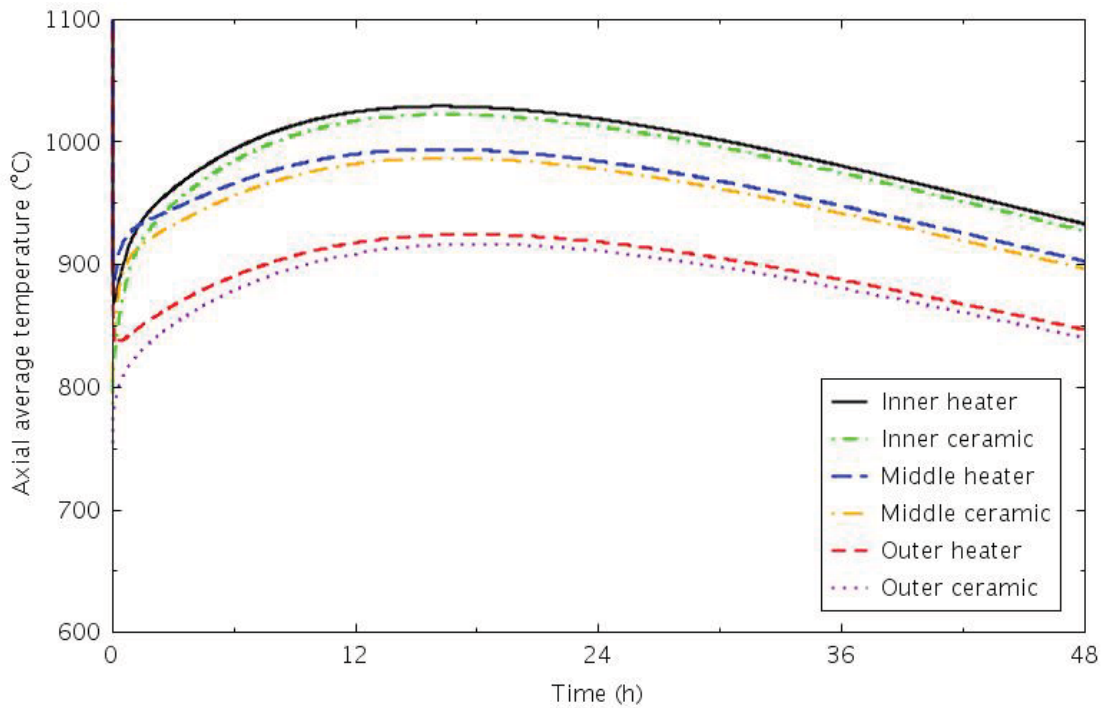


Figure 6-30. Calculated core region axial average temperatures for the HTTF PCC transient.

Central reflector average temperatures are presented in Figures 6-31 and 6-32 for the MHTGR and the HTTF, respectively. In both facilities, the reflector ring nearest the core stays the hottest throughout the transient. In the MHTGR, the peak temperatures occur between 60 and 66 hours, about 150°C cooler and 10 hours earlier than in the DCC, peaking first nearest the core then working toward the center of the reflector. In the HTTF, the outer ring temperature peaks near 18 hours, with the other two rings peaking 3 hours later.

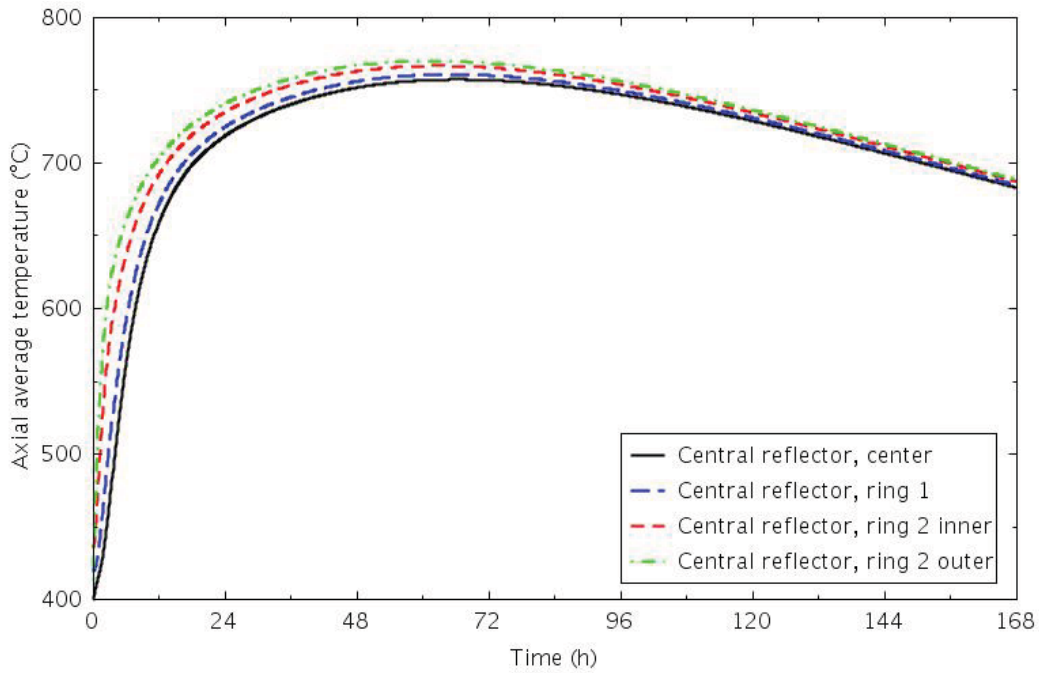


Figure 6-31. Calculated central reflector axial average temperatures for the MHTGR PCC transient.

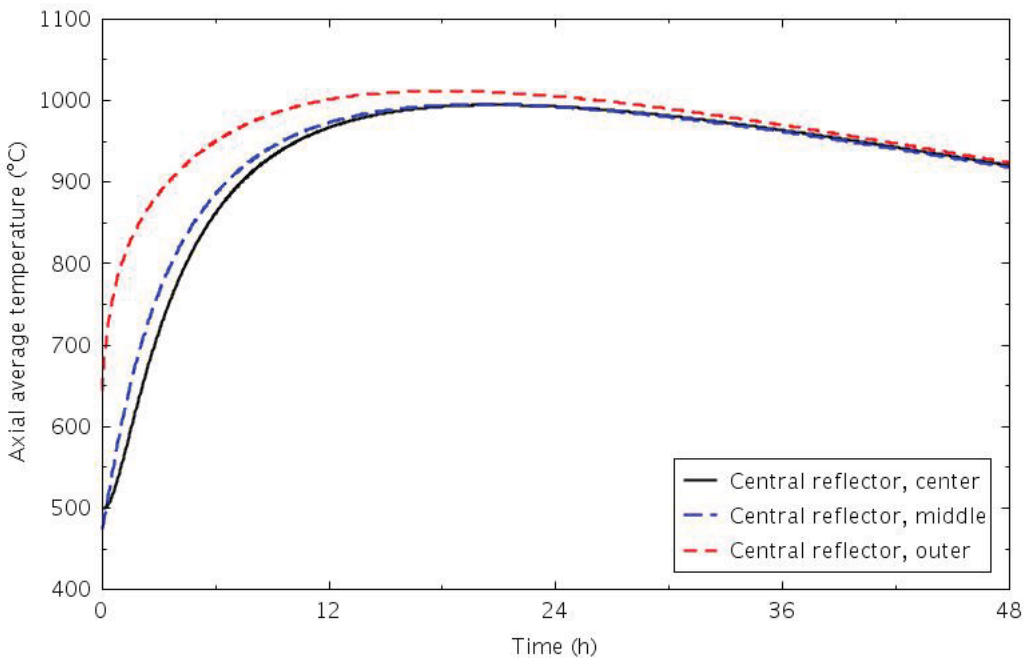


Figure 6-32. Calculated central reflector axial average temperatures for the HTTF PCC transient.

Average temperatures in the side reflector are shown in Figures 6-33 and 6-34. The peak inner ring temperature is about 100°C lower in the MHTGR, while the peak outer ring temperature is about 50°C higher, yielding a radial temperature gradient 150°C higher in the HTTF than in the MHTGR.

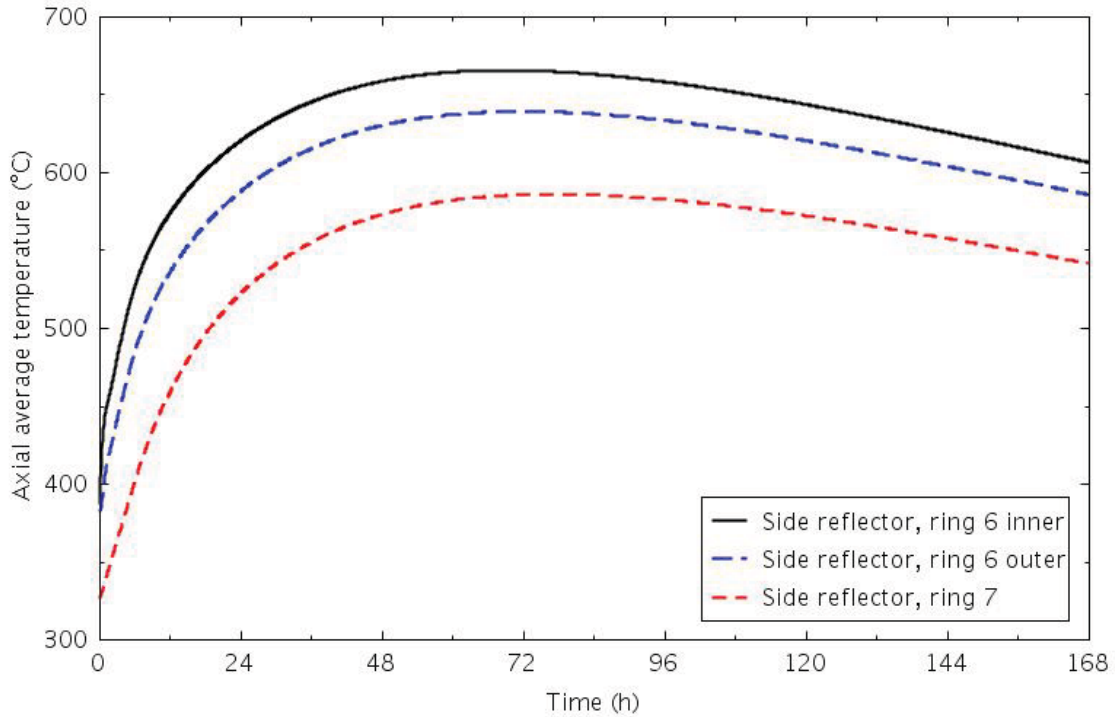


Figure 6-33. Calculated side reflector axial average temperatures for the MHTGR PCC transient.

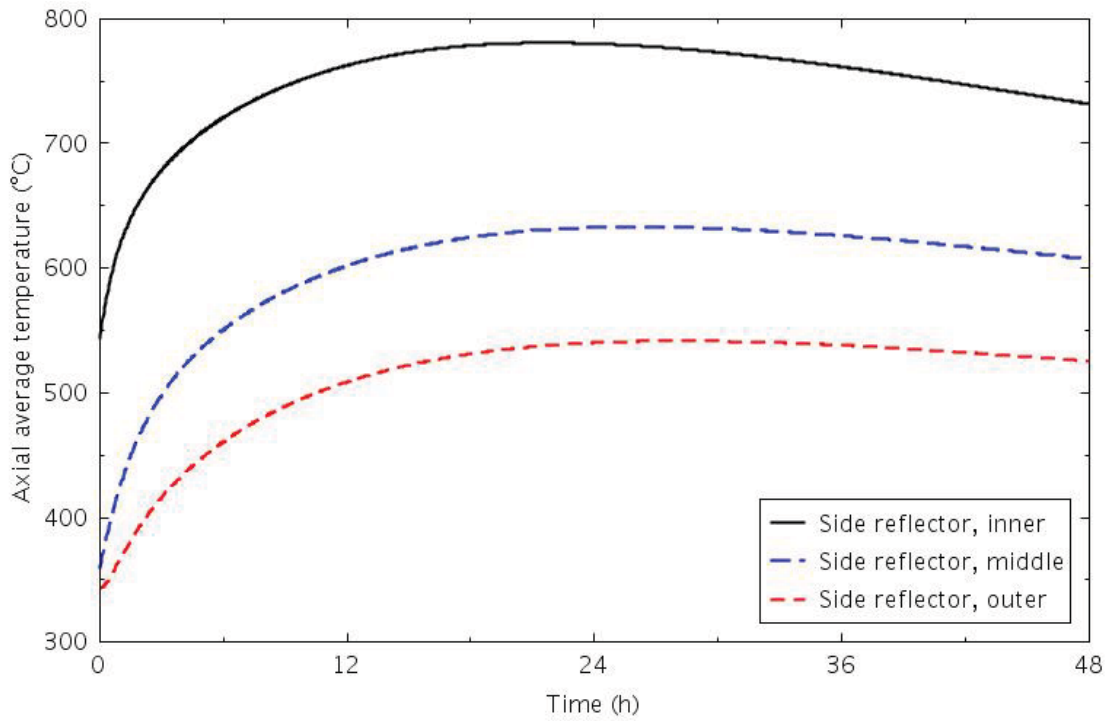


Figure 6-34. Calculated side reflector axial average temperatures for the HTTF PCC transient.

Figures 6-35 and 6-36 present the temperatures in the permanent side reflector, core barrel, and reactor vessel wall for the two facilities. Two core barrel temperatures are shown in the MHTGR, one for the portion connected to the coolant risers and one for the remaining portion. All three temperatures are higher in the MHTGR: the permanent side reflector by 50°C, the core barrel by 75°C, and the reactor vessel by 50°C.

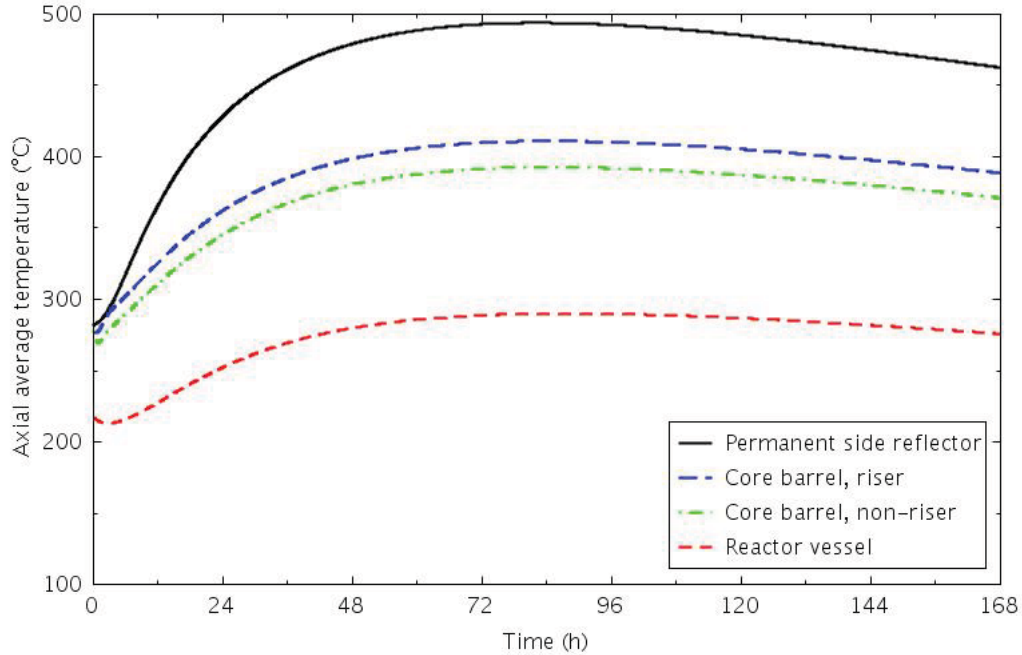


Figure 6-35. Calculated permanent side reflector, core barrel, and reactor vessel axial average temperatures for the MHTGR PCC transient.

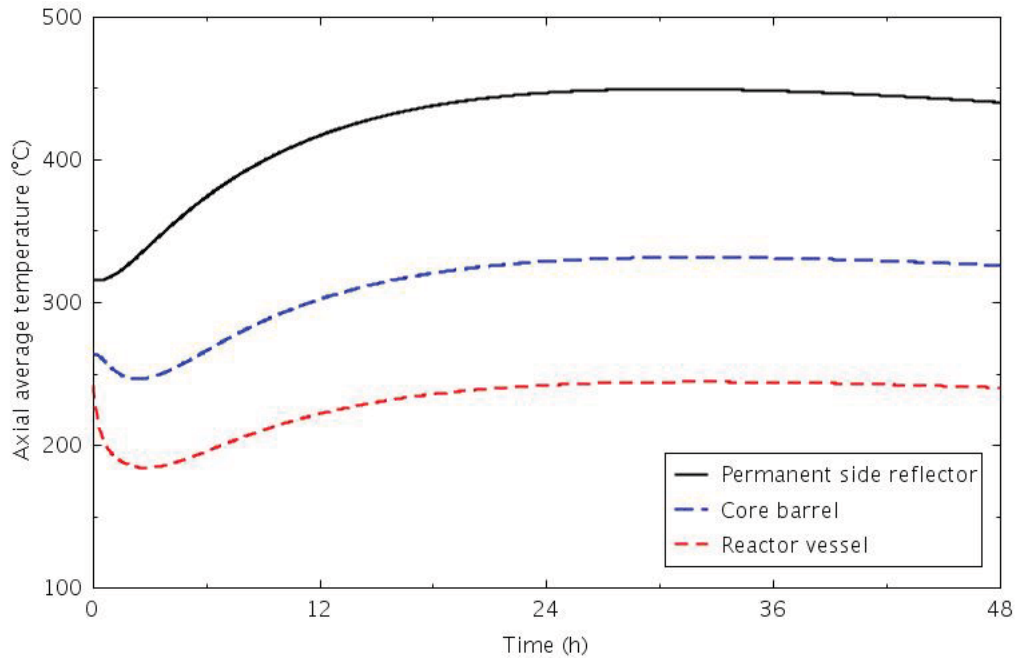


Figure 6-36. Calculated permanent side reflector, core barrel, and reactor vessel axial average temperatures for the HTTF PCC transient.

The heat removal through the reactor vessel is shown in Figures 6-37 and 6-38. The heat removal includes the convection heat transfer to the reactor cavity and the radiation heat transfer to the RCCS from both the reactor vessel shell and the upper head. For comparison, the total decay power is also provided in the figures. The heat removal exceeds the power input after 96 hours in the MHTGR and after 26 hours in the HTTF.

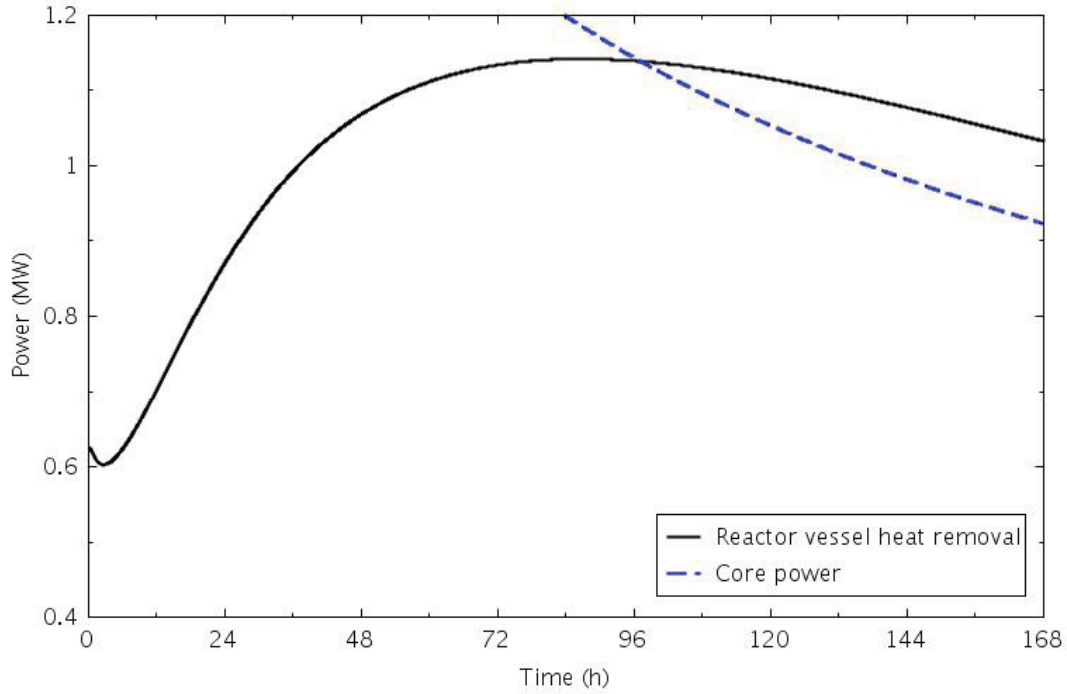


Figure 6-37. Calculated reactor vessel heat removal and core power for the MHTGR PCC transient.

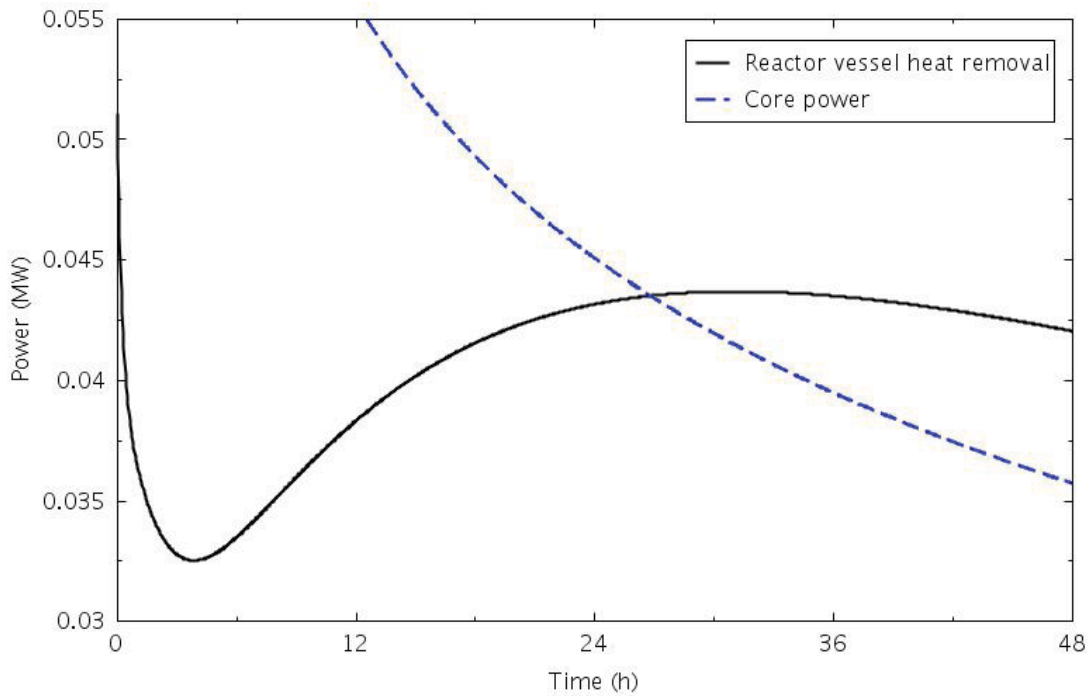


Figure 6-38. Calculated reactor vessel heat removal and core power for the HTTF PCC transient.

Coolant velocities at the top of selected core and reflector channels are presented in Figures 6-39 and 6-40; negative velocities indicate that flow is up through the channel. When natural circulation flow is initially established in the MHTGR, flow is up through the inner and middle fuel rings and down through both reflectors and the outer core ring. As the transient progresses, the flow through the coolant gap around the central reflector center block decreases, eventually reversing to a small upward flow. In the larger diameter channels (core and control rod channels, reflector/core barrel gap), the convection and radiation/conduction heat transfer rates are of the same order; in the small gaps between blocks, the convection is an order of magnitude lower than the radiation or conduction. In the HTTF, the initial natural convection flow pattern is up through the three core channels and down through the reflector cooling channels. As the transient progresses, the flow in the central reflector and outer core channels eventually reverse, with flow up in the inner and middle core rings and central reflector, and down through the outer core ring and side reflector. The convection heat transfer rate is two orders of magnitude lower than that from conduction or radiation. The circulating mass flow rate in the MHTGR is near 0.22 kg/s, and in the HTTF is about 0.37 g/s.

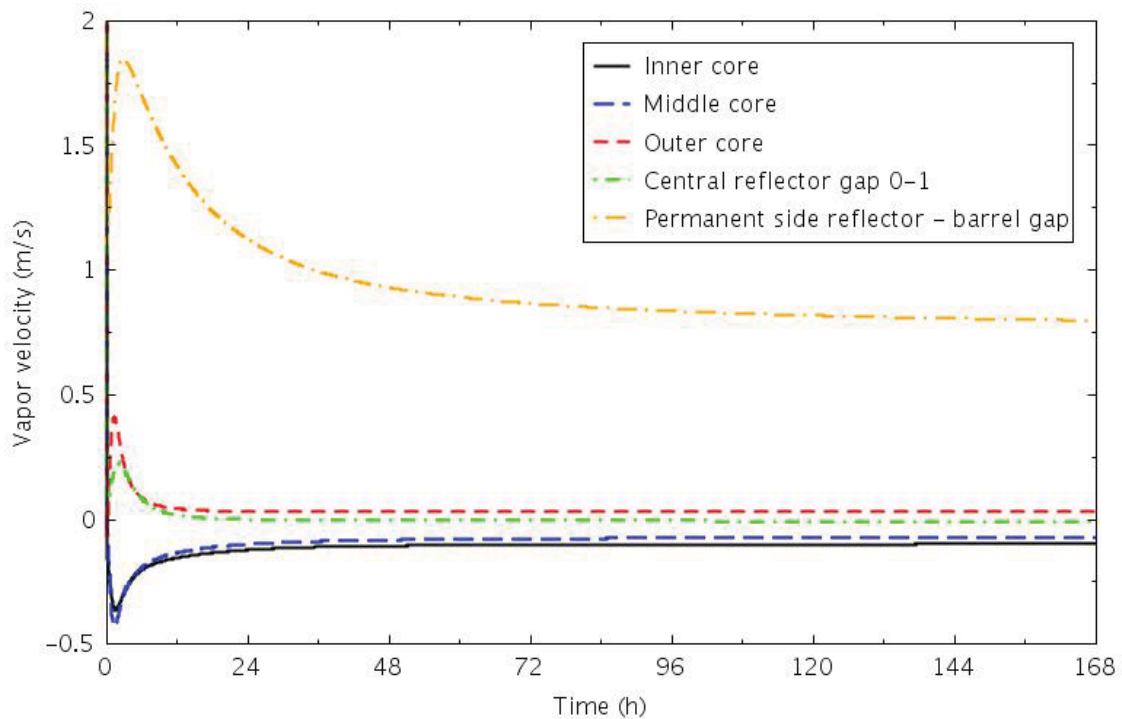


Figure 6-39. Calculated channel inlet coolant velocities for the MHTGR PCC transient.

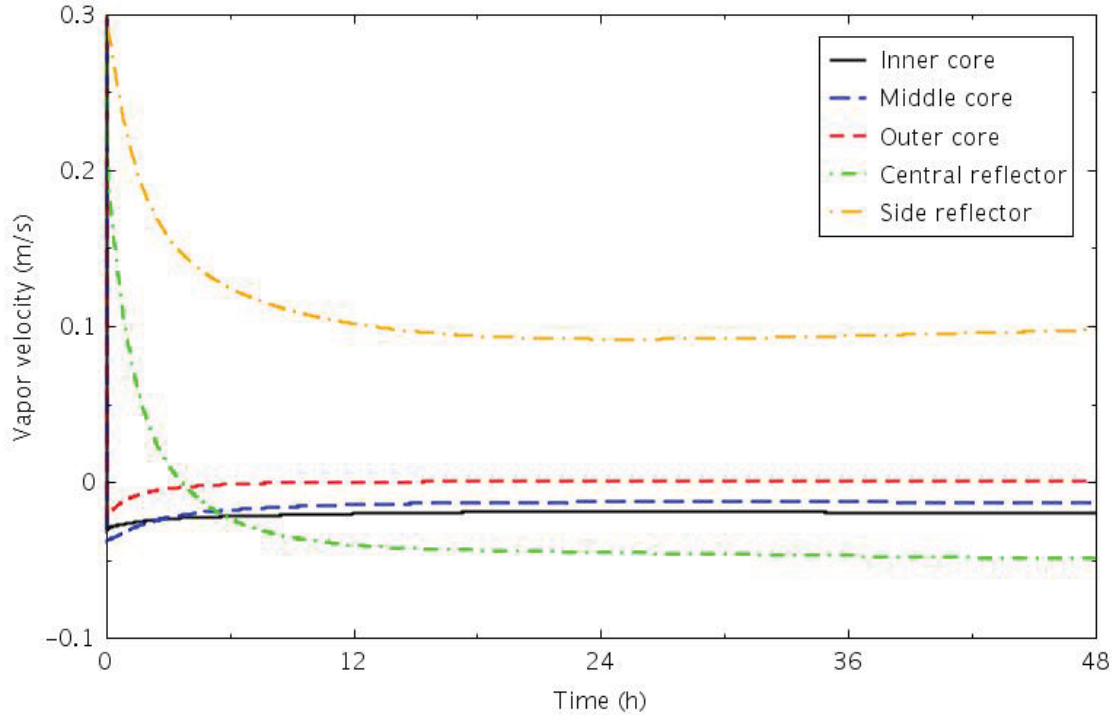


Figure 6-40. Calculated channel inlet coolant velocities for the HTTF PCC transient.

6.2.2 Sensitivity Calculations

In the sensitivity calculations, the decay power was increased by 20%. Peak fuel temperatures from the MHTGR base and sensitivity calculations are compared in Figure 6-41. The peak temperatures were 100 to 150°C higher and occurred about 12 hours later with the higher decay power. Figure 6-42 shows the corresponding heater rod temperatures from the HTTF calculations. These peak temperatures also increased 100-150°C, with a delay of about 6 hours.

Peak reactor vessel temperatures are shown in Figures 6-43 and 6-44. For the MHTGR, the peak temperature occurred near 84 hours in the base case, while in the sensitivity case it was near 90 hours and about 30°C higher. In the HTTF simulation, the peak temperature increased about 20°C, and was delayed about 4 hours. The peak vessel temperatures were about 70°C lower in the HTTF than in the MHTGR.

Figure 6-45 presents the calculated reactor vessel heat removal for the MHTGR, together with the decay power. The peak heat removal is 0.2 MW higher than in the base case (see Figure 6-37), and the time at which the heat removal exceeds the decay heat is about 10 hours later. The corresponding variables from the HTTF simulation are shown in Figure 6-46. Compared with Figure 6-38, the peak heat removal is about 6 kW higher in the sensitivity calculation, and the cross-over with the decay heat occurs about 5 hours later.

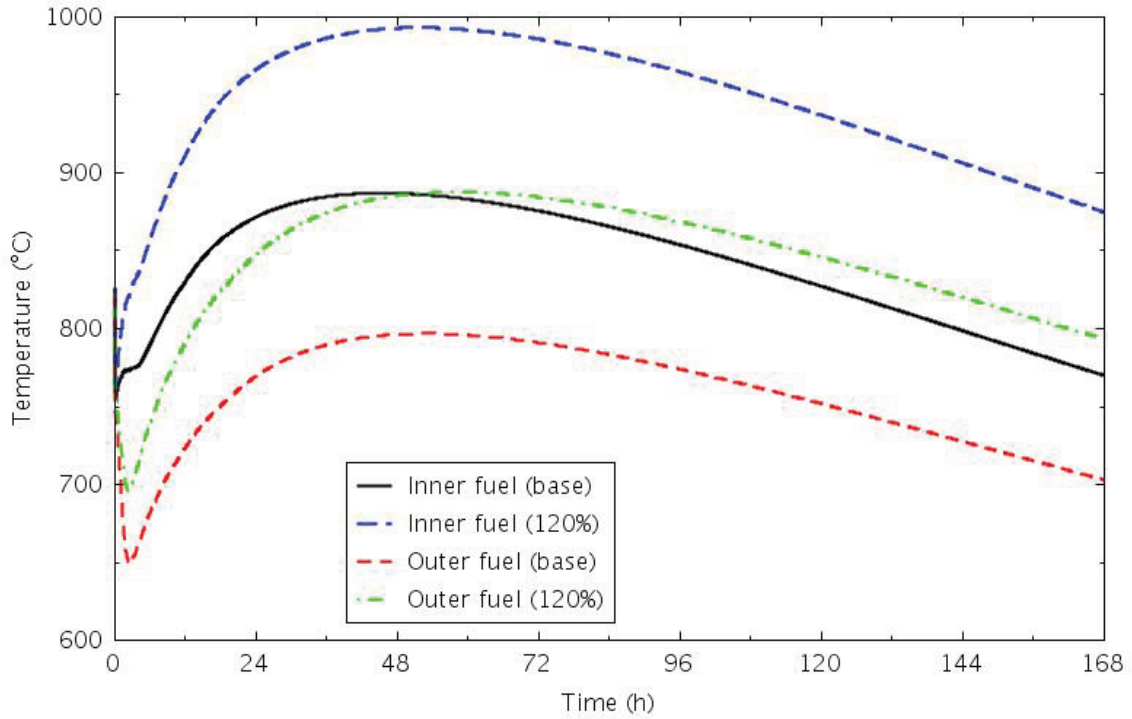


Figure 6-41. Peak fuel temperatures for the MHTGR PCC base and 120% decay power cases.

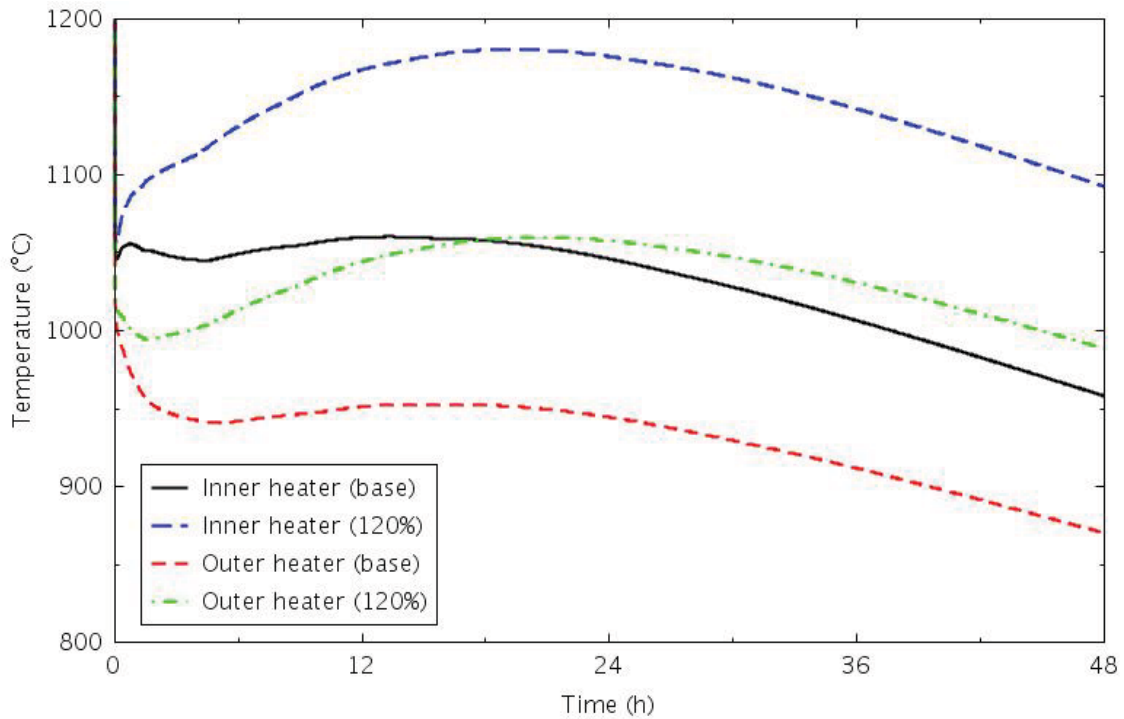


Figure 6-42. Peak heater rod temperatures for the HTTF PCC base and 120% decay power cases.

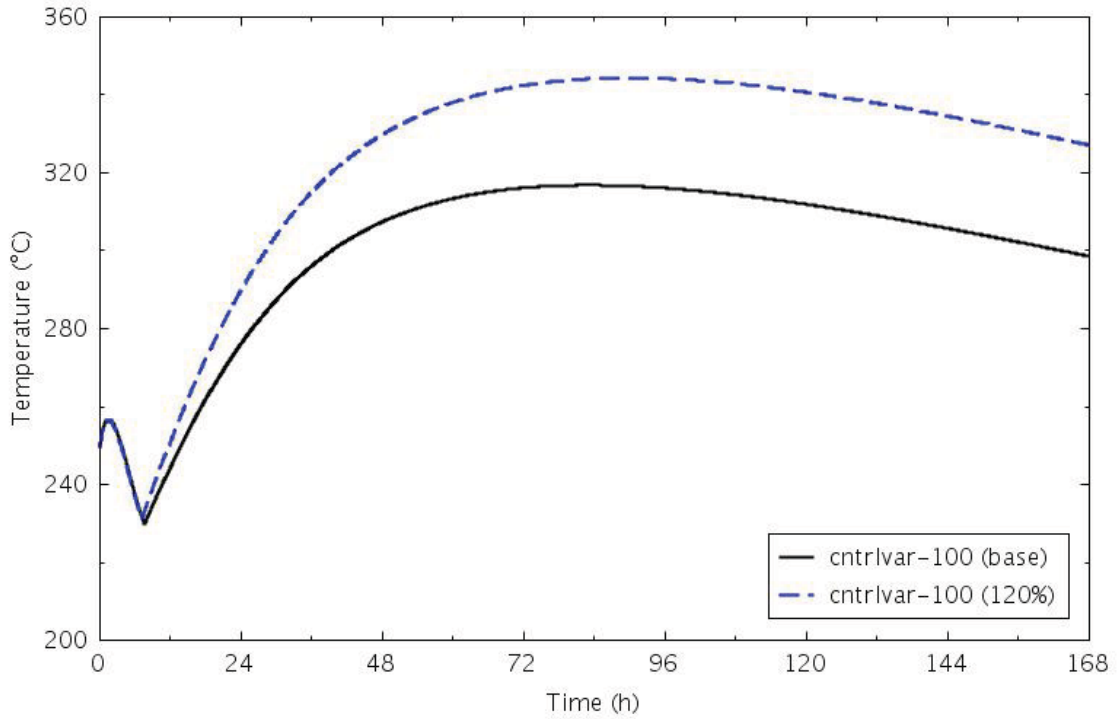


Figure 6-43. Peak reactor vessel temperatures for the MHTGR PCC base and 120% decay power cases.

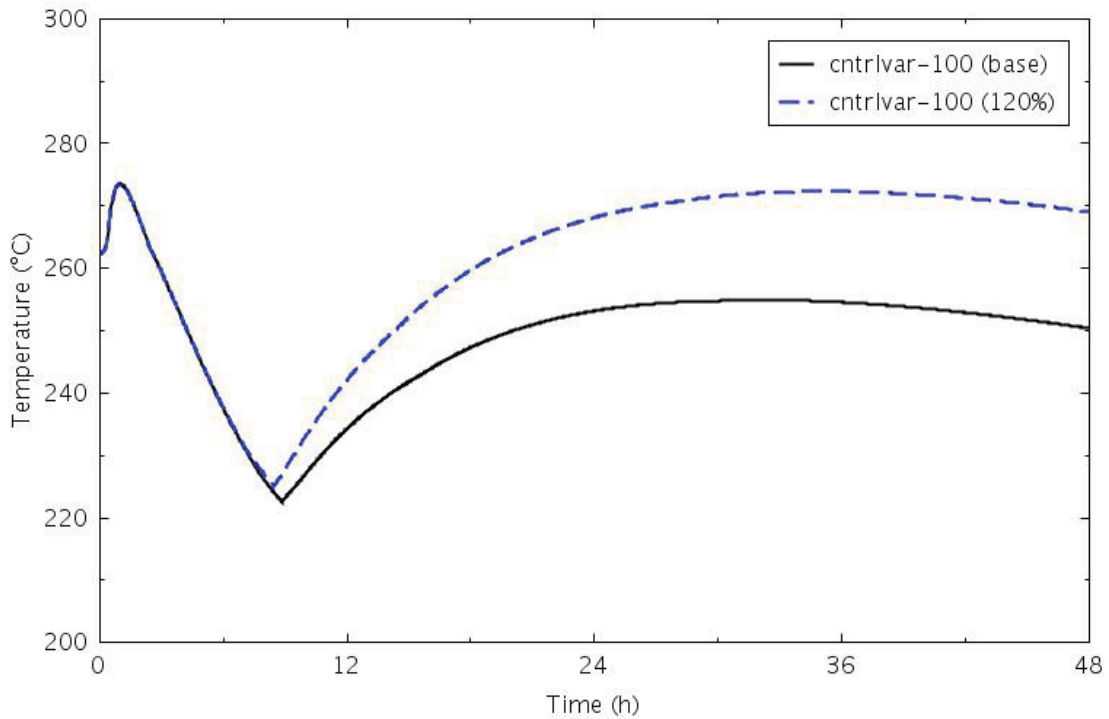


Figure 6-44. Peak reactor vessel temperatures for the HTTF PCC base and 120% decay power cases.

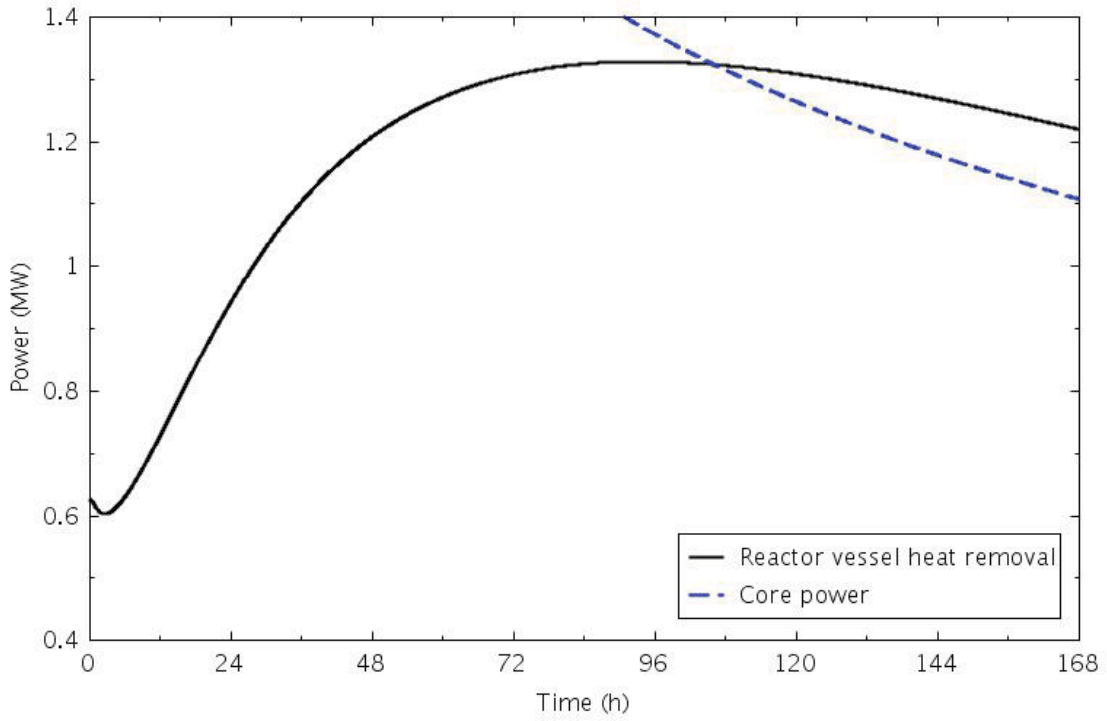


Figure 6-45. Calculated reactor vessel heat removal and core power for the MHTGR PCC 120% decay power case.

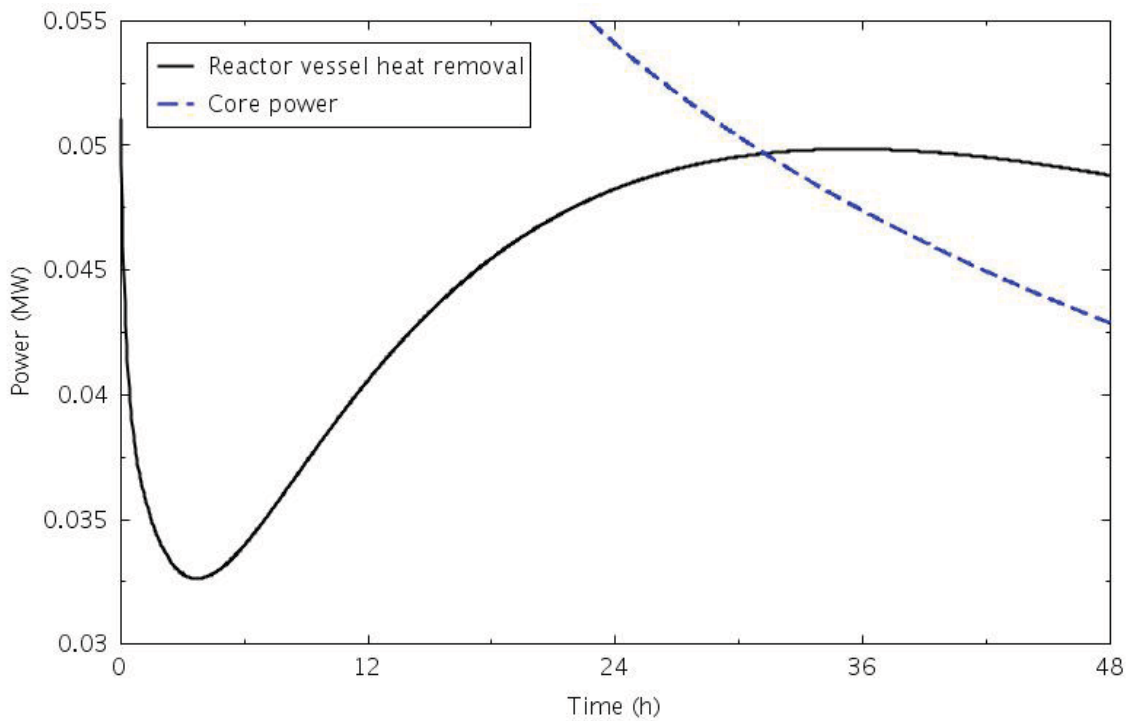


Figure 6-46. Calculated reactor vessel heat removal and core power for the HTTF PCC 120% decay power case.

6.3 HTTF Operational Transients

Several operational transients in the HTTF were simulated. These were heatup and cooldown evolutions that may be encountered when preparing the facility to run an experiment or when recovering after an experiment is over.

The first transient simulated was a heatup from ambient temperature to steady-state operating conditions. Full steady-state helium flow was established, then the power was increased linearly from zero to 2.2 MW over 1 hour.

Figure 6-47 presents the core fuel and ceramic temperature response. Steady-state temperatures are reached shortly after full power to the heater rods is established. Temperatures in the central and side reflectors are shown in Figure 6-48. The central reflector temperatures have all reached steady-state by 12 hours, while the side reflector takes about 20 hours to reach steady-state. Permanent side reflector, core barrel, and reactor vessel average temperatures are presented in Figure 6-49. The permanent side reflector takes the longest to reach steady-state, about 20 hours.

Because of the different amount of time required to reach steady-state, radial temperature gradients in the core ceramic block, which includes the central and side reflectors, will likely be higher during heatup than during steady-state operation. Figures 6-50 and 6-51 show the relative heatup of different regions of the core block on different time scales. At 2 hours, the region around the heater rods is nearly at full temperature, while the ends of the reflectors have only completed 30 to 40% of their heatup. This suggests that it may be helpful to try to control the heatup so that the reflectors do not lag so far behind the core temperature increase in order to reduce the thermal gradient across the core ceramic blocks.

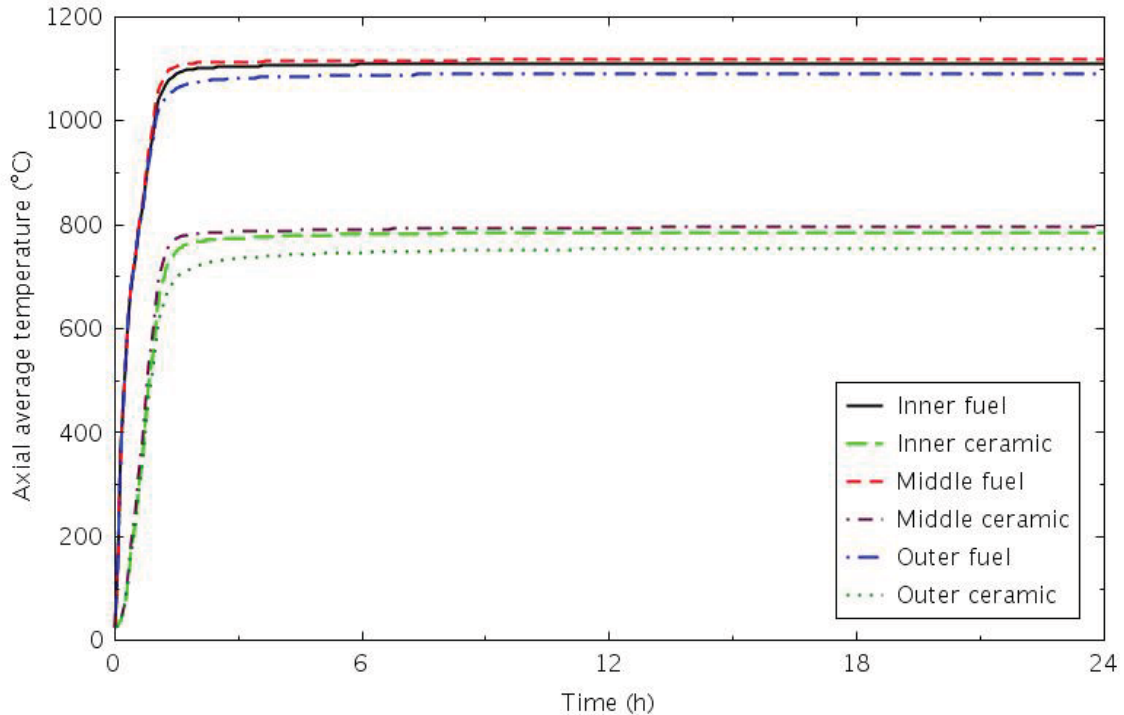


Figure 6-47. Calculated HTTF core structure average temperatures during an initial heatup transient.

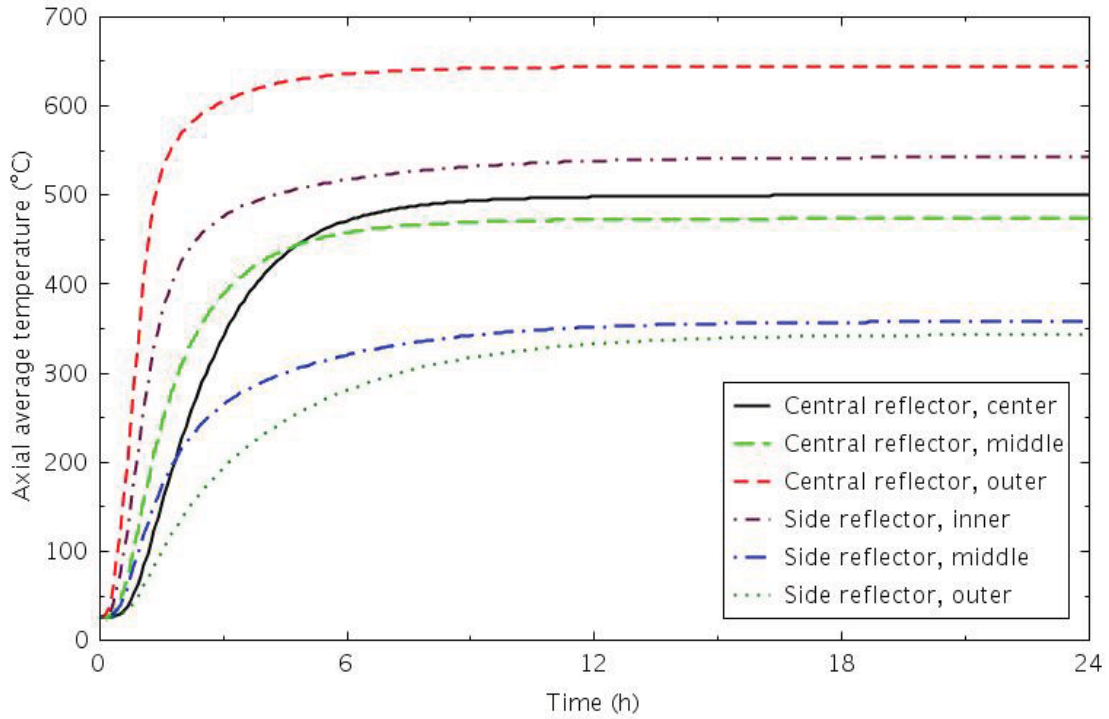


Figure 6-48. Calculated HTTF reflector structure average temperatures during an initial heatup transient.

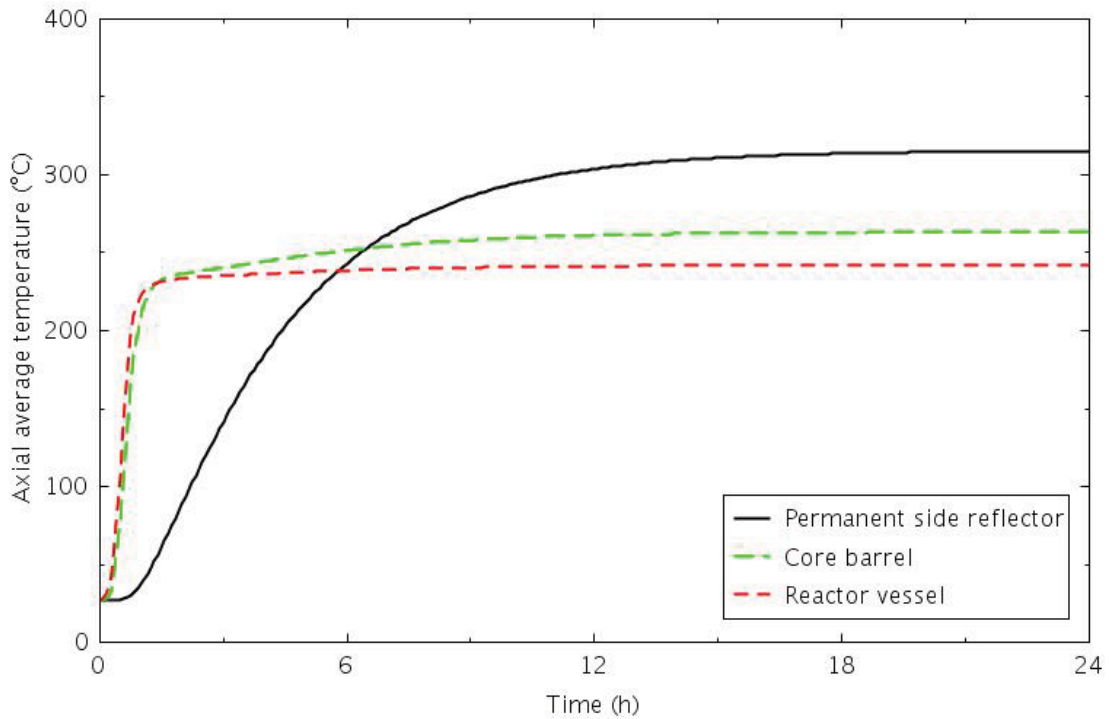


Figure 6-49. Calculated HTTF structure average temperatures during an initial heatup transient.

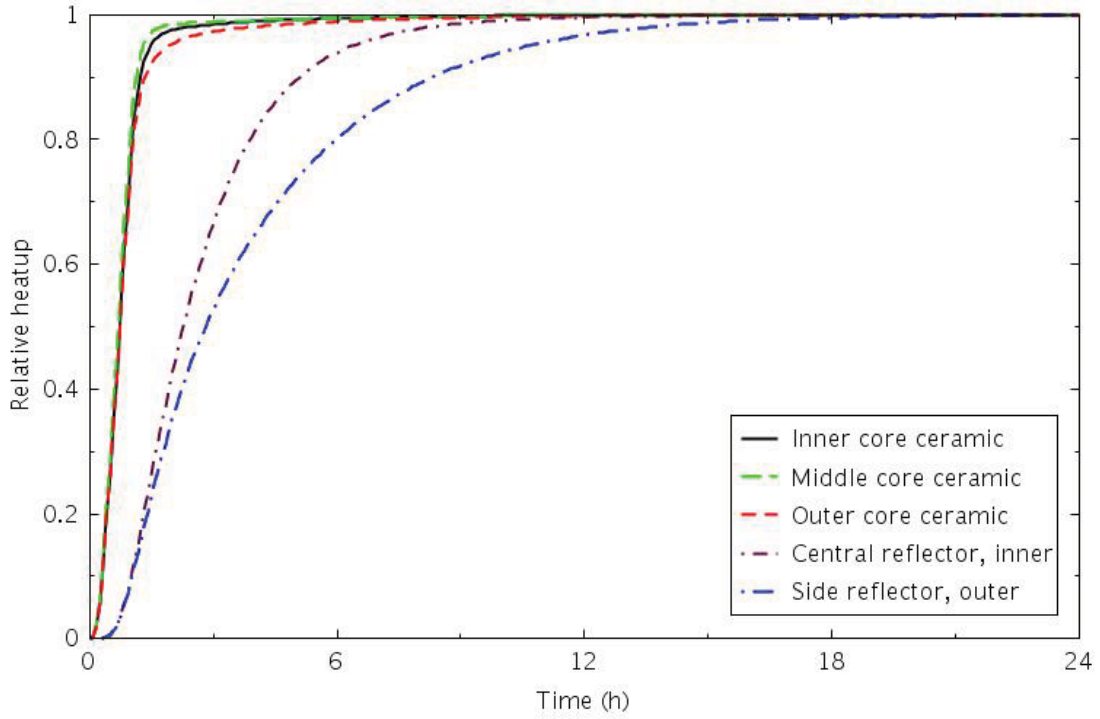


Figure 6-50. Calculated HTTF structure relative temperatures during an initial heatup transient.

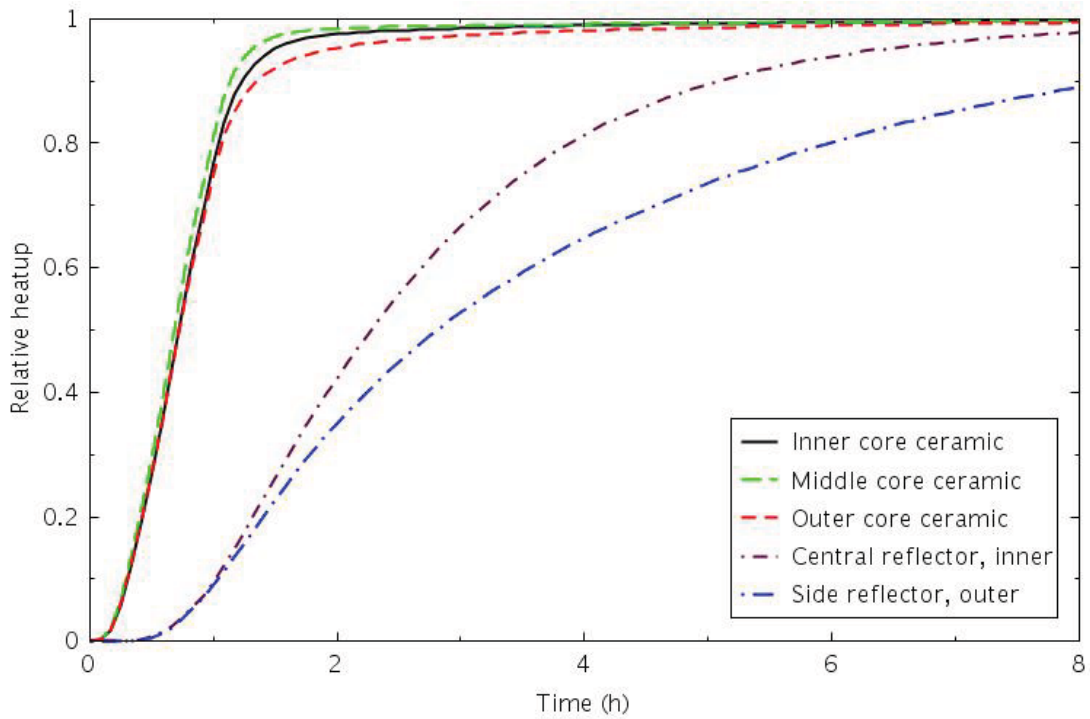


Figure 6-51. Calculated HTTF structure relative temperatures during an initial heatup transient.

Given the long time required to heat the facility, it may be desirable to run several experiments in series, without cooling the system down in between. A calculation was performed in which the facility was heated back up following a DCC experiment. After 48 hours of a DCC transient, the flow and pressure were increased back to steady-state conditions in 30 seconds, and the power was held constant for 60 seconds before being ramped linearly to full power over a 60-second time span.

Axial average temperatures for various structures in the model are shown in Figures 6-52 through 6-54. The heater rods and reactor vessel heat up, while the remaining structures need to cool down to reach normal full power operating conditions. The permanent side reflector again takes the longest time to reach steady-state, about 20 hours, the same as for the initial heatup from ambient. These results suggest that it might be better to start the recovery by initially cooling the system, and restoring power to the heater rods later.

Two cooldown scenarios were modeled following completion of a DCC experiment. At 48 hours, the power to the heater rods was turned off over 10 seconds, and a 30-second flow increase to either 20% or 50% of nominal operating conditions was imposed. The reactor inlet temperature was assumed to be 100°C lower than the outlet temperature or 27°C, whichever was higher.

Figures 6-55 through 6-57 present the temperatures for the 50% flow case. The core and reflector temperatures decreased throughout the transient, while the reactor vessel, core barrel, and permanent side reflectors heated up initially as hotter steam was circulated around to the vessel inlet. After 24 hours, all of the structure average temperatures are between 32 and 42°C, with the permanent side reflector taking the longest to cool down, as it has no direct convective cooling available to it.

Temperatures for the same structures for the 20% flow case are shown in Figures 6-58 through 6-60. After 24 hours, the temperatures range from 29 to 69°C.

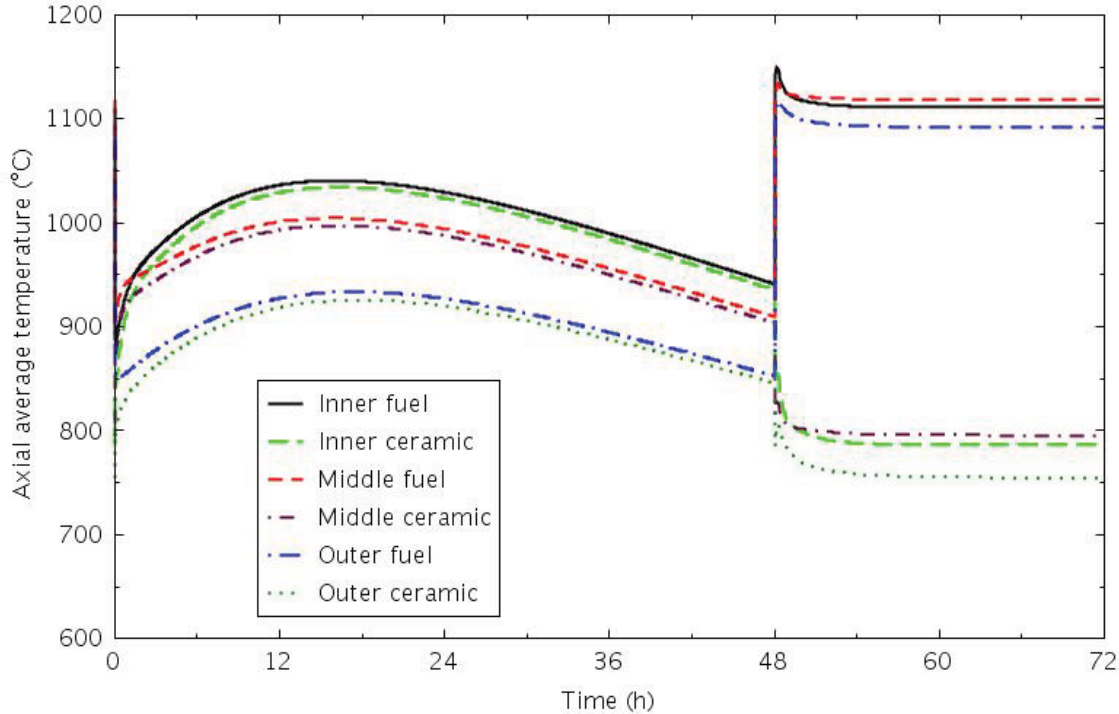


Figure 6-52. Calculated HTTF core average temperatures for the DCC reheat transient.

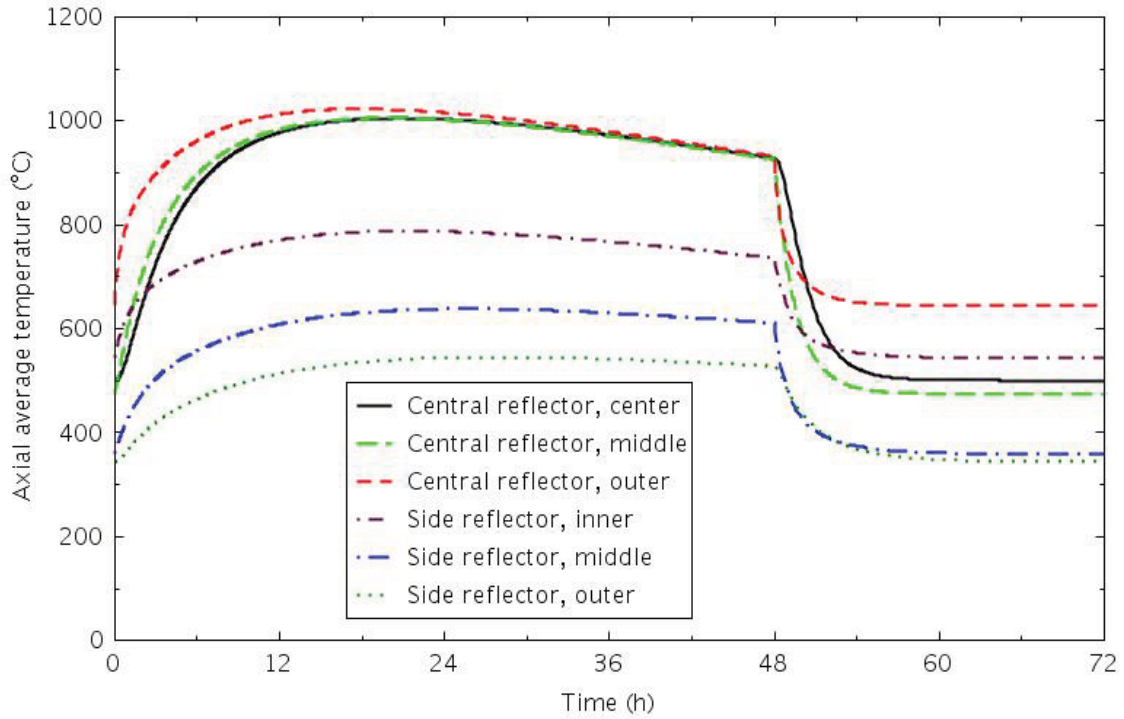


Figure 6-53. Calculated HTTF reflector average temperatures for the DCC reheat transient.

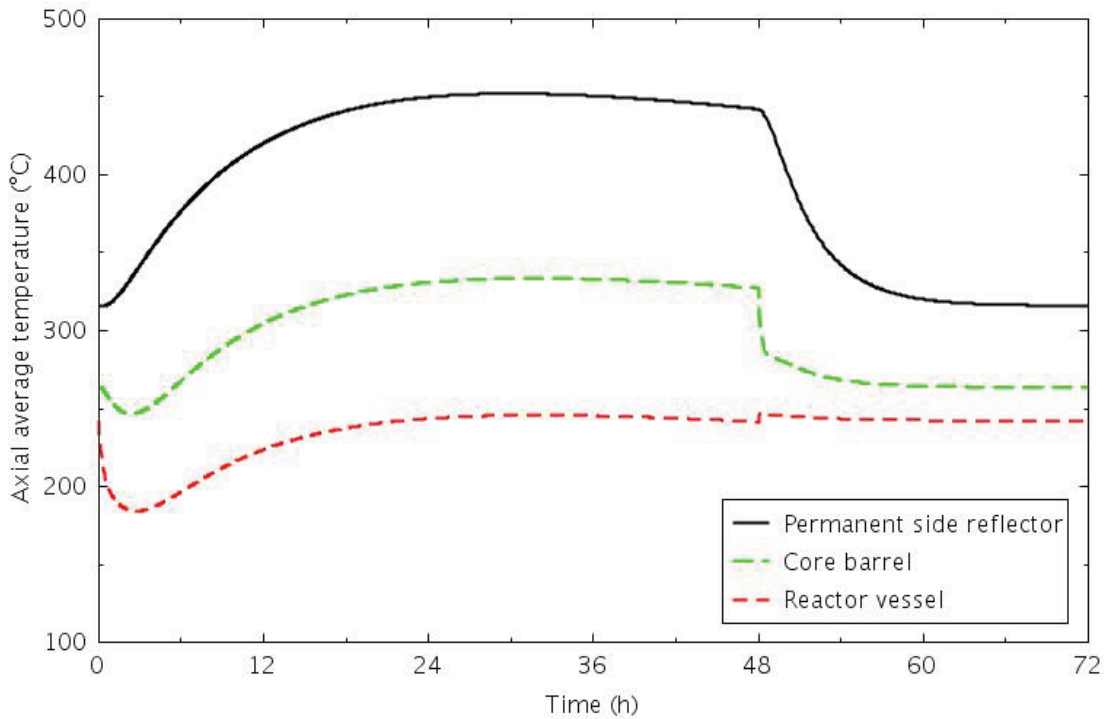


Figure 6-54. Calculated HTTF structure average temperatures for the DCC reheat transient.

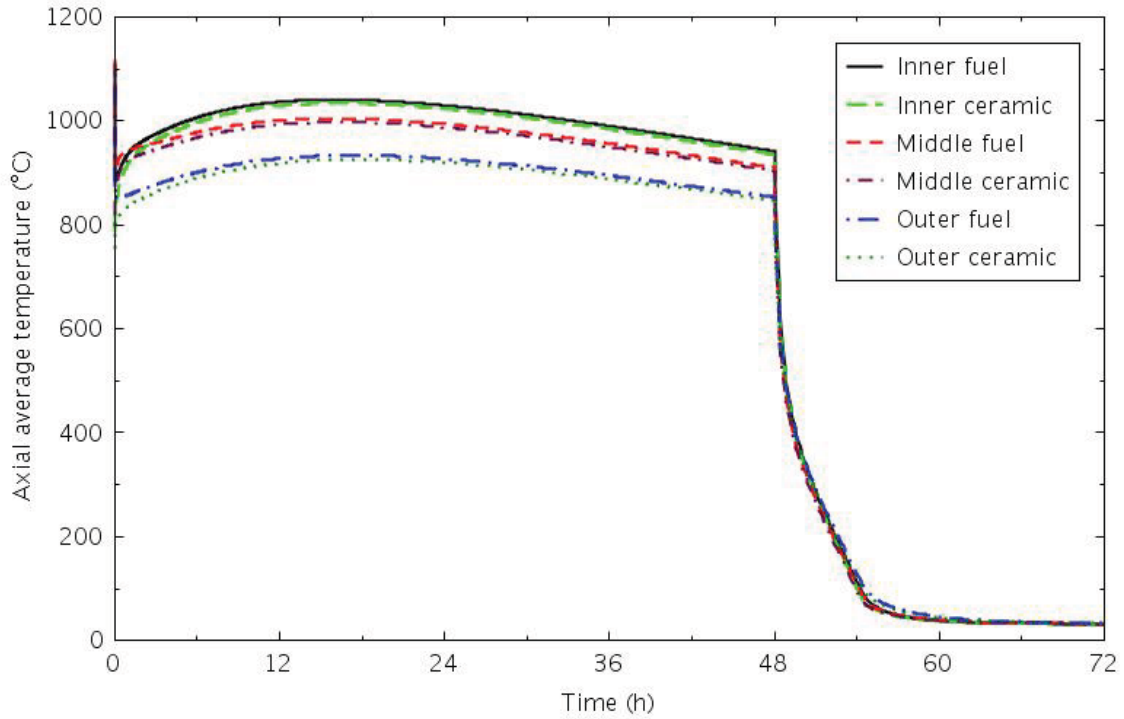


Figure 6-55. Calculated HTTF core structure average temperatures for the DCC 50% flow cooldown transient.

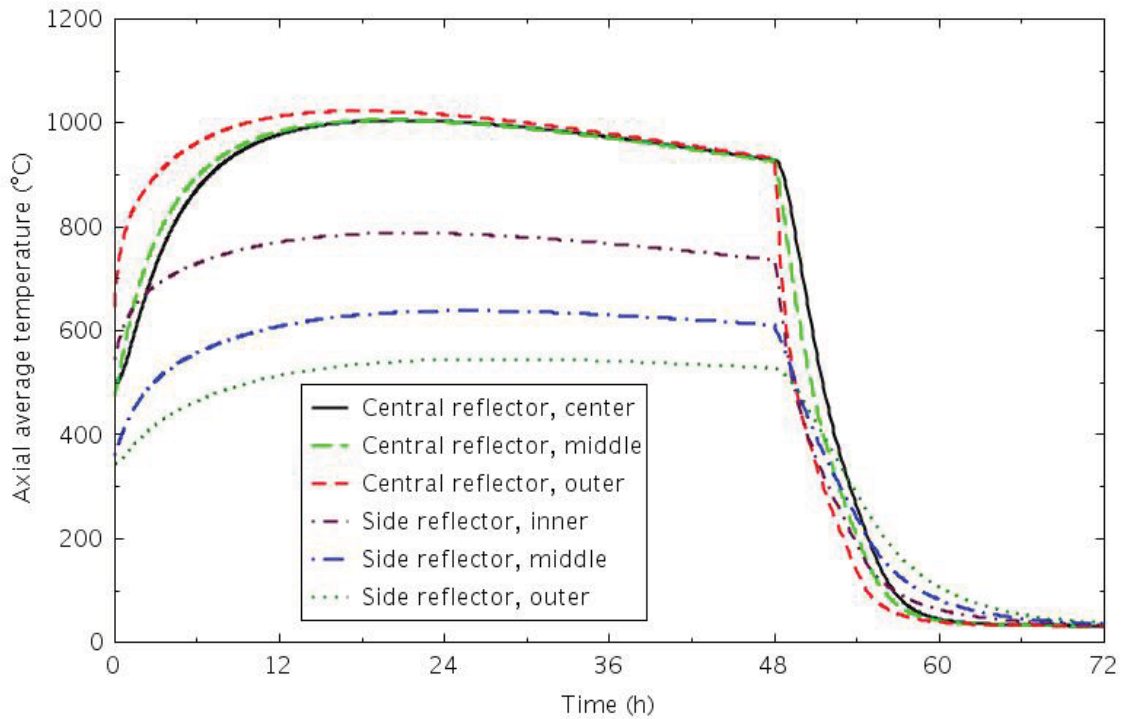


Figure 6-56. Calculated HTTF reflector structure average temperatures for the DCC 50% flow cooldown transient.

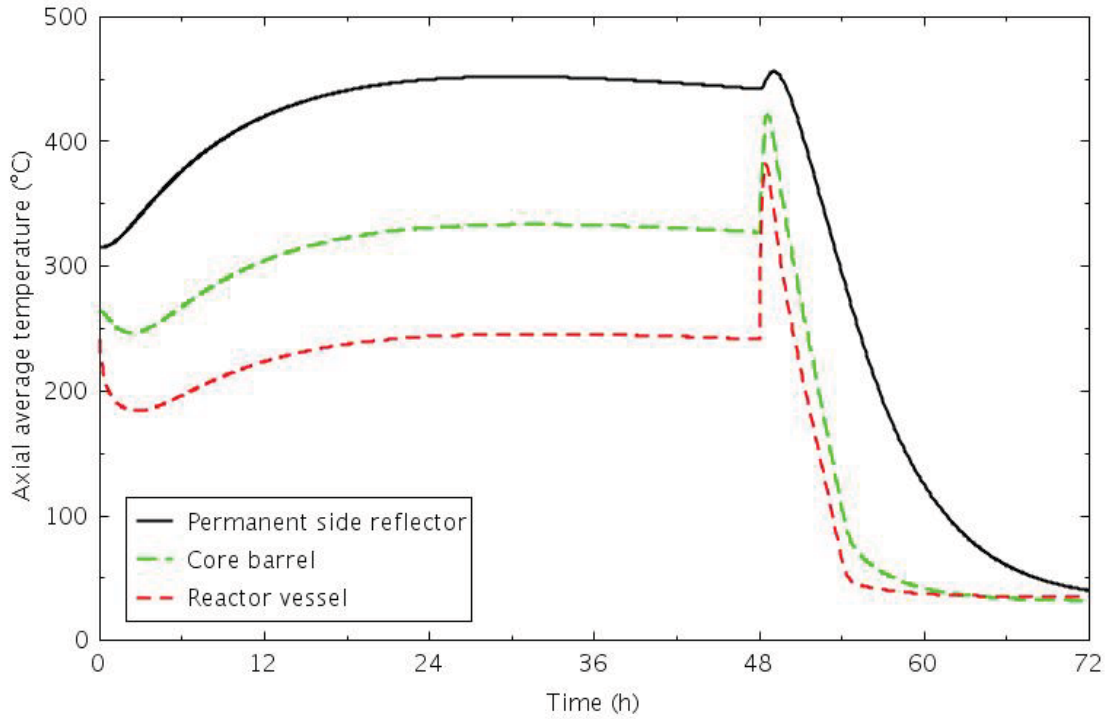


Figure 6-57. Calculated HTTF structure average temperatures for the DCC 50% flow cooldown transient.

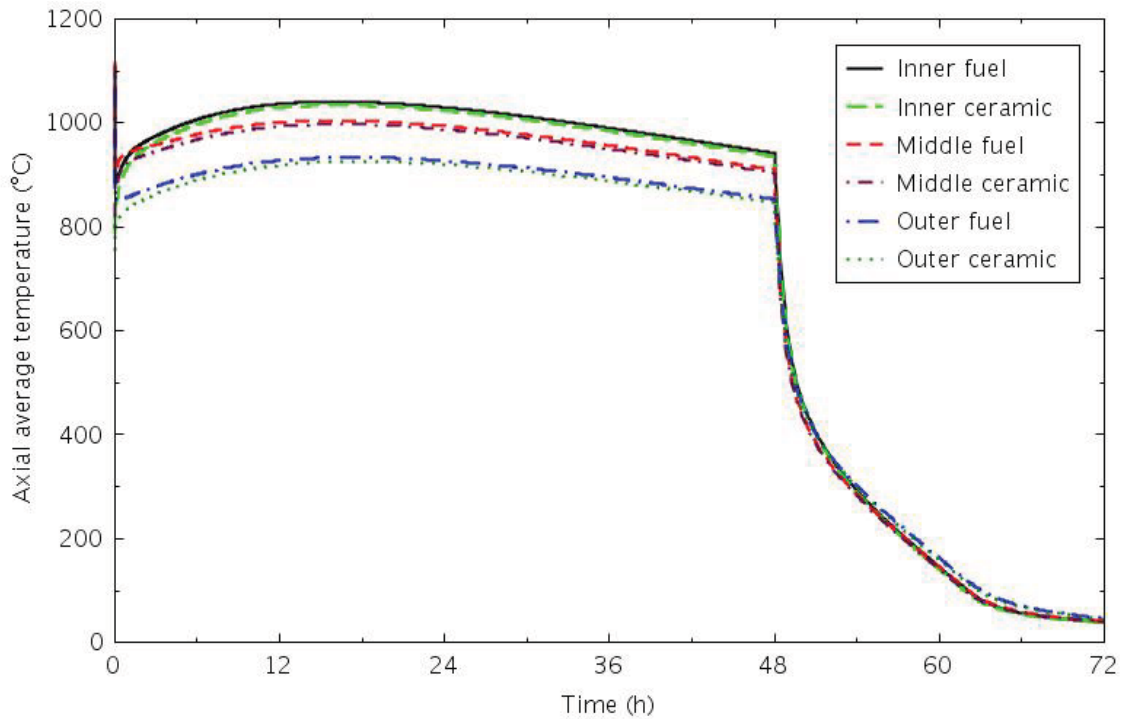


Figure 6-58. Calculated HTTF core average structure temperatures for the DCC 20% flow cooldown transient.

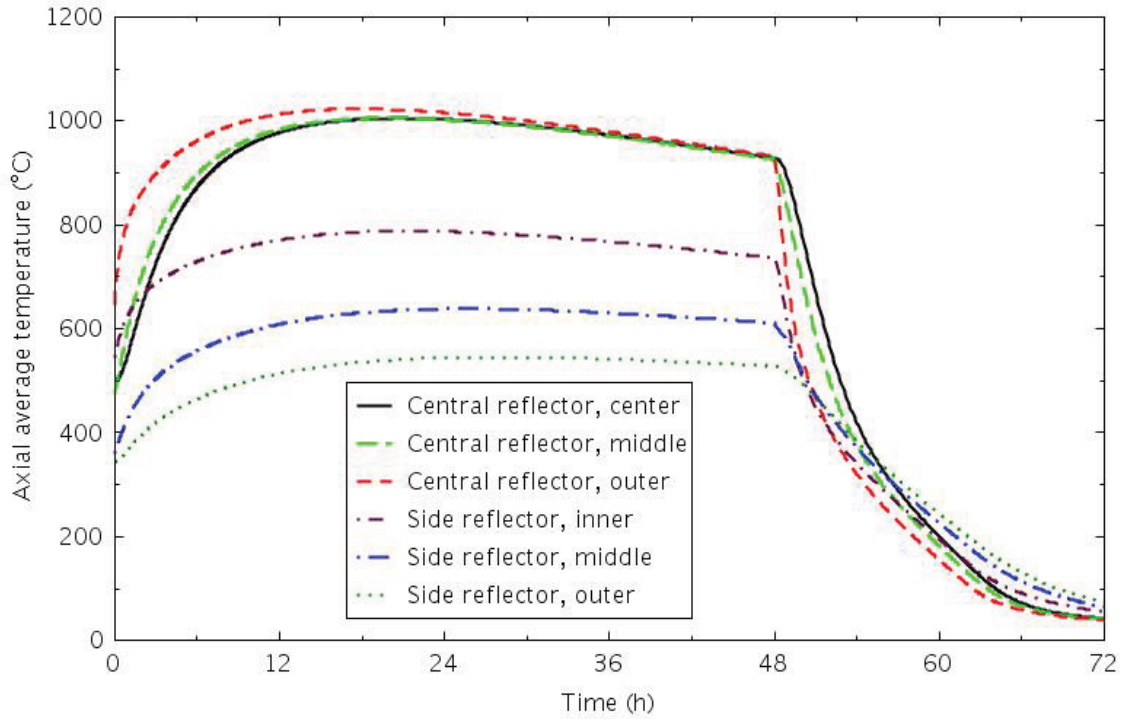


Figure 6-59. Calculated HTTF reflector structure average temperatures for the DCC 20% flow cooldown transient.

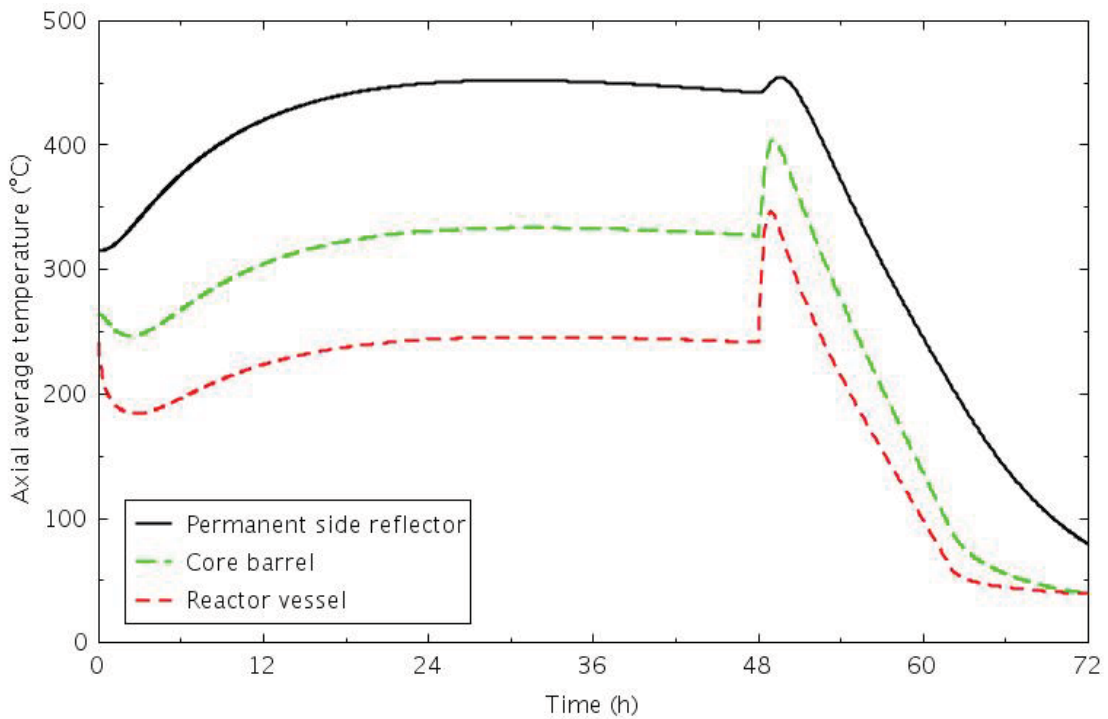


Figure 6-60. Calculated HTTF structure average temperatures for the DCC 20% flow cooldown transient.

6.4 Summary

Scoping RELAP5-3D calculations of DCC and PCC transients in the HTTF and the MHTGR were performed. Heatup and cooldown operational evolutions in the HTTF were also simulated.

The response of the two facilities during a DCC transient was similar. The order in which peak temperatures were reached in the various structures in the reactor vessel was the same in the HTTF and the MHTGR. Peak core temperatures were about the same, although the increase from steady-state conditions was larger in the MHTGR. The radial temperature gradient across the side reflector was about 100°C higher in the HTTF than in the MHTGR. Considering the facility time scale factor of 2, the HTTF temperatures are peaking earlier than those of the reference plant.

Two sets of sensitivity calculations were performed. Increasing the decay power by 20% resulted in higher peak temperatures that occurred later in both facilities. Modeling the boundary volume connected to the reactor vessel outlet as pure air instead of pure helium changed the core flow behavior. With helium, all of the core and reflector flow channels were flowing upward. With air, there was a mixture, with some channels flowing up and some down. However, there was an insignificant effect on the temperature response because the heat transfer is dominated by radiation and conduction, not by convection. Graphite oxidation was not considered in the MHTGR simulation.

There was little difference between the DCC and PCC transients in the HTTF, whereas noticeable differences occurred between these transients in the MHTGR. The principal reason for this is the power/flow mismatch at the onset of the transient.

For the PCC scenario the flow in the MHTGR is reduced at a slower rate than the power, allowing some of the stored energy in the core and reflectors to be removed before the overall heatup begins. This results in lower temperatures in the MHTGR during the PCC transient than in the HTTF, with the peak fuel temperature dropping by 100 to 150°C. In the HTTF, little of the stored energy was removed because the flow transitions to laminar flow in the HTTF much earlier in the coastdown than in the MHTGR using the assumption that the flow coastdowns begin concurrently for the HTTF and MHTGR scenarios. Thus the peak temperatures in the HTTF PCC transient were less than 20°C lower than those in the DCC transient where similar behavior occurred at the start of the scenario. However, for the PCC scenario, adjustments may be made to the HTTF operational procedures to better mimic the MHTGR behavior. Calculations to study the optimal way to perform each experiment have not yet been performed because the design was only recently finalized. But when such calculations are performed, investigations of prolonged recirculation flow in the HTTF that will result in an integrated scaled core heat removal equivalent to that obtained in the MHTGR will be initiated to give a better match between the two.

There were some minor differences in the flow patterns in the core between the MHTGR and HTTF, concerning which channels were flowing up and which down, but these had little effect on the overall facility response given the relative unimportance of convective heat transfer compared to radiation and conduction.

Two HTTF heatup transients were simulated, one from ambient temperature and one following termination of a DCC transient. The heatup from ambient indicated that there may be a concern with increased radial temperature gradients across the core blocks during the heatup. The recovery following a DCC experiment suggested that a more rapid return to operating conditions may be achieved if the system is first cooled for a while before reestablishing power to the heater rods.

Two cooldown transients following completion of a DCC experiment were also simulated, using different flow rates with the heaters turned off. The permanent side reflector is the structure that takes the longest to cool down, because it has no direct convective cooling by the flowing helium; it must transfer heat by radiation or conduction to either the core barrel or the side reflector. After 24 hours, all of the

structure average temperatures were within 15°C of ambient with ~50% of nominal cooling flow, and within 45°C of ambient with ~20% cooling flow.

The calculations performed to date indicate that the HTTF experiments will give a reasonable representation of the behavior of the MHTGR for the scenarios under consideration. Although sometimes the flow behavior in the cooling channels may differ by an order of magnitude, e.g., during steady-state conditions, from that of the MHTGR, because the cooling channel flow is either turbulent in both the HTTF and the MHTGR or laminar in both concurrently, enables the use of the scaling laws to obtain reasonable comparisons between the HTTF and MHTGR.

7. SUMMARY OF DEVELOPMENTAL NEEDS FOR RELAP5-3D

Several areas in which additional code development is needed for the RELAP5-3D computer code have been identified and are required to calculate the scenario behavior in both the MHTGR and the HTTF. In its present form, RELAP5-3D cannot properly calculate the behavior of some of the scenarios which are part of the planned experimental matrix presented in Chapter 3. Examples of this are: (a) countercurrent density-gradient driven stratified flow in the hot duct for not only the small-break loss-of-coolant accidents but also the double-ended guillotine rupture, (b) the recirculation flow zones that will occur in the lower and upper plena during the PCC, and (c) the movement of dust particles. For this reason, a short discussion is given below on the developmental needs.

7.1 Air Ingress

Three potential methods of modeling density-gradient driven stratified flow are described below. All of the methods rely on having pertinent experiment data available to inform the modeling approach.

7.1.1 Split Pipe Model

This approach would divide the hot duct into top and bottom pieces, with hotter, less dense gas flowing in the upper portion from the outlet plenum to the break, and cooler, denser gas flowing in the lower portion from the break to the outlet plenum. The two counter-flowing streams do not interact. Data are needed to establish the flow area split between the two flow streams; in the absence of data, sensitivity calculations could be performed or results of CFD simulations could be used. This modeling technique has been used successfully in the past for modeling countercurrent gas flow in pressurized water reactor hot legs during severe accidents [Bayless et al. 1995]. One advantage of this approach is that it does not require a code modification; the modeling is done strictly through code input. An area of potential difficulty is making the transition from the horizontal piping to the vertical orientation that would be needed in the outlet plenum, where it would be necessary to determine how much mixing occurs, or conversely, how well stratified the cooler gas layer may remain as it fills the outlet plenum. The outlet plenum mixing may be similar to that in the steam generator inlet plenum for the severe accident case referenced above, which was adequately handled by the modeling approach.

7.1.2 Add a New Correlation to the RELAP5-3D Code

A new correlation would be developed and added to the code to model the air ingress. Available data sets from which the correlation would be developed have not been identified. Transport of the air from the break to the outlet plenum would still be a problem that would likely require use of a split model as described above. The code has an air diffusion model that may be appropriate for some small break scenarios.

7.1.3 Link to a CFD Code

This approach would use a CFD code to perform the calculations of the air ingress from the break and transport to the reactor vessel outlet plenum. The interface to the RELAP5-3D system model would be at the outlet of the core and reflector coolant channels. RELAP5 would provide the temperature, velocity, and composition of the fluid exiting the coolant flow paths into the outlet plenum. It would also provide the mass flow or velocity of the fluid entering the coolant channels from the outlet plenum. The CFD code would provide the fluid composition and temperature of the gas flowing up into the core and reflector flow channels from the outlet plenum, and would accept the flow out of the core. Mixing in the outlet plenum and flow through the hot duct to the break would be calculated by the CFD code.

7.1.4 Summary of Developmental Needs to Model Density-Gradient-Driven Stratified Flow

Of the three techniques summarized above, only the linkage to a CFD code will likely give the calculational results at the required quality level. The other two techniques (using a split-pipe or a correlation) are considered stop-gap methods. For example, of the three techniques, only the CFD code will be capable of analyzing the double-ended guillotine rupture (DEGB) scenario when not all the flow moving into the lower plenum via the hot duct moves through the core and into the upper plenum. For some portions of the DEGB scenario it is postulated that some fraction of the gases moving into the lower plenum will circulate and as they are heated, move in the countercurrent direction through the hot duct and into the source volume. Therefore, linkage to a CFD code is recommended for future RELAP5 development.

7.2 Dust and Fission Product Tracking

Graphite dust generated during operation and fission products released from the fuel will need to be accounted for in detailed accident analyses. Phenomena to be addressed include generation and release to the coolant flow paths, transport, deposition, resuspension, and eventual release from the system. Chemical interactions between the dust, fission products, and system components may need to be modeled. Fission products in aerosol form will likely need to be addressed, particularly with dust particles being potential seeds for aerosol formation. Developing these features for the RELAP5-3D code would be a major undertaking. A more efficient approach would be to link an external code that performs these calculations, or to import an existing code into RELAP5-3D.

7.3 Graphite Oxidation

Depending on the oxidation environment, the reaction may be endothermic (water/steam) or exothermic (air). While the release of the generated carbon dioxide or carbon monoxide may be a health issue, the principal concern is the potential reduction in structural integrity that may occur as a result of the support columns being oxidized. The model will need to address oxidation in both air and steam, heat generation/removal, gas generation and release, oxygen removal from the coolant, progress of the oxidation front through the structure, and oxygen starvation of the oxidation reaction. Development of a generalized oxidation model for RELAP5-3D is currently underway as part of another project, but this model only addresses the energy deposition and oxidation front progression phenomena; the user must also input the appropriate rate constants for the oxidation reaction.

8. REFERENCES

- ABAQUS Standard Version 6.11-1, Dassault Systèmes 2011.
- Ball, S. J., et al., 2008, *Next Generation Nuclear Plant Phenomena Identification and Ranking Tables (PIRTs)*. NUREG/CR-6944, Vol. 2: Accident and Thermal Fluids Analysis PIRTs.
- Bayless, P. D., et al., 1995, *Severe Accident Natural Circulation Studies at the INEL*, NUREG/CR-6285, INEL-94/0016, February 1995.
- DOE/HTGR-86-024, 1986, *Preliminary Safety Information Document for the Standard MHTGR*, Stone & Webster Engineering Corp, HTGR-86-024.
- I-DEAS NX6, Copyright 2008 Siemens Product Lifecycle Management Software Inc.
- Lewis, E. E., 1977, *Nuclear power reactor safety*, John Wiley, New York, pp. 298-302.
- MacDonald, P. E., et al., 2003, *NGNP Preliminary Point Design – Results of the Initial Neutronics and Thermal-Hydraulic Assessments During FY-03*, INEEL/EXT-03-00870, Rev. 1, September 2003.
- Math Soft., 2001, *MathCad 2001 User's Guide*, Math Soft, Inc.
- National Institute of Standards and Technology (NIST) Webbook, 2010, <http://webbook.nist.gov>, accessed September 13, 2010.
- RELAP5 Code Development Team, 2005, *RELAP5-3D Code Manual*, INEEL/EXT-98-00834, Rev. 2.4, June 2005.
- STAR-CCM+, version 5.02.009, 2010, CD-adapco, 60 Broadhollow Road, Melville, NY 11747.
- Tung, Y-H., Johnson, R. W. and Sato, H., "Effects of Graphite Surface Roughness on Bypass Flow Computations for an HTGR," paper PVP2011-58035, ASME 2011 Pressure Vessel and Piping (PVP) Division Conference, Baltimore, Maryland, July 17-21, 2011.
- Woods, et al., 2009, *Scaling analysis for the very high temperature reactor test facility at Oregon State University*, OSU-HTTF-000000-TECH-oo1-R0/DRAFT.
- Woods, et al., 2011, *Preliminary Test Plan for the High Temperature Test Facility at Oregon State University*, OSU-HTTF-000000-TECH-oo2-R0/DRAFT.